UNIVERSITÀ
DEGLI STUDI
DI PADOVA

Zoom-in on the dust-obscured phase of galaxy formation with gravitational lenses

Thesis Advisors
Prof. Alberto Franceschini, *Università degli Studi di Padova*
Dott. Mattia Negrello, *Cardiff University*
Thesis External Evaluators
Prof. Stephen Serjeant, *The Open University*
Dott. Neal Jackson, *Manchester University*
PhD Course Coordinator
Prof. Giampaolo Piotto

PhD Student
Andrea Francesco Maria Enia

Dipartimento di Fisica e Astronomia "Galileo Galilei"
Università degli Studi di Padova
PhD Course in Astronomy, XXXI Cycle

Zoom-in on the dust-obscured phase of galaxy formation with gravitational lenses

Abstract

Over the last 20 years gravitational lensing has become an essential instrument to investigate the structures within the Universe and the Universe itself. It directly traces the gravity of matter, whether baryonic or not, and so it's essential for a systematic study of dark matter and its distribution ob both small and large scales. Moreover, the magnification generated by a foreground lensing system, like a massive elliptical galaxy, on a background source allows us to study high-redshift galaxy structures down to scales difficult to probe with the largest telescope at present, and to detect intrinsically faint objects.

In this PhD thesis I describe the advantages that gravitational lensing offers in the study of high-redshift ($z > 1.5$) dusty star forming galaxies (DSFGs), progenitors of the early-type (ETGs) observed in the local Universe. DSFGs are the major contributors to the cosmic star formation activity in the Universe and, as such, they represent the key to understand the build-up of galaxies. Dust absorption of UV/optical radiation from newborn stars is re-emitted in the far-infrared/sub-mm bands, making DSFGs particularly bright at those wavelengths.

In order to extract information from the galaxy-galaxy strong lensing events involving DSFGs, I have written a Python code performing lens modelling and source reconstruction, based on the Regularized Semilinear Inversion method by

Warren and Dye (2003), as outlined in Enia et al. (2018). This method reconstructs the intrinsic (i.e. un-lensed) surface brightness of the background galaxy without any analytic pre-assumption on its distribution, while searching in the parameters space for the mass distribution of the lens. Since DSFGs are the main focus of this project, and since they are very bright at FIR/sub-mm wavelengths, I have extended the formalism to the uv plane, in order to deal with interferometric data. In fact, interferometry is the best observational technique to achieve high resolution imaging in the sub-mm/mm bands, thanks to facilities like the Atacama Large Millimeter/sub-millimeter Array (ALMA). Furthermore, since the lens galaxy is usually a massive elliptical, the main emission in the sub-mm/mm is due almost exclusively from the background galaxy. DSFGs show extremely steep number counts, so that any DSFGs with a very high flux density (e.g. above $\sim$ 100mJy at 500μm) is expected to be lensed. The selection of gravitationally lensed galaxies based on a simple cut in flux density has proven to be extremely efficient in the search for these sources in wide area extragalactic surveys such as the Herschel Astrophysical Terahertz Large Area Survey (H-ATLAS). This survey found 80 candidate lensed galaxies, 20 of which have already been confirmed to be lensing systems by a number of follow-up observations mainly with the Sub-Millimeter Array (SMA), the Hubble Space Telescope and the Keck telescope.

In Enia et al. (2018) I have applied my code to the SMA observations of 12 strongly lensed galaxies from the H-ATLAS in order to derive their morphologies, sizes and magnifications. The derived lens model parameters are

in general consistent with previous findings (i.e. Bussmann et al., 2013), however the estimated magnification factors, ranging from 3 to 10, are lower. These discrepancies are observed in particular where the reconstructed source hints at the presence of multiple knots of emission. An appropriate estimate of the magnification factor is essential to properly retrieve the physical properties of the sources, i.e. CO line luminosities, star formation rates, or SFR surface densities.

In Massardi, Enia et al., 2018 multiwavelength observations of two strongly lensed sources are presented. H-ATLAS J090740.0-004200, also known as SDP.9, and H-ATLAS J091043.1-000322, also known as SDP.11, both come from the H-ATLAS sample. The observations were carried out with Chandra, HST and ALMA, covering a large portion of the electromagnetic spectrum. These multiwavelength observations probed the presence of highly obscured nuclear activity in the galaxy, with X-ray emissions generated in the nuclear area, allowing an insight on the co-evolution between the central SMBH and the galaxy, as predicted by various evolutionary theories for galaxy formation and evolution. I applied the code to SDP.9, reconstructing the background source in the different bands, obtaining a clear cospatiality in the source plane between the sub-mm emission, tracing the star formation, and the X-ray signal, tracing the nuclear activity, within a circle of ~ 400 pc diameter. This analysis will be further exploited in the future thanks to the large number of follow-up campaigns in different wavelength ranges currently ongoing.

In Rodighiero, Enia et al., in prep, a study of the statistical properties of a sample of dusty sources with very efficient star formation rates (SFR) is

performed, in order to understand the role of enhanced SFR in triggering the Black-Hole Accretion Rate. These sources are *Herschel*-selected in the COSMOS field, with SFRs elevated $4\times$ above the star-forming "main sequence", classifying them as starbursts (SB). Here, by means of a multicomponent spectral energy distribution fitting analysis, the contribution of stars, AGN torus, and star formation to the total emission at different wavelengths is separated, spanning the range from the UV to the far-IR. The sample is divided into active SBs (dominated by an AGN emission, SBs-AGN) and purely star-forming SBs (SBs-SFR). From visual inspection of the HST-UV morphology, the two classes have statistically different morphologies: SBs-SFR are generally irregular systems, while a large majority ($\sim 65\%$) of SBs-AGN are instead dominated by regular compact and symmetric morphologies. Searching in the ALMA public archive, I found continuum counterparts with a secure detection above 3σ for 24 galaxies (10 SBs-AGN and 14 SBs-SFR). Then, dust and total molecular gas masses are computed, finding that SBs turn to be gas rich systems ($f_{gas} = 45\% - 85\%$), with similar gas fractions in the two classes, and therefore no direct evidence of AGN feedback depleting the parent hosts. This results are discussed in the context of the co-evolution scenario. The SB population is consistent with a mixture of: low-mass primordial galaxies, rapidly accreting their M_* together with their M_{BH} (mainly the more compact SBs-AGN), and a class of highly star-forming merging systems (dominating the SBs-SFR). Anyway, feedback effects have not reduced yet the f_{gas} of the objects. Alternatively, feedback processes (in form of galactic outflows from the SMBH) are not

efficient enough to significantly deplete the gas masses of the host galaxies.

Contents

Listing of figures

Acknowledgments

1

Introduction

One of the main frontiers of astrophysical investigation concerns the history of how the Universe evolved from small perturbations, imprinted as seeds in the cosmic microwave background, to the complex variety of structures seen nowadays. From star clusters to galaxies to galaxy clusters, the Universe presents a richness that still requires a self-consistent, coherent physical understanding. From the Big Bang to the present day, the shape in which the Universe moulded is the narrative arc of two main characters, gravity and the complex baryon physics. The former is the logos driving the evolution on cosmological scales, generating the filamentary web permeating the Universe, as confirmed by decades of N-body simulations coherently reproducing the large scale structures observed today. The latter becomes a key actor, if not the leading one, on galactic scales, and the complexities underlying its various facets complicate a proper full and comprehensive description of galaxy structure evolution.

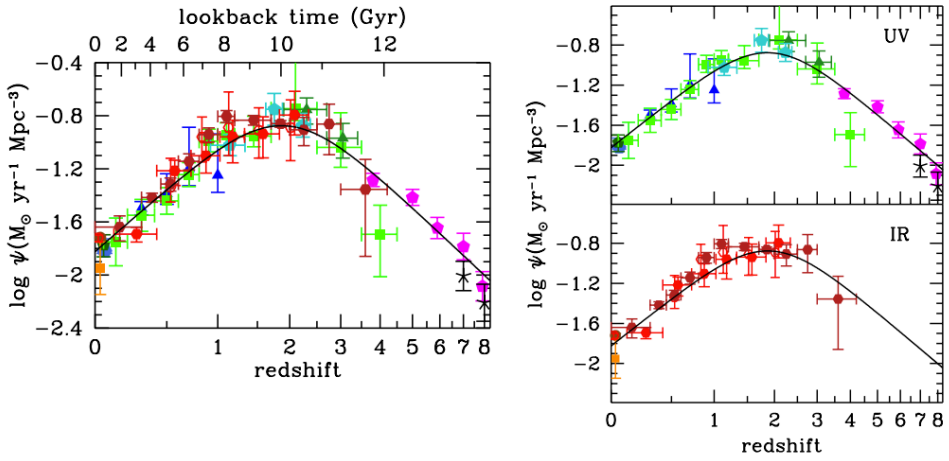

Figure 1.0.1: Cosmic star formation rate history $\log \psi$ as a function of redshift (lower ticks) or lookback time (left panel, upper ticks). Red and dark red points refers to IR measurements, that is, the dust-obscured star formation activity. Green, blue and magenta to FUV measurements, unobscured. Black curve is the best-fit obtained from Eq. 15 in Madau and Dickinson (2014).

The last two decades of investigations have laid some foundations for a chronologically accurate description of galaxy formations, with a number of well established key points, especially in the star formation field. It is now clear that the peak of star formation activity in the history of the Universe occurred about 10 billion years ago, at $z \sim 2$ (Fig. 1.0.1), a time in which the comoving star formation rate densities where a order of magnitude higher than what is observed in the local Universe (see Madau and Dickinson, 2014, and references therein). During this phase, also called the *cosmic noon*, most of the star formation occurred in dusty, obscured environments. In a short amount of time from the initial gas collapse inside the central regions of the dark matter halo, characterized by hectic star formation activity, supernovae explosions of the most massive stars filled these inner regions with dust (hence the acronym *Dust Obscured Galaxies*, DOGs, Blain et al., 1999) in a relatively short amount of time. The star formation processes continued, enshrouded in these obscuring clouds. The energetic UV photons of newborn stars were almost or completely absorbed, heating the dust

to temperatures $T_{\rm dust} = 20 - 80$ K, and then re-emitted in far-IR/sub-mm, making these galaxies extremely brilliant in those bands, a peculiarity that at the time of their discovery led to them being coined *sub-millimetre galaxies*, SMGs (Blain et al., 2002).

At that time, galaxies bright in the sub-mm were thought to be just an extremely rare population in the local Universe, but the increasing amount of data coming from observations of the Hubble Deep Field with the Submillimetre Common-User Bolometer Array (SCUBA, Hughes et al., 1998, Holland et al., 1999) at the James Clerk Maxwell Telescope (JCMT) revealed their commonness at high-z. Thanks to the negative k-correction, the intense sub-mm emission coming from the dust, usually modelled with a modified blackbody law, eased their identification in surveys probing the young Universe. In the past 20 years, various different far-IR to sub-mm/mm surveys (e.g. Smail et al., 1997, Barger et al., 1998, Eales et al., 1999, Vieira et al., 2010, Simpson et al., 2014, 2017), along with numerous single-dish observations with stratospheric balloons and ground telescopes, lifted the curtain on this population, identifying properties such as the extreme star formation rates (i.e. $100 - 1000\,M_{\odot}\,{\rm yr}^{-1}$, the highest found in the Universe, in comparison our Galaxy forms stars at a rate of $1 - 2\,M_{\odot}\,{\rm yr}^{-1}$), peculiar morphologies (i.e. usually clumpy, not smooth), or redshift distribution, peaking at $z \sim 2$ (for an exhaustive review see Casey et al., 2014).

A series of observational evidence points to the fact that these galaxies are the progenitors of the population of Early-Type Galaxies (ETGs) observed in the local Universe. Now passive, massive and without any star forming activity, in their past, at redshifts $z > 1$, these galaxies converted a large amount of gas into stellar mass in a relatively short period of time. Different evolutionary theories have been investigated to explain their observational properties and the quenching mechanisms suppressing star formation, the three main ones being the *merging-driven galaxy evolution*, the *cold stream-driven galaxy evolution* and the *self-regulated baryon collapse scenario*. In the first scenario, gravity dominates also in the star formation field, that is thought to be the consequence of starbursting

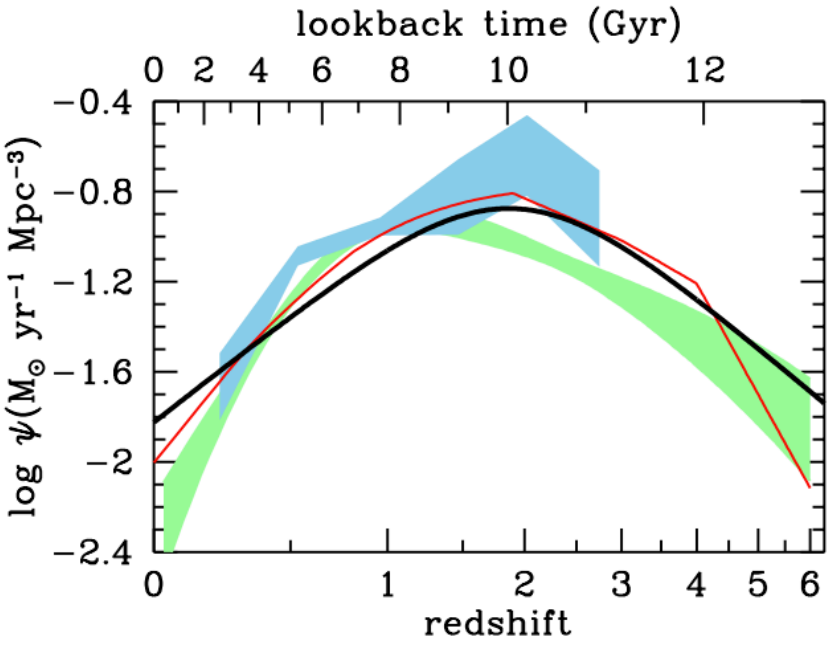

Figure 1.0.2: Black hole accretion and star formation histories in the Universe. The former have been scaled for visual comparison. The solid black curve is the star formation, the red curve and green shade the BHAR from X-ray (Shankar et al. 2009, Aird et al. 2010), the blue shade the BHAR from IR-data (Delvecchio et al 2014). From Madau and Dickinson (2014).

activities due to merging of dark matter halos (Benson, 2010). In the second scenario, high-z star formation is linked to a flow of cold gas from the filamentary streams of the cosmic web to the inner part of the forming galaxies (Dekel et al., 2009). Finally, the last scenario gives more importance to baryonic processes, self-regulated, and primarily fueling star formation, while mergers and galaxy-galaxy interactions play a secondary role in late stages of formation, mainly in order to increase the galaxy mass to the values observed in the local Universe (Granato et al., 2004). In summary, the starbursts observed in the DSFGs are either a consequence of boosted star formation activity due to major mergers, or instabilities of in-situ large amounts of molecular gas, or cold flows from the cosmic web.

At the same time, there is increasing observational evidence that this peak of star formation activity in the high-z Universe is concurrent with the peak of nuclear activity in the innermost part of these galaxies (see Fig. 1.0.2). Different dynamical observations of massive galaxies in the local Universe probed the presence of a quiescent black hole in their nuclear regions. The velocity dispersion of the stars in the galaxy bulge is correlated with the central BH mass. This $M_{\rm BH} - \sigma^*$ relation (Ferrarese and Merritt, 2000, Gebhardt et al., 2000) hints at the existence of a link between the two components in the early stage of the galaxy formation, when starforming processes were taking place at elevated rates. Studies of the BH accretion rate at different redshifts (Shankar et al., 2009, Delvecchio et al., 2015, Mancuso et al., 2016) showed how the two processes seem to peak at the same time. Some evolutionary scenarios (i.e. the SISSA-PADOVA model, Lapi et al., 2018) predict that the co-evolution between the star formation and the nuclear activity in galaxy evolution is crucial to describe their evolution from clumpy, dusty and frantically star forming objects to the massive, quiescent ETGs galaxies observed in today's Universe, i.e. energetic feedback from AGN might be the primary cause that halts star formation in these galaxies. The co-evolution between the central BH during its AGN phase and the star formation in the galaxy is still a challenging topic and needs more data to be addressed in every aspect, such as observations in every region of the electromagnetic spectrum, fundamental to probe the two components, and high-resolution data, especially in the sub-mm, to identify the spatial distribution of the star forming regions with respect to the nuclear activity.

The past two decades of observations have shed light on the DSFGs, revealing their statistical properties thanks to the increasing number of identified galaxies in surveys (Driver et al., 2009, Eales et al., 2010a). Nevertheless, it is still quite a complicated task being able to resolve their full spatial distribution and dynamics at sub-kiloparsec scales, the typical scales at which star formation takes place in the clumpy molecular clouds observed in todays Universe. To resolve those scales in the distant Universe requires extremely high angular resolution and integration times, either for pure imaging or spectroscopic analysis, something

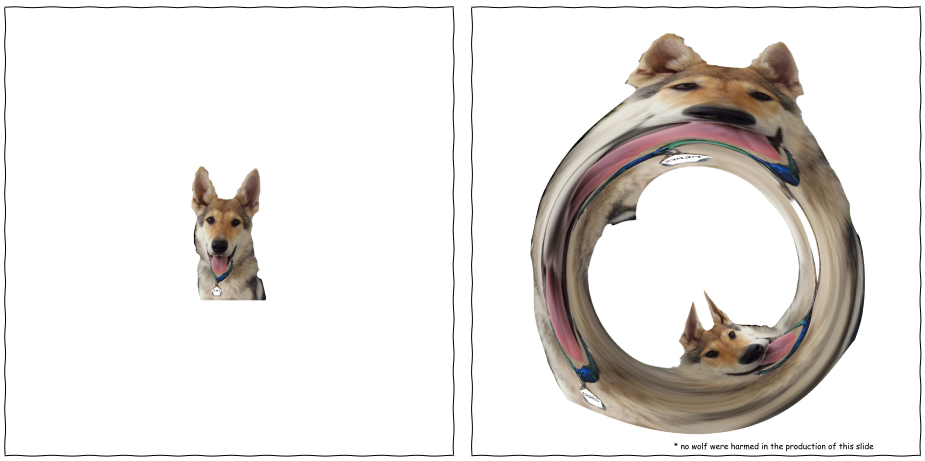

Figure 1.0.3: Gravitational lensing of a DOG, the source plane on the left panel, the image plane on the right panel. The increase in angular resolution is clearly visible, allowing the observer to detect details otherwise hardly readable, such as the writing on the DOG necklace, or the DOG tongue.

that was almost unreachable until the Atacama Large Millimetre/Submillimetre Array (ALMA) became fully operational. Fortunately, the Universe itself provides us a way to investigate those scales, via the effect of gravitational lensing.

Gravitational lensing is a direct consequence of Einstein's General Relativity. As John Archibald Wheeler said in the often cited quote that seizes the heart of Einstein's theory of Gravity, *spacetime tells matter how to move, matter tells spacetime how to curve*. Each distribution of matter/energy in the Universe curves the spacetime structure, and the matter/energy within it is forced to follow the path suggested by its geometry. This synergy within the fabric of the Universe and the Universe itself molds the structures inside it to become that which we see today. Photons are forced to follow the paths suggested by the spacetime curvature, like every massive baryon composed object such as planets, stars or galaxies. In fact, the deflection generated by the Sun on a background star, observed during a solar eclipse in 1919, was the first unequivocal test that probed Einstein's theory as a valid description of gravity.

Apart from the amount of images suitable for the press, gravitational lensing

has two main effects that make it extremely useful in the study of high-z objects (see Fig. 1.0.3). First, there is a measurable increase in the observed flux of a background source. Photons that otherwise would have been undetectable are bent towards the observer, and therefore are detected. Coming with this, and strictly connected to the fact the surface brightness is always conserved in a gravitational lensing event, there is also an increase in angular resolution. A foreground gravitational lens can generate multiple images of the background source, stretched over a large area. Therefore, as a magnifying glass, a gravitational lens is able to unveil finer details than the ones detected with a direct observation. The combination of these effects allows otherwise impossible studies of physical and morphological properties of high-z galaxies.

In order to have a lensing event, a geometrical alignment between the background source, the foreground lens and the observer is mandatory. For this reason, these events are quite rare to observe. Historically, the first detections of gravitationally lensed objects happened serendipitously. The first was in 1979, with the source SBS 0957+561 A/B, best known as the *Twin Quasars* (Walsh et al., 1979). It is composed of two quasars, separated by 5.7 arcsec, with the same magnitudes and redshifts $z = 1.413$. Spectroscopic analysis concluded that the two sources were multiple images of the same object. From that moment on, gravitational lensing became a proper scientific subject: in 1986 the first gravitational arcs in galaxy clusters were detected (Soucail et al., 1988), in 1988 the first Einstein ring (Hewitt et al., 1988), in 1989 and 1990 the first microlensing (Irwin et al., 1989) and weak lensing (Tyson et al., 1990) measurements.

The first attempts to identify gravitationally lensed sources apart from serendipity came from careful analysis of photometric and spectroscopic large-scale surveys. One of the first examples is the Sloan Lens ACS Survey (SLACS, Bolton et al., 2004, see Fig. 1.0.4). By taking advantage of the great volume of spectroscopic data in the Sloan Digital Sky Survey (SDSS, more than 3 millions spectra), SLACS was able to identify numerous candidate gravitational lensing events in the visible band, by simply detecting the presence of multiple

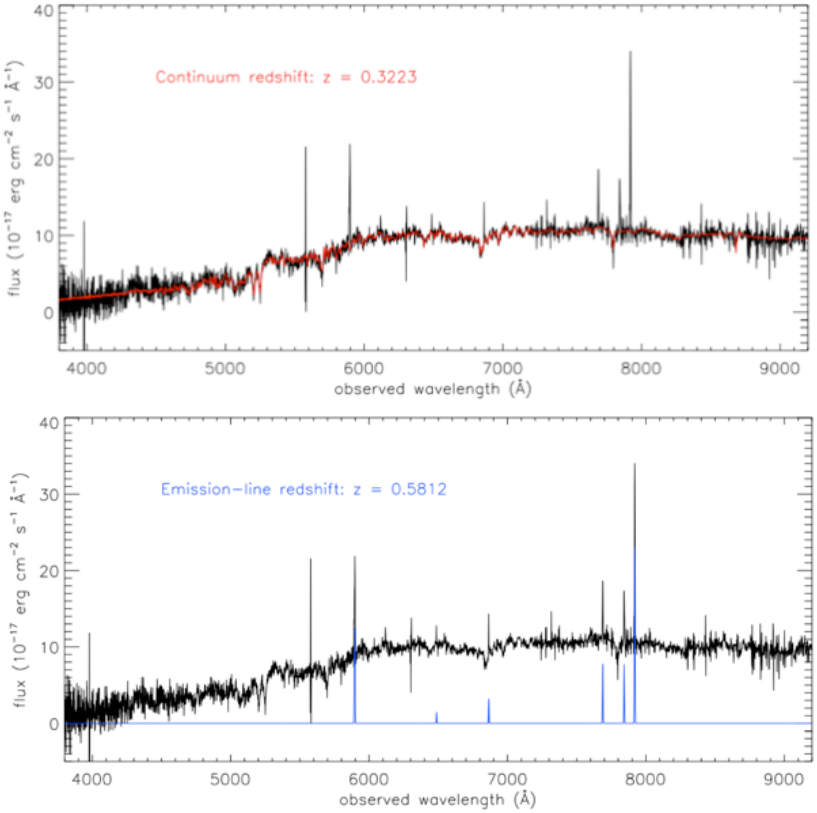

Figure 1.0.4: SLACS source spectrum example. *Upper panel*: continuum emission coming from the foreground galaxy, acting as a lens. *Lower panel*: emission lines from the background galaxy. From SLACS website: www.slacs.org.

redshift components in the same spectrum, both belonging to the same line of sight. These candidates were subsequently observed with the ACS instrument on HST, confirming 70 of them.

On the other side of the electromagnetic spectrum, the Cosmic Lens All-Sky Survey (CLASS) discovered 22 strongly lensed AGN focusing on radio imaging (Browne et al., 2003).

Starting from the casual discovery of SMMJ2135-0102, also known as the *Cosmic Eyelash*, a $z = 2.3259$ sub-mm galaxy magnified 30 times by a galaxy

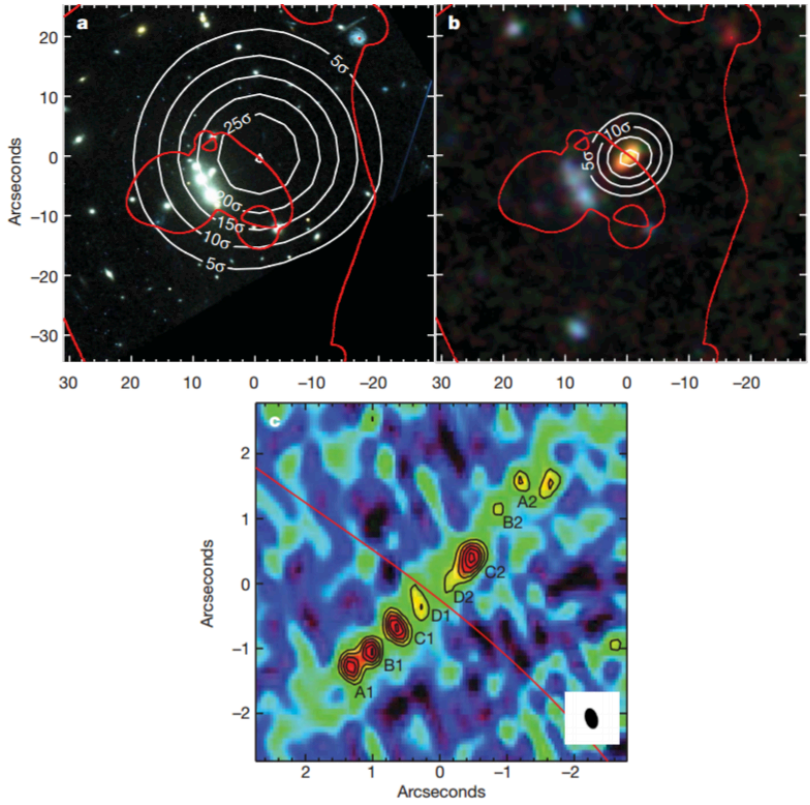

Figure 1.0.5: The Cosmic Eyelash, as observed in different bands. *Panel a)* is the HST data, white contours refers to the LABOCA/APEX 870μm emission, red contours to the cluster critical lines. *Panel b)* are observations at 3.6, 4.5 and 8.0 μm of the cluster, white contours are the 350μm Submilliter APEX Bolometer Camera (SABOCA) detected emission. *Panel c)* is a close up of the *b)* panel, the LABOCA observation: A, B, C and D components are single resolved starforming region, spaced along 1.5 kpc. The red line is the cluster critical line. From Swinbank et al. (2010).

cluster at $z = 0.325$ (Swinbank et al., 2010, see Fig. 1.0.5), an increasing number of strongly lensed sub-mm sources were discovered. It is worth noticing that a great advantage coming from far-IR/sub-mm observations of strongly lensed sources is that, since the lens is usually a massive elliptical local galaxy, with no gas or dust, the signal coming from the source is virtually uncontaminated from the foreground lens emission, while at near-IR bands it is necessary to properly fit and remove the lens emission before attempting any lens modelling. From 2010, a systematic way to identify DSFGs in sub-mm/mm surveys has been developed and successfully tested. The integral number counts of these sources show a steep decline over a certain flux limit, i.e. 100 mJy at 500μm. Whenever an object is detected over that limit in a sub-mm survey, apart from contaminants such as local spiral galaxies or blazars, the remaining possibilities are (an extremely rare) Hyper Luminous InfraRed Galaxy (HYLIRG), or a typical DSFGs whose flux has been boosted by gravitational lensing. Statistical analysis predicts that the surface density of these sources is lower than 0.5 deg^{-2} (Negrello et al., 2007), so in order to select a satisfactory sample, surveys covering a significant fraction of the sky are necessary. That is the case in the Herschel Astrophysical Terahertz Large Area Survey (H-ATLAS, Eales et al., 2010a), a 550 deg^2 extragalactic survey undertaken by the Herschel Space Observatory (Pilbratt et al., 2010). In the H-ATLAS survey, 80 candidate lensed galaxies were discovered, 21 of which have been confirmed as strong lenses by various follow-up observations (e.g. Enia et al., 2018, Bussmann et al., 2013, Negrello et al., 2010, Bussmann et al., 2012, Fu et al., 2012, Messias et al., 2014, Calanog et al., 2014). Ten possess multiple redshifts along the same line-of-sight, only one has been confirmed to be a binary system of HyLIRG (Ivison et al., 2013). Numerous follow-up campaigns are underway to confirm the strong lensing nature of the whole catalogue, in different domains of the electromagnetic spectrum (i.e. HST-SnapShots, P.I. Marchetti, SMA observations, P.I. Negrello, ALMA snapshot imaging, P.I. Eales), with the best-known example being the ALMA high-resolution observations of H-ATLAS J090311.6+003906, a $z = 3.042$ galaxy also known as SDP.81 (Fig. 1.0.6).

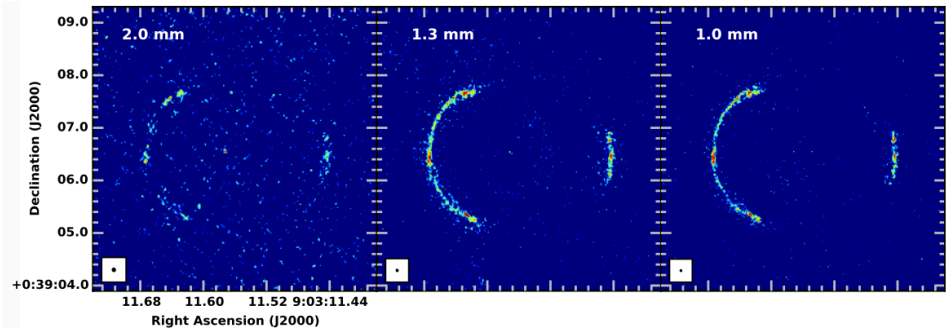

Figure 1.0.6: ALMA high-resolution observations of SDP.81. observed with ALMA. From left to right, the panels are continuum observations in Band 4 (2.0 mm), Band 6 (1.3 mm) and Band 7 (1.0 mm). Bottom left squares in each panel is the synthesized beam, the smallest being 31x23 mas. From ALMA Partnership et al. (2015).

However, for as good as lensing can be in allowing otherwise inaccessible angular resolutions, fundamental for detailed studies of DSFGs, the result of a strong lensing phenomenon is always a multiply imaged, distorted and stretched image of the source. In order to exploit these advantages, it is fundamental to properly model the lens mass distribution, and reconstruct the original source morphology, techniques that go under the name *lens modelling methods*. There are mainly two classes of methods. First there are the full-parametric methods, that model both the lens and the source mass distribution with analytic profiles such as Single Isothermal Ellipsoid for the lens and a Sérsic profile for the background source. Due to the clumpy, irregular morphologies of the DSFGs, these methods are not well-suited to achieve satisfying results. For these kind of sources, it is necessary that the morphologies are retrieved without any analytic pre-assumption, i.e. by considering each pixel in the source plane as a free parameter. This does not translate into an enormous parameter space, since the mathematics that lies behind a semi-parametric method such as the SemiLinear Inversion (SLI, Warren and Dye, 2003, Nightingale and Dye, 2015) is able to retrieve the source counts from the observed image counts with a simple algebraic expression, once the lens mass distribution, still modelled with an

analytic profile like the SIE, is set. The lens parameters that best describe the mass distribution are then retrieved in the parameter space using a Bayesian analysis (Suyu et al., 2006).

The main focus of this work is the sub-mm Universe. Observations carried out in far-IR/sub-mm/mm bands with single-dish telescopes of diameter D are affected by the angular resolution set by the diffraction limit $\theta \propto \lambda/D$. In order to properly resolve the details of DSFGs (or even the lensing features such as multiple images alone), resolutions of the order of 1 arcsec are needed. In those bands, resolutions of this kind are achieved with interferometry. An interferometer is an array of telescopes, and the best achievable angular resolution is set by the maximum distance between two telescopes, called baseline B, so $\theta \propto \lambda/B$. An interferometer does not directly measure the source surface brightness, rather a complex quantity called *visibility* that is the correlated signal coming from the different array baselines. These *visibilities* are sampled on a plane called the *uv* plane. The surface brightness pattern in the sky is the Fourier transform of the visibilities on this plane. The better the sampling of the *uv* plane, the better the retrieved image. Obviously, a perfect sampling of the *uv* plane is hard to achieve, and usually requires high integration times, so the retrieved image will suffer from setbacks such as correlated noise, or ghost features that come from the *uv* plane undersampling rather than real structures in the observed source. As a consequence, it is dangerous to perform lens modelling on the Fourier transformed image coming from an interferometer, since the method might confuse a ghost feature for a real structure. The worse the *uv* sampling in the Fourier space, the worse the solution coming from a real plane approach to lens modelling will be. It is mandatory to extend the methods of the lensing analysis to directly deal with visibilities to achieve a proper lens modelling.

When I started the PhD, there were no publicly available codes that exploited the advantages of the SemiLinear Inversion directly modeling in the *uv* plane. I developed my own code, based on the SLI method, and extended it to deal directly with visibilities. The Methodology behind the code is outlined in Chapter 2. Thorough this work, I use this version of the SLI to perform lens

modelling on multiwavelength data of H-ATLAS discovered sub-mm sources.

In Chapter 3 I applied the code to a sample of 12 SMA H-ATLAS selected sources observed with SMA. Eleven of these sources were already modelled with a full-parametric method by Bussmann et al. (2013). I report the observation of five extra sources, observed in 2017 with SMA, one of which possesses a resolution high enough to resolve multiple images, and allow lens modeling. I reassessed the previous findings on the sample magnifications and sizes, results presented in Enia et al. (2018).

In Chapter 4 I applied the code to multiwavelength observations of HATLASJ090740.0−004200, observed with HST at 1.6μm, ALMA at 1.3 mm, and Chandra in X-ray, while presenting image plane observations in the same bands for another source, HATLASJ091043.0−000322, whose lens modelling is complicated by the presence of a nearby spiral galaxy exerting a strong source of external shear (Massardi, Enia et al., 2018). In particular, the X-rays data probed the presence of a buried AGN in both galaxies, co-spatial within ~ 400 pc with the sub-mm emission for HATLASJ090740.0−004200, a result that sheds light on the angular scales of the co-evolutionary scenario previously mentioned, and probes the importance of gravitational lensing in studies of these kind of sources.

In Chapter 5 I worked with archival ALMA data of starburst galaxies in the COSMOS field (Rodighiero, Enia et al., in prep), aiming to compare the gas properties of the AGN dominated starburst with those of the non-AGN starburst, in order to infer the presence of a difference between the two populations in terms of gas content and morphologies.

2

Methodology

Sub-mm galaxies are the key to understand the build-up of galaxies we see in the Universe today, and gravitational lensing is a tool that allows us to probe otherwise inaccessible details of those galaxies. But the outcome of a gravitational lensing event is a distorted image, with light coming from a background source bent into shapes resembling rings and arcs, with typical sizes of $2'' - 3''$. In order to obtain phenomenological information on sub-mm galaxies from gravitational lensing, the original morphology has to be retrieved, by modelling the mass distribution that generates the distortion. Moreover, the sub-mm part of the spectrum is probed at sub-arcsec resolutions with interferometers rather than single-dish telescopes. An interferometer does not directly measure the surface brightness of the source, but instead it samples its Fourier transform, named the *visibility function*. As such, the lens modelling of interferometric images needs to be carried out in Fourier space in order to

minimize the effect of correlated noise in the image domain and to properly account for the undersampling of the signal in Fourier space, which produces un-physical features in the reconstructed image.

This Chapter is committed to the Methodology that lies behind strong lensing source reconstruction techniques. A brief introduction on interferometry is provided, followed by the mathematical framework adopted by the SemiLinear Inversion Method (Warren and Dye, 2003), a semi-parametric method to model the mass distribution of the lens while searching for the background source original morphology without any analytic pre-assumption on its distribution. Then I extended the method to deal directly with visibility data. Finally, I report on the Bayesian approach to the method which allows us to obtain the best-fit lens parameters.

2.1 Principles of Interferometry

Every astrophysical observation of any object in the Universe, whatever the target is, is affected by a series of errors and setbacks that reduce the quality of the observation itself. The best-known example is *seeing*: atmospheric turbulence distorts wavefronts coming from a distant source, with consequences as flux scintillation, image motion or source profile enlargement. The combination of these effects reduces the achieved spatial resolution θ of the observation, θ being the minimum angular separation at which two point sources can still be distinguished. Common ways to overcome this issue vary from the implementation of adaptive optics, that reconstruct the unperturbed wavefront by sampling the atmospheric perturbation, or observing from space, removing the atmosphere altogether.

However, even removing each possible source of turbulence or nuisance, the best-achievable angular resolution by a telescope of diameter D is physically fixed by the diffraction limit, $\theta \propto \lambda/D$, λ being the wavelength of observations. Resolution gets better by increasing the telescope aperture, while at a fixed aperture size, observations made at longer wavelengths will suffer a worse spatial

resolution than those made at shorter wavelengths.

This issue is usually less considered when observing at optical or near-infrared bands, since atmospheric turbulence or any other nuisance dominates the diffraction limit, but becomes important when observing in far-infrared, sub-millimetre/millimetre bands or in the radio. In this case, it's technically impossible to reach the same angular resolution achieved with near-infrared observations with a single dish telescope, since that would require a collector with a diameter as big as tens of kilometers, for the wavelength domain being three or four order of magnitude bigger.

Interferometry overcomes this issue. Since observing with a single big photon collector is technically unfeasible, the technique employs a number of single receivers acting as a bigger collector, called *array*, that correlates the signal coming from the single antennas. The distance between a single couple of antennas is called *baseline B*, and an interferometer best-achievable angular resolution is a function of the maximum baseline: $\theta \propto \lambda/B$.

2.1.1 Visibility function

Obviously, interferometry is not as easy as it appears. Observing with 60 10-meters antennas with a maximum baseline of 10 kilometers is not exactly the same as observing with a 5 kilometer single-dish telescope. First, the collecting area of an array is obviously lower than the collecting area of a single-dish, so a longer integration time is needed to fully collect an acceptable amount of photons from the desired source. As such, a high number of antennas and a proper amount of integration time are necessary to obtain a trustworthy image of the observed source. Then, the measured signal is a correlation made between the baselines, so an interferometer doesn't directly measure a surface brightness pattern in the sky, but an interference pattern, also known as *fringe visibility* or *visibility function* or *visibility*.

The distance $\Delta\theta$ between two consecutive peaks of the visibility function - that is the achieved angular resolution - has a linear dependence on the observed

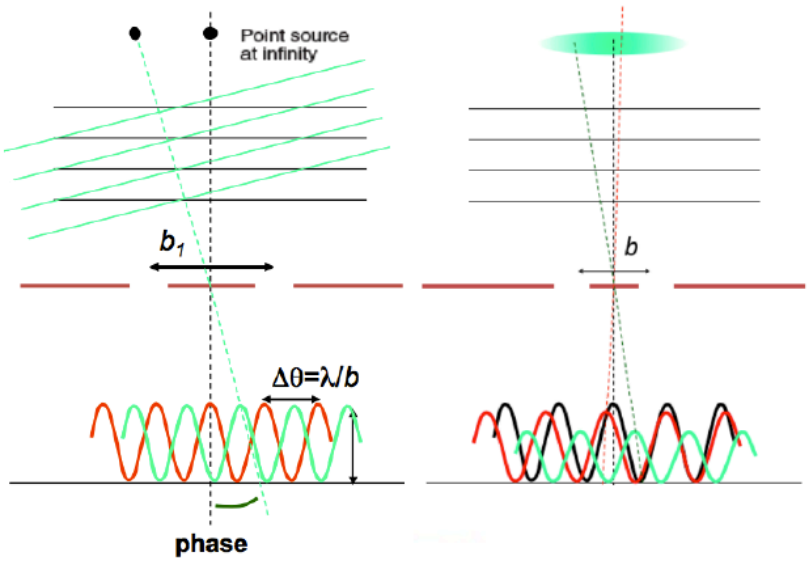

Figure 2.1.1: Phase and amplitude in an interferometric image. *Left panel*, the same source observed at two different positions in the sky: the measured signal has the same amplitude, and it's basically the same except for a phase offset. *Right panel*, an extended source, observed in three different directions, with a decreasing flux from the image center, affecting the signal amplitude. Credits: Italian ARC.

wavelength λ and on the array baseline B: $\Delta\theta \propto \lambda/B$. Visibility contains the surface brightness information observed at a precise spatial frequency obtained from $\Delta\theta$. As a consequence, **shorter baselines probe wider angular scales, longer baselines probe smaller angular scales**.

Two fundamental quantities in interferometry, which enter the visibility function, are the signal amplitude A, that is connected to the source flux, and the signal phase φ, that is connected to the direction the signal is coming from (Fig. 2.1.1).

Let's assume an array composed of two antennas, observing the same source. An electromagnetic wave detected by the two receivers induces a potential U on both:

$$U_1 \propto Ee^{i\omega t} \qquad U_2 \propto Ee^{i\omega(t-\tau)} \tag{2.1}$$

where τ is the geometric delay, necessary to be certain that the same wavefront is being considered, and is related to the baseline dimension B and the observed direction s:

$$\tau = \frac{B \cdot s}{c}. \tag{2.2}$$

The signal is then correlated by a correlator. The correlator multiplies the two signals, and integrates them along the integration time T, giving the correlated signal

$$R(\tau) \propto \frac{E^2}{T} \int_0^T e^{i\omega t} e^{-i\omega(t-\tau)} dt. \tag{2.3}$$

Then

$$dR(\tau) \propto E^2 e^{i\omega\tau} dt \propto dP e^{i\omega\tau}. \tag{2.4}$$

The power induced by the source, in terms of radiation intensity I and the subtended solid angle in the direction s is

$$dP = I_\nu \cos\theta d\Omega d\sigma d\nu = A(s) I_\nu(s) d\Omega d\nu, \tag{2.5}$$

where $A(s)$ is the effective collecting area of each antenna, i.e. the primary beam.

The correlated signal becomes

$$dR_{12} = A(s) I_\nu(s) e^{i\omega\tau} d\Omega d\nu. \tag{2.6}$$

Once integrated along the source dimension and the bandwidth, the signal becomes the visibility function

$$V = \int_\Omega \int_\nu A(s) I_\nu(s) e^{i2\pi\nu(B\cdot s/c)} d\Omega d\nu. \tag{2.7}$$

This is the quantity measured by an interferometer, and from now on will be referred as **visibility**.

Obviously, visibility is not the much desired surface brightness. Luckily, the two are linked by the Van Cittert-Zernike theorem: **the surface brightness pattern in the sky is the Fourier-transform of the measured visibilities**

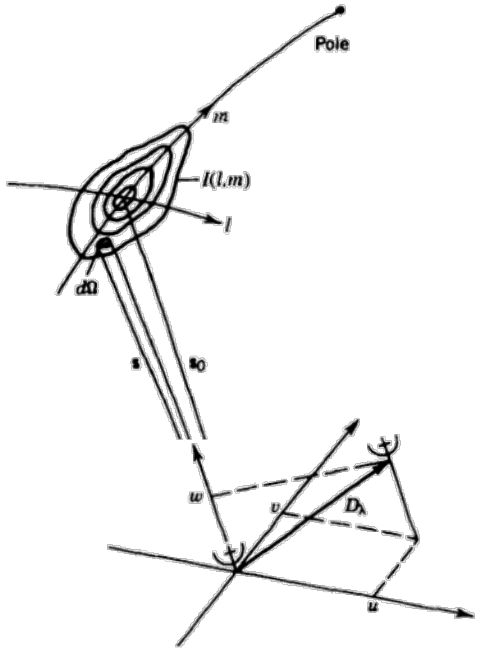

Figure 2.1.2: Interferometry fundamental planes: the surface brightness *xy* plane (or real plane) and the Fourier corresponding *uv* visibility plane. The latter is also interpreted as the way the source sees the interferometer. Credits: Wilner D., *13th Synthesis Imaging Workshop*.

sampled on the visibility space. Image space is instantly defined as a function of the coordinates x and y defined on the sky, related to the object right ascension α and declination δ, while visibility space is defined as a function of the coordinates u and v (from which the acronym *uv* plane), and they are connected via Fourier transformation

$$V(u,v) = \int\int A(x,y)I(x,y)e^{-2\pi i(ux+vy)}dxdy \tag{2.8}$$

$$I(x,y) = \int\int P(u,v)V(u,v)e^{2\pi i(ux+vy)}dudv \tag{2.9}$$

A measure of intensity on the *uv* visibility plane is the same as the Fourier

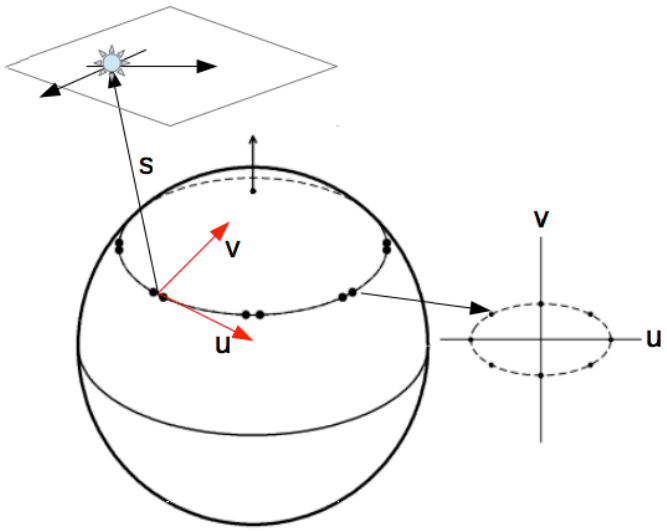

Figure 2.1.3: How interferometry exploits the Earth's rotation to obtain a more complete sampling of the *uv* plane, expecially when it's not possible to use a high number of antennas. While time flows, the baseline projection on the plane generates an ellipse, whose axis ratio is related to the geographic latitude of the interferometer (the ellipse becomes a circle at the equator, a point at the Pole). Image adapted from *Essential Radio Astronomy, J. J. Condon and S. M. Ransom*.

transform of the surface brightness measured in the sky.

At a fixed position, a single baseline is a point in the *uv* plane, that is the projection of the distance between two antennas. Every baseline corresponds to a point in the *uv* plane, so for given N antennas, there are $N(N-1)/2$ independent baselines, corresponding to $N(N-1)/2$ points in the *uv* plane. Actually, the *uv* plane being a complex plane, the complex conjugate of each point in the corresponding $-u-v$ plane also exists, so the total number of points is $N(N-1)$. Each of these points corresponds to a measure of the visibility, that is the Fourier transform of the surface brightness. **In order to obtain an image that is the most faithful representation of the sky, it is necessary that the *uv* plane gets uniformly sampled, and then anti-transformed in the image plane**. In order to sample properly the *uv* plane, there are two principal

arrangements. The first is to observe with a high number of antennas. The second, once the *uv* plane is sampled by the baseline-projection in the sky, exploits the Earth's rotation: as such, while the Earth moves, the points in the *uv* plane move describing ellipses in the plane, increasing the sampling (technique known as *aperture sampling*, as shown in Fig. 2.1.3). The better the sampling, the better the retrieved surface brightness pattern in the sky.

Unfortunately, as good as the sampling can be, the retrieved image will suffer typical interferometric features such as correlated noise, side lobes and setbacks coming from the non sampled regions of the *uv* space that can be mistaken as source substructure by the most sophisticated lens modeling techniques. That is the reason behind the need for extending the lens modelling formalism to directly deal with visibilities, as I will show in the forthcoming sections.

2.2 Lens modeling techniques

As shown in the first Chapter, gravitational lensing is now a key tool to investigate the structures in the Universe, whether in the lens or in the source. High-redshift galaxy structures become accessible thanks to the magnification generated by a foreground mass distribution on a background source. Intrinsically faint objects suddenly become detectable. In theory, it is just a matter of finding these lensing events.

In order to exploit these advantages, it is fundamental that a proper lens modeling is adopted, extracting every useful piece of information from the lensing phenomena. Historically, two main approaches to this problem have been used: the so-called fully-parametric methods and the semi-parametric methods.

The first class of methods, (e.g. GRAVLENS, GLAFIC, Keeton, 2011, Oguri, 2010), describes both the lens and the source with analytic models (i.e. a Singular Isothermal Ellipsoid for the lens, a Sérsic profile for the background source). The best-fit parameters are obtained by minimizing the χ^2 between the observed counts in the sky and some model counts obtained by lensing the

parametrized source:

$$G = \frac{1}{2}\chi^2_{im} = \frac{1}{2}\sum_{j=1}^{\mathcal{J}} \left(\frac{\sum_{i=1}^{\mathcal{I}} d_j^{\text{model}} - d_j}{\sigma_j} \right)^2 , \tag{2.10}$$

where $d_j \pm \sigma_j$ are the observed counts in the image plane with associated noise, and d_j^{model} the model counts.

This approach suffers from two main issues. First, there is no assurance that the background source is actually best described by a (single) Sérsic profile, especially in the case of sub-mm sources. A way to overcome this is by using multiple different profiles, but that leads to the second (bigger) problem: the higher the number of parameters, the bigger the parameter space to explore, leading to degeneracies. This makes the fully-parametric methods computation-heavy and time-consuming, with no assurance that the desired solution is trustworthy.

2.2.1 The adaptive semilinear inversion method

That is the reason why semi-parametric methods were developed in the past 20 years. These methods avoid any analytic assumption on the source intrinsic morphology, and attempt the reconstruction by assuming a pixellated source brightness distribution, treating each pixel (in principle) as a free parameter.

In this Thesis I follow the Regularized Semilinear Inversion (SLI) method introduced by Warren and Dye (2003). This method assumes a pixellated source brightness distribution, and also introduces a regularization term to control the level of smoothness of the reconstructed source. The method was improved by Suyu et al. (2006) using Bayesian analysis to determine the optimal weight of the regularization term and by Nightingale and Dye (2015) with the introduction of a source pixelization that adapts to the lens model magnification. Here I adopt all these improvements and extend the method to deal with interferometric data. I provide a summary of the SLI method, but I refer the reader to Warren and Dye (2003) for more details.

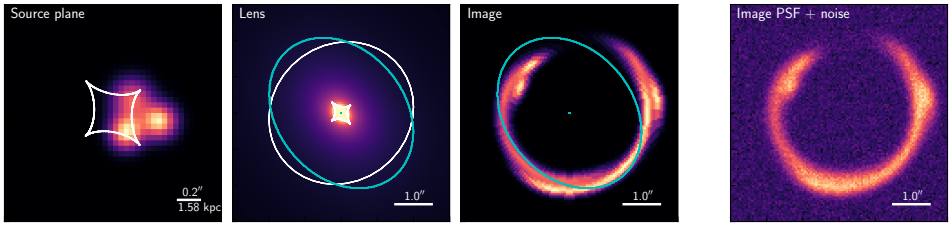

Figure 2.2.1: A simulated lensed source. *Left panel*: a simulated cluster of three sources, lensed with a SIE model lens (*center-left*). The result is a lensed source (*center-right*), then convolved with an instrumental PSF and with noise added to simulate an observation (*right panel*).

The image plane (IP) and the source plane (SP), i.e. the planes orthogonal to the line-of-sight of the observer to the lens containing the lens and the background source respectively (see Fig. 2.2.1), are gridded into pixels, whose values represent the surface brightness counts. In the IP, the pixel values are described by an array of elements d_j, with $j = 1, \ldots, J$, and associated statistical uncertainty σ_j, while in the SP the unknown surface brightness counts are represented by the array of elements s_i, with $i = 1, \ldots, I$. For a fixed lens mass model, the IP is mapped to the SP by a unique rectangular matrix f_{ij}. The matrix contains information on the lensing potential, via the deflection angles, and on the smearing of the images due to convolution with a given point spread function (PSF). In practice, the element f_{ij} corresponds to the surface brightness of the j-th pixel in the lensed and PSF-convolved image of source pixel i held at unit surface brightness. The method aims at evaluating the vector, $\mathbf{S}$, of elements s_i that best reproduces the observed IP. In the following sections, the lens parameters used to retrieve the reconstructed source are fixed to the best-fit values.

2.2.2 Without regularization

S is found by minimizing a proper merit function. In the non-regularized case, this function is:

$$G = \frac{1}{2}\chi^2_{im} = \frac{1}{2}\sum_{j=1}^{\mathcal{J}}\left(\frac{\sum_{i=1}^{\mathcal{I}} s_i f_{ij} - d_j}{\sigma_j}\right)^2 \tag{2.11}$$

In order to obtain the minimum of the merit function, I have to derive it with respect to the source terms s_i and find the zeroes:

$$\frac{\partial G}{\partial s_i} = \sum_{j=1}^{\mathcal{J}}\left[\frac{f_{ij}(\sum_{k=1}^{\mathcal{I}} s_k f_{kj} - d_j)}{\sigma_j^2}\right] = 0 \tag{2.12}$$

This produces a set of I equations. Eq. 2.12 can be rewritten in matrix form[1]. If I define the following vectors:

$$\mathbf{S} = [s_1, s_2, ..., s_{\mathcal{I}}] \tag{2.13}$$

$$\mathbf{D} = \left[\sum_{j=1}^{\mathcal{J}}\frac{f_{1j}d_j}{\sigma_j^2}, \sum_{j=1}^{\mathcal{J}}\frac{f_{2j}d_j}{\sigma_j^2}, ..., \sum_{j=1}^{\mathcal{J}}\frac{f_{\mathcal{I}j}d_j}{\sigma_j^2}\right], \tag{2.14}$$

and the matrix **F** with elements

$$[\mathbf{F}]_{ik} = F_{ik} = \sum_{j=1}^{\mathcal{J}}\frac{f_{ij}f_{kj}}{\sigma_j^2}, \tag{2.15}$$

then Eq. (2.12) can be written as

$$\sum_{k=1}^{\mathcal{I}} F_{ik}\cdot s_k = D_i \Longrightarrow \mathbf{F}\cdot\mathbf{S} = \mathbf{D} \tag{2.16}$$

[1] Given a matrix A of dimensions $m \times r$ and elements a_{ij}, and a matrix B of dimensions $r \times n$ and elements b_{ij}, their product is a matrix C of dimensions $m \times n$ and elements $c_{ij} = \sum_{p=1}^{N} a_{ip}b_{pj}$

Therefore, the most likely solution for the source surface brightness counts can be obtained via a matrix inversion

$$\mathbf{S} = \mathbf{F}^{-1}\mathbf{D}. \tag{2.17}$$

In Eq. (2.17) lies the heart of the method, showing how the minimum of the χ^2_{im} is obtained via a matrix product of two linear matrices, one of which is inverted. Even though in principle each pixel is a free parameter, this does not translate into an immense parameter space, since the best-fit solution is obtained algebraically. This leaves the lens model parameters as the unknowns to be determined. This is achieved exploiting MonteCarlo techniques, that I will describe in detail in the final section of the Chapter.

Deriving again Eq. (2.12), $\mathbf{F}$ corresponds to the χ^2_{im} Hessian:

$$\frac{\partial^2 G}{\partial s_i \partial s_k} = \sum_{j=1}^{\mathcal{J}} \frac{f_{ij} f_{kj}}{\sigma_j^2} = \mathbf{F} \tag{2.18}$$

Lastly, the covariance matrix, whose diagonal terms are the uncertainties on the reconstructed source counts. The covariance between two independent pixels in the SP, i and k, is:

$$\begin{aligned} \sigma^2_{ik} &= \sum_{j=1}^{\mathcal{J}} \sigma_j^2 \frac{\partial s_i}{\partial d_j} \frac{\partial s_k}{\partial d_j} \\ &= \sum_{j=1}^{\mathcal{J}} \sigma_j^2 \sum_{l=1}^{\mathcal{I}} R_{il} \frac{f_{li}}{\sigma_j^2} \sum_{m=1}^{\mathcal{I}} R_{km} \frac{f_{mj}}{\sigma_j^2} \\ &= R_{ik} \end{aligned} \tag{2.19}$$

with $\mathbf{R} = \mathbf{F}^{-1}$.

In the form outlined here, the method may produce unphysical results. In fact, each pixel in the SP behaves independently from the others and, therefore, the reconstructed source brightness profile may show severe discontinuities and pixel-to-pixel variations due to the noise in the image to be modelled (Fig. 2.2.2).

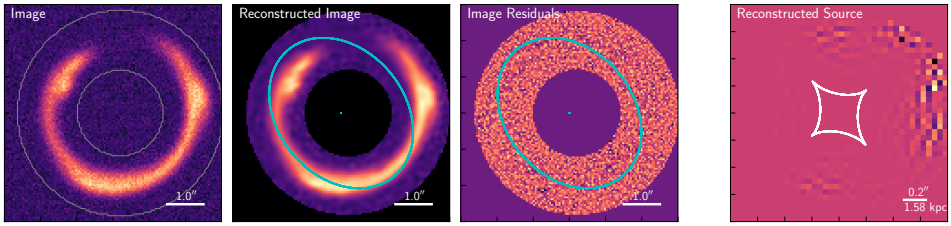

Figure 2.2.2: Reconstructed source without regularization term. Even though the minimum χ^2 reconstructed image plane is indistinguishable from the original image, the reconstructed source is sparse in the source plane.

2.2.3 With regularization

In order to overcome this problem a *prior* on the parameters s_i is assumed, in the form of a regularization term, E_{reg}, which is added to the merit function in Eq. (2.11), and forces a smooth variation in the value of nearby pixels in the SP. It is important to choose a form for the regularization term E_{reg} that preserves the matrix formalism, in particular E_{reg} has to be a linear combination of s_i, s_k terms, such that its partial derivatives are linear in those terms:

$$E_{\text{reg}} = \frac{1}{2}\sum_{i,k} h_{ik} s_i s_k = \frac{1}{2}\mathbf{S}^T\mathbf{H}\mathbf{S} \tag{2.20}$$

In this way, the merit function becomes:

$$G_\lambda = \frac{1}{2}\chi^2 + \lambda E_{\text{reg}} = \frac{1}{2}\chi^2 + \lambda\frac{1}{2}\mathbf{S}^T\mathbf{H}\mathbf{S} \tag{2.21}$$

where λ is the so-called *regularization constant*, which controls the strength of the regularization, and $\mathbf{H}$ is the *regularization matrix*.

There are different ways to define E_{reg}, depending on the level of smoothness required for the reconstructed solution. In this work, I use a gradient form regularization, that is a term that forces immediately nearby pixels not to differ too much from one another. In principle, one can use a curvature form regularization, that forces the source curvature to change minimally in its surface brightness distribution. Here I implemented the first form, being the best choice

between the need of a regularization and the computational cost of the regularization process.

Again, deriving G_λ with respect to the source terms:

$$\frac{\partial G}{\partial s_i} = 0 = \sum_{j=1}^{J} \left[\frac{f_{ij} \sum_{k=1}^{I} s_k f_{kj} - f_{ij} d_j}{\sigma_j^2} \right] + \lambda h_{ik} \sum_k s_k$$

$$\frac{\partial G}{\partial s_i} = \mathbf{FS} - \mathbf{D} + \lambda \mathbf{HS} = 0$$

The minimum of the merit function in Eq. (2.21) satisfies the condition

$$[\mathbf{F} + \lambda \mathbf{H}] \cdot \mathbf{S} = \mathbf{D}, \tag{2.22}$$

and, therefore, can still be derived via a matrix inversion

$$\mathbf{S} = [\mathbf{F} + \lambda \mathbf{H}]^{-1} \mathbf{D}. \tag{2.23}$$

The errors on the reconstructed source surface brightness distribution, for a fixed mass model, are given by the diagonal terms of the covariance matrix (Warren and Dye, 2003):

$$\sigma_{ik}^2 = \sum_{j=1}^{\mathcal{J}} \sigma_j^2 \frac{\partial s_i}{\partial d_j} \frac{\partial s_k}{\partial d_j} = R_{ik} - \lambda \sum_{l=1}^{\mathcal{I}} R_{il} [\mathbf{RH}]_{kl}, \tag{2.24}$$

where $\mathbf{R} = [\mathbf{F} + \lambda \mathbf{H}]^{-1}$. I will use this expression to draw signal-to-noise ratio contours in the reconstructed SP for the best fit lens model. The results are showed in Fig. 2.2.3.

2.2.4 Adaptive pixelization

Even in this form, the SLI method may present some minor issues. A key one comes from the fact the not every region in the source plane is magnified in the

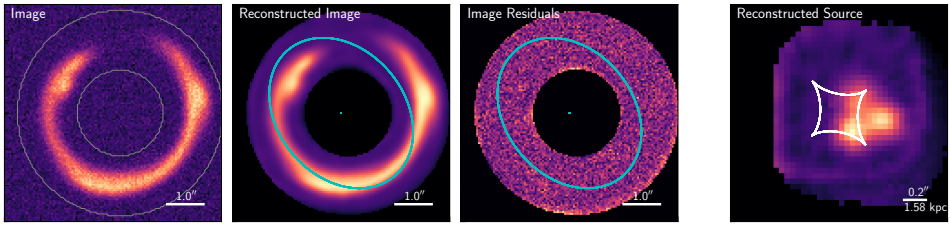

Figure 2.2.3: Reconstructed source with regularization on a grid of square pixels. The regularization term ensures that a physically motivated solution is obtained, avoiding the sparse solution caused by noise overfitting.

image plane by the same amount. Regions close to the caustics will be magnified more than regions that are far away from it. Enclosing all the regions near the caustics into a single pixel lead to some information loss. In theory, it is better to probe these regions with more points. This is the concept behind the adaptive SP pixellization scheme introduced in Nightingale and Dye (2015). For a fixed lens mass model, the IP pixel center are traced back to the SP. Then, a k-means clustering algorithm is used to group them, and define new pixel centres in the SP. These are then used to generate Voronoi cells (for visualization purposes). In this way, more magnified regions will be probed by more cells, and viceversa.

The mathematics behind the method is the same, the only difference is in the adopted regularization term:

$$E_{\text{reg}} = \sum_{i=1}^{\mathcal{I}} \sum_{k=1}^{N_v(i)} (s_i - s_k)^2 \tag{2.25}$$

where $N_v(i)$ are the counts members of the set of Voronoi cells that share at least one vertex with the i-th pixel.

The adaptive pixel scale solution is shown in Fig. 2.2.4. This is an improvement compared to the grid of square pixels shown before.

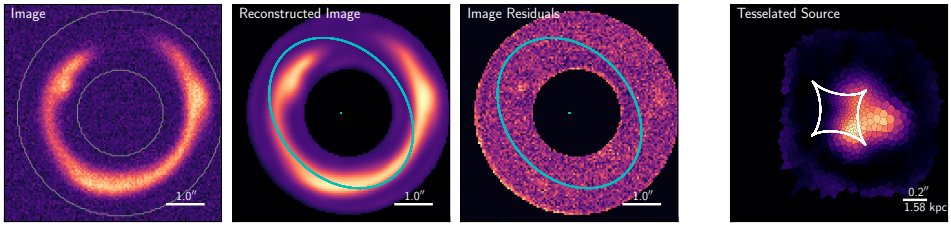

Figure 2.2.4: Reconstructed source with regularization and with adaptive pixel scale.

2.3 Modeling in the uv plane

I extended the adaptive SLI formalism to deal with images of lensed galaxies produced by interferometers.

As shown in the previous Section, an interferometer correlates the signals of an astrophysical source collected by an array of antennas to produce a *visibility function* $V(u, v)$, that is the Fourier transform of the source surface brightness $I(x, y)$ sampled at a number of locations in the Fourier space, or *uv*-plane:

$$V(u, v) = \int \int A(x, y) I(x, y) \mathrm{e}^{-2\pi \mathrm{i}(ux+vy)} dxdy \qquad (2.26)$$

where A is the effective collecting area of each antenna, i.e. the primary beam.

Because of the incomplete sampling of the *uv*-plane the image of the astrophysical source obtained by Fourier transforming the visibility function will be affected by various artifacts, such as side-lobes, correlated noise, non-conserved total flux (Fig. 2.3.1). All these effects compromise the correct application of the SLI method. Therefore, a proper source reconstruction performed on interferometric data should be carried out directly in the *uv*-plane.

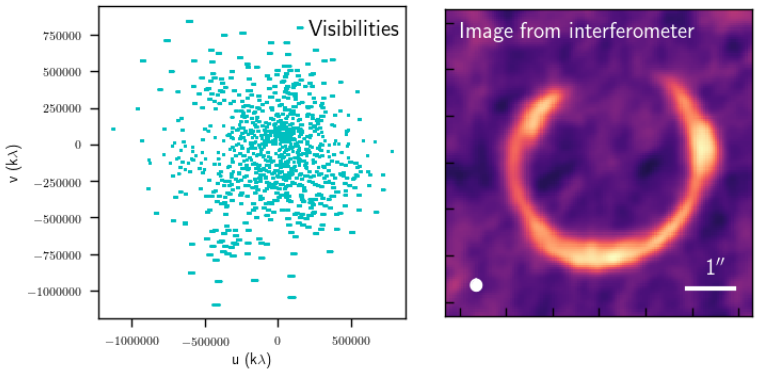

Figure 2.3.1: The same simulated lensed source as before, observed with ALMA. *Left panel*: *uv*-plane sampling. All those unsampled regions generate artifacts in the Fourier-transformed image. *Right panel*: the Fourier-transformed image. The white ellipse on the bottom left is the image synthetized beam.

Let's define the merit function using the visibility function

$$\begin{aligned} G_\lambda &= \frac{1}{2}\sum_{u,v}^{N_{\rm vis}} \left| \frac{V_{\rm model}(u,v) - V_{\rm obs}(u,v)}{\sigma(u,v)} \right|^2 + \lambda \frac{1}{2}\mathbf{S}^T\mathbf{H}\mathbf{S} \\ &= \frac{1}{2}\sum_{u,v}^{N_{\rm vis}} \left(\frac{V^{\mathbb{R}}_{\rm model}(u,v) - V^{\mathbb{R}}_{\rm obs}(u,v)}{\sigma(u,v)} \right)^2 \\ &\quad + \frac{1}{2}\sum_{u,v}^{N_{\rm vis}} \left(\frac{V^{\mathbb{I}}_{\rm model}(u,v) - V^{\mathbb{I}}_{\rm obs}(u,v)}{\sigma(u,v)} \right)^2 \\ &\quad + \lambda \frac{1}{2}\mathbf{S}^T\mathbf{H}\mathbf{S}, \end{aligned} \tag{2.27}$$

where $N_{\rm vis}$ is the number of observed visibilities $V_{\rm obs} = V^{\mathbb{R}}_{\rm obs} + {\rm i}V^{\mathbb{I}}_{\rm obs}$, while $\sigma^2(u,v) = \sigma^2_{\rm real}(u,v) + \sigma^2_{\rm imag}(u,v)$, with $\sigma_{\rm real}$ and $\sigma_{\rm imag}$ representing the 1σ uncertainty on the real and imaginary parts of $V_{\rm obs}$, respectively. With this definition of the merit function I am assuming a natural weighting scheme for the visibilities in the lens modelling.

Following the formalism of Eq. (2.21), I introduce a rectangular matrix of *complex* elements $\hat{f}_{jk} = \hat{f}^{\mathbb{R}}_{jk} + i\hat{f}^{\mathbb{I}}_{jk}$, with $k = 1, .., N_{\rm vis}$ and $j = 1, .., N$, N being the

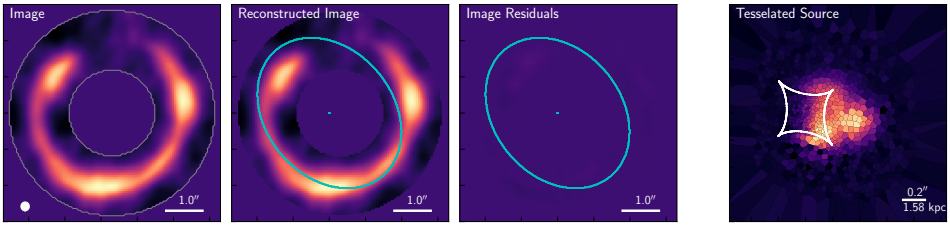

Figure 2.3.2: Background source reconstructed from the visibility data by using the extended SLI method, with the adaptive pixel scale.

number of pixels in the SP. The term $\hat{f}_{jk}$ provides the Fourier transform of a source pixel of unit surface brightness at the j-th pixel position and zero elsewhere, calculated at the location of the k-th visibility point in the uv-plane. The effect of the primary beam is also accounted for in calculating $\hat{f}_{jk}$. Therefore, Eq. (2.27) can be re-written as

$$\begin{aligned} G_\lambda &= \frac{1}{2}\sum_{u,v}^{N_{\rm vis}} \left| \frac{V_{\rm model}(u,v) - V_{\rm obs}(u,v)}{\sigma(u,v)} \right|^2 + \lambda \frac{1}{2}\mathbf{S}^T\mathbf{H}\mathbf{S} \\ &= \frac{1}{2}\sum_{k}^{N_{\rm vis}} \left(\frac{\sum_{j=1}^{N} s_i \hat{f}^{\mathbb{R}}_{jk} - V^{\mathbb{R}}_{{\rm obs},k}}{\sigma_k} \right)^2 \\ &\quad + \frac{1}{2}\sum_{k}^{N_{\rm vis}} \left(\frac{\sum_{j=1}^{N} s_i \hat{f}^{\mathbb{I}}_{jk} - V^{\mathbb{I}}_{{\rm obs},k}}{\sigma_k} \right)^2 \\ &\quad + \lambda \frac{1}{2}\mathbf{S}^T\mathbf{H}\mathbf{S}. \end{aligned} \tag{2.28}$$

In deriving this expression I assume that $\mathbf{S}$ is an array of real values, as it describes a surface brightness.

The set of s_i values that best reproduces the observed IP can then be derived as in Eq (2.23):

$$\mathbf{S} = [\hat{\mathbf{F}} + \lambda\mathbf{H}]^{-1}\hat{\mathbf{D}}. \tag{2.29}$$

with the new matrices $\hat{\mathbf{F}}$ and $\hat{\mathbf{D}}$ defined as follows

$$\hat{\mathbf{F}}_{jk} = \sum_{l=1}^{N_{\rm vis}} \frac{\hat{f}^{\mathbb{R}}_{jl}\hat{f}^{\mathbb{R}}_{lk} + \hat{f}^{\mathbb{I}}_{jl}\hat{f}^{\mathbb{I}}_{lk}}{\sigma_l^2} \tag{2.30}$$

$$\hat{\mathbf{D}}_j = \sum_{l=1}^{N_{\rm vis}} \frac{\hat{f}^{\mathbb{R}}_{jl}V^{\mathbb{R}}_{{\rm obs},l} + \hat{f}^{\mathbb{I}}_{jl}V^{\mathbb{I}}_{{\rm obs},l}}{\sigma_l^2} \tag{2.31}$$

The computation of the errors on the reconstructed source surface brightness distribution is exactly the same as before, by replacing $\mathbf{F}$ and d_J with the corresponding quantities defined in this section.

2.4 A Bayesian wrapper to the SLI method

As showed in the previous section, reconstructing the surface brightness counts in a strong lensing image is a relatively simple task, even when applied directly in the *uv* plane.

The last things to assess are the evaluation of the regularization constant λ, and the search for the best-fit lens model parameters. The Bayesian approach to the method allows us to obtain the regularization constant directly from the data, while classifying the different lens mass models at the same time, in order to find the best-fit parameters that points to the real minimum $\chi^2_{\rm im}$. Here I report the fundamentals of the approach, and refer the reader to Suyu et al. (2006) for further details.

Let's assume that N_d data have been measured, organized into the vector $\mathbf{d}$ of elements d_j, with $j = 1...N_d$. From this data set, I want to obtain the N_s model parameters, defined as s_i with $i = 1...N_s$. The connection between the s_i model parameters and the measured d_j is a matrix $\mathbf{f}$ of dimension $N_d \times N_s$. This matrix will enclose all the information on the assumed lens model, such as the full lens potential ψ. A gaussian noise $\mathbf{n}$ is associated to these data, characterized by a covariance matrix $\mathbf{C}_d$. The relation between these quantities is:

$$\mathbf{d} = \mathbf{fs} + \mathbf{n} \tag{2.32}$$

and the probability that, given the s_i model parameters, the observation returns the d_j measured data is the *likelihood*

$$P(\mathbf{d}|\mathbf{s},\mathbf{f}) = \frac{\exp[-E_D(\mathbf{d}|\mathbf{s},\mathbf{f})]}{Z_D}, \tag{2.33}$$

with Z_D as the normalization and the term E_D

$$E_D(\mathbf{d}|\mathbf{s},\mathbf{f}) = \frac{1}{2}(\mathbf{fs}-\mathbf{d})^T\mathbf{C}_D^{-1}(\mathbf{fs}-\mathbf{d}) = \frac{1}{2}\chi^2 \tag{2.34}$$

that is half of the χ^2.

By definition, the most likely solution $\mathbf{s}_{ML}$, is the one that maximizes the likelihood in Eq. (2.33), or minimizes Eq. (2.34), such that $\nabla E_D(\mathbf{s}_{ML}) = 0$.

Without any regularization scheme applied on the data, the most likely solution is the same as the most probable solution $\mathbf{s}_{MP}$, that is the one that maximizes the *posterior* probability. This solution changes with a prior assumption on the data, such as the request of a regularization $\mathbf{g}$ like the one discussed in the previous Section. In this case, a *prior* is assumed, regularizing the parameters s_i so that also the terms $\mathbf{f}s_i$ are regularized. This is expressed in this way

$$P(\mathbf{s}|\mathbf{g},\lambda) = \frac{\exp[-\lambda E_S(\mathbf{s}|\mathbf{g})]}{Z_S(\lambda)}, \tag{2.35}$$

Z_S is the normalization, λ the regularization term, E_S the regularization function

$$\lambda E_S = \frac{1}{2}\mathbf{s}^T\mathbf{Hs} \tag{2.36}$$

with $E_S(0) = 0, H = (\lambda\mathbf{C})^{-1}$ and $\mathbf{C} = \nabla\nabla E_S$, the Hessian of E_S. Combining Eq. (2.36) and Eq. (2.34)

$$M(s) = E_D(\mathbf{s}) + \lambda E_S(\mathbf{s}) = \frac{1}{2}(\mathbf{fs}-\mathbf{d})^T\mathbf{C}_D^{-1}(\mathbf{fs}-\mathbf{d}) + \frac{1}{2}\mathbf{s}^T\mathbf{H}^{-1}\mathbf{s} \tag{2.37}$$

is defined.

By applying Bayes' theorem, I can obtain the *posterior* probability, that is the

probability of obtaining the parameters s_i once known the d_j data and the prior probability distribution:

$$P(\mathbf{s}|\mathbf{d},\lambda,\mathbf{f},\mathbf{g}) = \frac{P(\mathbf{d}|\mathbf{s},\mathbf{f})P(\mathbf{s}|\mathbf{g},\lambda)}{P(\mathbf{d}|\lambda,\mathbf{f},\mathbf{g})} = \frac{\exp[-M(\mathbf{s})]}{Z_M(\lambda)} \tag{2.38}$$

$M(\mathbf{s})$ is defined from the likelihood and the prior, while Z_M is the posterior normalization. The denominator $P(\mathbf{d}|\lambda,\mathbf{f},\mathbf{g})$ is the *evidence*, that is a probability distribution that, in strong lensing, depends on the model parameters, and is fundamental in obtaining the best regularization term λ while classifying the different lens models.

Since both likelihood and prior are assumed as gaussian probability distribution, also the posterior will be a gaussian. The most probable solution will be the one that maximizes Eq. (2.38), or minimizes Eq. (2.37), so $\nabla M(\mathbf{s}_{MP}) = 0$.

The most likely and the most probable solution

It is possible to obtain a simple expression that also connects both solutions.

As for the former, the Hessian of E_D as $\mathbf{F} = \nabla\nabla E_D(\mathbf{s}) = \mathbf{f}^T\mathbf{C}_D^{-1}\mathbf{f}$ and the quantity $\mathbf{D} = \mathbf{f}^T\mathbf{C}_D^{-1}\mathbf{d}$ are defined. These two, along with $\mathbf{s}_{ML}$: $\nabla E_D(\mathbf{s}_{ML}) = 0$, lead to

$$\mathbf{s}_{ML} = \mathbf{F}^{-1}\mathbf{D}. \tag{2.39}$$

As for the latter

$$\begin{aligned} \mathbf{s}_{MP} &= \mathbf{A}^{-1}\mathbf{f}^T\mathbf{C}_D^{-1}\mathbf{d} \\ &= \mathbf{A}^{-1}\mathbf{F}\mathbf{F}^{-1}\mathbf{f}^T\mathbf{C}_D^{-1}\mathbf{d} \\ &= \mathbf{A}^{-1}\mathbf{F}\mathbf{F}^{-1}\mathbf{D}. \end{aligned} \tag{2.40}$$

Once known (2.39), that becomes

$$\mathbf{s}_{MP} = \mathbf{A}^{-1}\mathbf{F}\mathbf{s}_{ML} = \mathbf{D}, \tag{2.41}$$

once we have calculated $\mathbf{A}$ and $\mathbf{Fs}_{ML}$.

Obtaining λ and classifying the models

In order to obtain the lens model parameters while evaluating the optimal regularization term, it is necessary to work on the evidence term. By applying again Bayes' theorem, this is expressed as

$$P(\lambda|\mathbf{d},\mathbf{f},\mathbf{g}) = \frac{P(\mathbf{d}|\lambda,\mathbf{f},\mathbf{g})P(\lambda)}{P(\mathbf{d}|\mathbf{f},\mathbf{g})}. \tag{2.42}$$

Substituting Eqs. (2.33) - (2.35) - (2.38) into Eq. (2.42) I obtain

$$P(\lambda|\mathbf{d},\mathbf{f},\mathbf{g}) = \frac{Z_M(\lambda)}{Z_D Z_S(\lambda)}. \tag{2.43}$$

The normalizations are expressed as follows

$$\begin{aligned} Z_S(\lambda) &= e^{-\lambda E_S(0)}(2\pi/\lambda)^{N_S/2}(\det \mathbf{C})^{(-1/2)} && (2.44)\\ Z_M(\lambda) &= e^{-M(s_{PP})}(2\pi)^{N_S/2}(\det \mathbf{A})^{(-1/2)} && (2.45)\\ Z_D &= (2\pi)^{N_d/2}(\det \mathbf{C}_D)^{(1/2)} && (2.46) \end{aligned}$$

In principle, the order of magnitude of these quantities is unknown, so it is better use the logarithm of the evidence, $\log P(\lambda|\mathbf{d},\mathbf{f},\mathbf{g})$. This does not affect the Bayesian analysis.

$$\begin{aligned} \log P(\lambda|\mathbf{d},\mathbf{f},\mathbf{g}) = \quad & +\lambda E_S(0) - \lambda E_S(s_{PP}) - E_D(s_{PP}) \\ & -\frac{1}{2}\log(\det \mathbf{A}) + \frac{N_s}{2}\log\lambda + \frac{1}{2}\log(\det \mathbf{C}) \\ & -\frac{N_d}{2}\log(2\pi) + \frac{1}{2}\log(\det \mathbf{C}_D^{-1}) \end{aligned} \tag{2.47}$$

The best estimate of the regularization term $\hat{\lambda}$ is obtained by setting the derivative of this expression to zero:

$$2\hat{\lambda}E_S(s_{PP}) = N_s - \hat{\lambda}\mathrm{Tr}(\mathbf{A}^{-1}\mathbf{C}) \tag{2.48}$$

This expression is often non-linear, and its resolution needs the use of numerical methods.

In the SLI formalism, calling the evidence ε, Eq. (2.47) is expressed as follows:

$$\begin{aligned} 2\ln\left[\varepsilon(\lambda)\right] &= -G_\lambda(\mathbf{S}) - \ln[\det(\mathbf{F}+\lambda\mathbf{H})] \\ &\quad - \ln[\det(\lambda\mathbf{H})] - \sum_{j=1}^{J}\ln\left(2\pi\sigma_j^2\right). \end{aligned} \tag{2.49}$$

Here, the sum on the j terms is intended on the image pixels (or the visibilities).

The first term on the right-hand-side corresponds to the χ^2_{im}, that is dependent of λ since the reconstructed SP counts depends on its value. The fourth term is a constant associated to noise in the data.

Once lens mass parameters are fixed, $\hat{\lambda}$ is the one that maximizes the evidence (or its logarithm), while the best-fit parameters for the lens will be the ones for which the overall evidence in Eq. (2.49) in the parameter space is maximum. Let's show this.

In order to compare different models **f** with different regularizations **g**, the posterior probability is analyzed, obtained from Bayes' rule as

$$P(\mathbf{f},\mathbf{g}|\mathbf{d}) \propto P(\mathbf{d}|\mathbf{f},\mathbf{g})P(\mathbf{f},\mathbf{g}). \tag{2.50}$$

In order to classify the different models, it is mandatory that the prior $P(\mathbf{f},\mathbf{g})$ is a flat distribution. By recalling the evidence $P(\mathbf{d}|\mathbf{f},\mathbf{g},\lambda)$ from Eq. (2.47), it is possible to rewrite the posterior:

$$P(\mathbf{d}|\mathbf{f},\mathbf{g}) = \int P(\mathbf{d}|\mathbf{f},\mathbf{g},\lambda)P(\lambda)d\lambda, \tag{2.51}$$

such that λ becomes a marginalized parameter.

The corresponding probability distribution for λ is assumed as approximated with a Dirac delta δ_D centered in $\hat{\lambda}$. δ_D acts inside an integral selecting the value in which it is centered, and as a consequence, the necessary term to rank the different models, that is $P(\mathbf{d}|\mathbf{f}, \mathbf{g})$, is approximated with $P(\mathbf{d}|\mathbf{f}, \mathbf{g}, \lambda_{\rm ott})$, explicited in Eqs. (2.47 - 2.49). This approximation is valid as long as the Hessian of the regularization term $E_{\rm reg}$ is non-singular, otherwise it is impossible to compare different models.

To summarize, the Bayesian inference translates the information inside $\chi^2_{\rm im}$ and the regularization in a global term, the evidence, that ranks the different solutions. The value of the regularization constant is found by maximizing the Bayesian evidence in Eq. 2.49. The parameters that best describe the mass distribution of the lens are obtained by exploring the lens parameter space and computing each time the evidence in Eq. (2.49) marginalized over λ, i.e. $\varepsilon = \int \varepsilon(\lambda) P(\lambda) d\lambda$, where $P(\lambda)$ is the probability distribution of the values of the regularization constant for a given lens model. The best-fitting values of the lens model parameters are those that maximizes ε, by approximating $P(\lambda)$ with a delta function centered around the value $\tilde{\lambda}$ that maximizes Eq. (2.42), so that $\varepsilon \simeq \varepsilon(\tilde{\lambda})$.

3

The H-ATLAS sample observed with SMA

The samples of strongly lensed galaxies generated by wide-area extragalactic surveys performed at sub-millimetre (sub-mm) to millimetre (mm) wavelengths (Negrello et al., 2010, 2017, Wardlow et al., 2013, Vieira et al., 2013, Planck Collaboration et al., 2015, Nayyeri et al., 2016), with the *Herschel* Space Observatory (Pilbratt et al., 2010), the South Pole Telescope (Carlstrom et al., 2011) and the *Planck* satellite (Cañameras et al., 2015) provide a unique opportunity to study and understand the physical properties of the most violently star forming galaxies at redshifts $z > 1$ (often cited as Dusty Star-Forming Galaxies, DSFGs from now on). In fact, the magnification induced by gravitational lensing makes these objects bright and, therefore, excellent targets for spectroscopic follow-up observations aimed at probing the physical

conditions of the interstellar medium in the distant Universe (e.g. Valtchanov et al., 2011, Lupu et al., 2012, Harris et al., 2012, Omont et al., 2011, 2013, Oteo et al., 2017a, Yang et al., 2016). At the same time, the increase in the angular sizes of the background sources due to lensing allows us to explore the structure and dynamics of distant galaxies down to sub-kpc scales (e.g. Swinbank et al., 2010, 2015, Rybak et al., 2015, Dye et al., 2015). In order to be able to fully exploit these advantages, it is crucial to reliably reconstruct the background galaxy from the observed lensed images. In Chapter 2 I illustrated how the SemiLinear Inversion method is able to model a strong lensing phenomenon. This method has been extensively implemented with numerous lensed galaxies observed with instruments such as the *Hubble* Space Telescope and the *Keck* telescope (e.g. Messias et al., 2014, Dye et al., 2015, 2008, Vegetti et al., 2012, Dye et al., 2014, Vegetti et al., 2014). For DSFGs, high resolution imaging data usable for lens modelling can mainly be achieved by interferometers at the sub-mm/mm wavelengths where these sources are bright, with the great advantage that, since the lensing galaxy is usually a massive elliptical, there is virtually no contamination from far-IR or sub-mm emission from the lens at those wavelengths.

Here, I model Sub-Milimeter Array (SMA) observations of a sample of 12 lensed galaxies discovered in the *Herschel* Astrophysical Terahertz Large Area Survey (*H*-ATLAS Eales et al., 2010a) with the adaptive source pixel scale method extended in the Fourier space described previously. Eleven of these sources were already modelled by Bussmann et al. (2013) (B13 hereafter) assuming a Sérsic profile for the light distribution of the background galaxy. I reassess their findings with this new approach, and also present SMA follow-up observations of 7 more candidate lensed galaxies from the *H*-ATLAS (Negrello et al., 2017), although I attempted lens modelling for only one of them, where multiple images can be resolved in the data.

This Chapter is based on the work published in Enia et al. (2018).

3.1 The Herschel-ATLAS

As pointed out in the first Chapter of this Thesis, in the past decades several methods to identify candidate lensed galaxies in surveys at different wavelengths have been developed and exploited. This Chapter is based on a work performed on lensed galaxies found in the Herschel Astrophysical Terahertz Large Area Survey (H-ATLAS) survey.

H-ATLAS is a Herschel Space Telescope survey that imaged approximately 600 deg^2 of sky in five bands (100, 160, 250, 350 and 500 μm) with the instruments PACS (Poglitsch et al., 2010) and SPIRE (Griffin et al., 2010), distributed in five fields, three on the celestial equator and two larger fields near the North Galactic Pole (NGP) and South Galactic Pole (SGP). The fields were chosen to minimize dust emission from the Galaxy, and to overlap with other existing surveys, i.e. the Galaxy and Mass Assembly (GAMA survey), the Sloan Digital Sky Survey (SDSS), the 2-Degree-Field Galaxy Redshift Survey (2DFGRS), the Kilo-Degree Survey (KiDS).

As outlined in the Introduction, the number counts of DSFGs reveal a steep drop at flux densities higher than 100 mJy at 500 μm. This feature is expected by different galaxy evolutionary models (Negrello et al., 2007, 2010, Blain, 1996, Perrotta et al., 2002, 2003, Lapi et al., 2006, 2011). Theoretically, every source with flux higher than this limit is either a local contaminant, a blazar, a Hyper-Luminous InfraRed Galaxy (HyLIRG) or a common DSFG whose flux has been boosted by gravitational lensing.

The survey selected 325 sources with fluxes $F_{500} > 100$ mJy, shortened to 83 when removed all the known contaminants by cross-checking the existing catalogues of local galaxies (231) and blazars (11). Three of these were found to be dusty stars. The final sample comprises 80 candidate lensed galaxies. Their position within the H-ATLAS fields is shown in Fig. 3.1.1 (Negrello et al., 2017, N17 hereafter).

Of these 80 candidates, 21 have been confirmed as strongly lensed galaxies

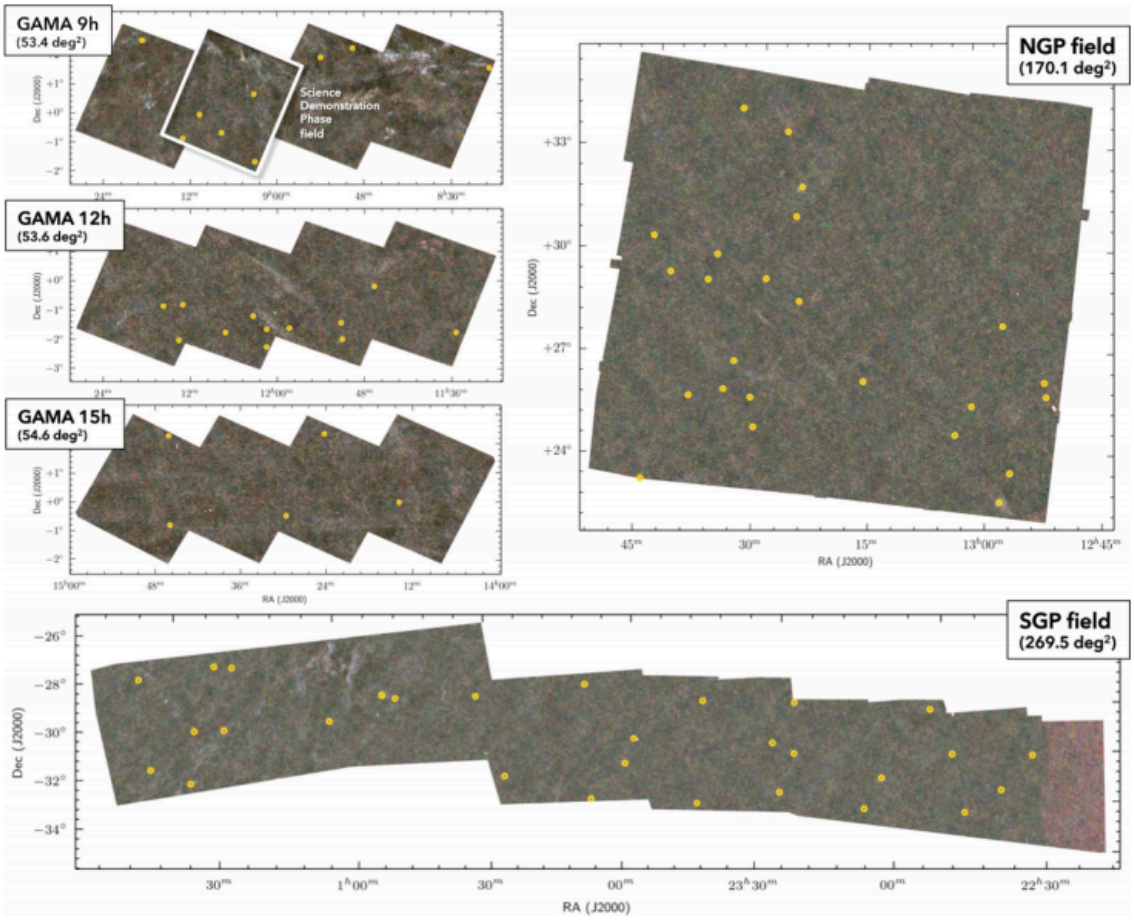

Figure 3.1.1: The five H-ATLAS field observed with SPIRE. The 80 candidate lensed galaxies are highlighted with yellow marks. (Negrello et al., 2017)

(Bussmann et al., 2013, Negrello et al., 2010, Bussmann et al., 2012, Fu et al., 2012, Messias et al., 2014, Calanog et al., 2014), ten present sources at multiple redshifts along the line of sight or have a follow-up observation hinting at the presence of multiple images (e.g. see N17, or Enia et al., 2018), while one object has been confirmed to be not strongly lensed (a binary system of HyLIRG at z = 2.410 indeed, Ivison et al., 2013). The median redshift distribution of the sources is 2.53; similar values are obtained by considering spectroscopic (2.49) and photometric (2.54) redshifts alone.

A striking visual example of the flux selection technique is shown in Fig. 3.1.2. Here, the combined sample of the whole five H-ATLAS fields integral number counts is reported, compared with the one at $F_{500} > 100$ mJy coming from HeLMS+HerS Nayyeri et al. (2016). It is immediately clear that the counts tail at $F_{500\mu m} > 100$ mJy is strongly affected by the presence of strongly lensed DSFGs, along with contaminants such as dust emission coming from spiral galaxies disks, or local starburst at $z < 0.1$, or AGN flat-spectrum synchrotron emission at high-z. Once removed by cross-matching with radio and optical catalogues, the remaining sources generally lie into two categories: strongly-lensed galaxies, or HYLIRGs, the latter being very rare.

3.2 The sample and previous results

The starting point of this Chapter is the subsample of 21 confirmed lensed galaxies, from which I kept only the sources with available SMA 870 μm continuum follow-up observations. This observations are presented in B13 (but see also Negrello et al., 2010, Bussmann et al., 2012). The observations were obtained as part of a large proposal carried out over several semesters using different array configurations from compact (COM) to very-extended (VEX), reaching a spatial resolution of $\sim 0.5''$, with a typical integration time of one to two hours on-source, per configuration. We refer the reader to B13 for details concerning the observations and data reduction.

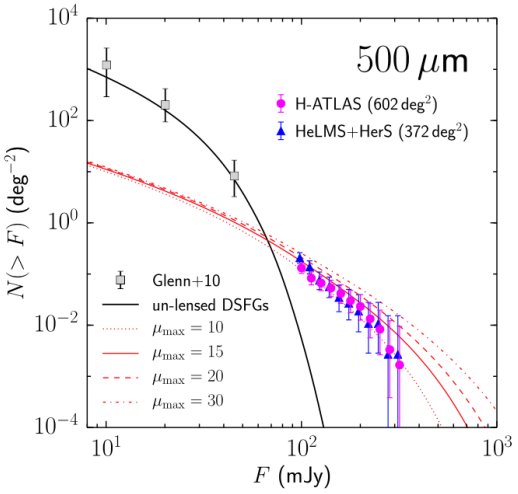

Figure 3.1.2: Integral number counts of every candidate lensed galaxy identified in the five H-ATLAS field (purple dots), compared with the results from HeLMS+HerS (Nayyeri et al., 2016, blue triangles). The predicted number counts are the solid black line, while red curves shows the predicted counts of lensed galaxies for values ranging from 10 to 30 of maximum magnification $\mu_{\max}$ (Negrello et al., 2017).

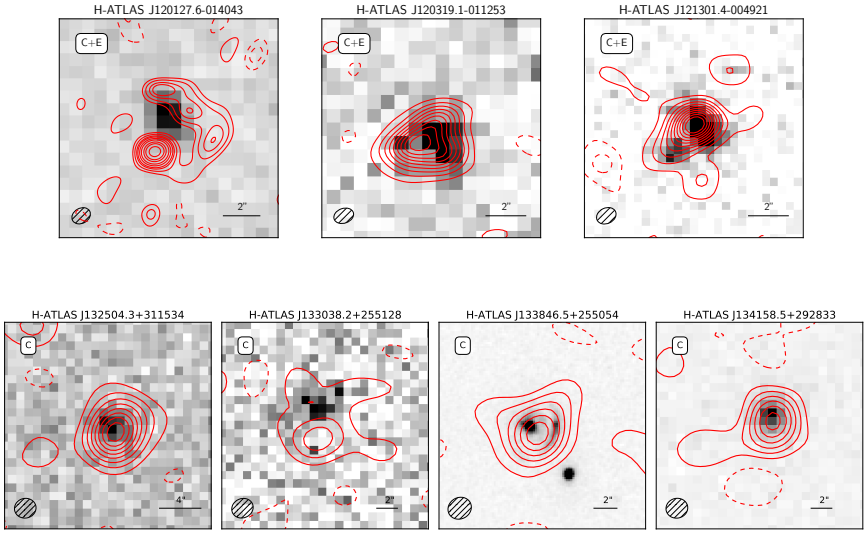

Figure 3.2.1: SMA 870 μm follow-up observations (red contours, starting at $\pm 2\sigma$ and increasing by factors of two) of seven H-ATLAS candidate lensed galaxies from the N17 sample. The three sources in the top panels were observed in both compact and extended array configurations, while the four sources in the bottom panels only have data obtained in compact configuration. The SMA's synthesized beam is shown in the lower left corner of each panel. The background images, in greyscale, show the best available optical/near-IR data and come from the Kilo Degree Survey (KiDS; de Jong et al., 2015, r band at $0.62\,\mu$m for HATLASJ120127.6−014043 and HATLASJ121301.4−004921), the VISTA Kilo-Degree Infrared Galaxy Survey (VIKING; Edge et al., 2013, K_s band at $2.2\,\mu$m for HATLAS120319.1−011253), the UK Infrared Deep Sky Survey Large Area Survey (UKIDSS-LAS; Lawrence et al., 2007, K_s band at $2.2\,\mu$m for HATLASJ132504.3+311534 and HATLASJ133038.2+255128; Y band at $1.03\,\mu$m for HATLASJ134158.5+292833) and the *HST* Wide Field Camera 3 (WFC3) at $1.6\,\mu$m (for HATLASJ133846.5+255054).

Between December 2016 and March 2017 our group carried out new SMA continuum observations at 870 μm of a further seven candidate lensed galaxies from the N17 sample (proposal ID: 2016B-S003 PI: Negrello, see Enia et al. (2018)). Not all of the observations were executed, thus while all seven sources were observed in COM configuration, only for three did we also obtain data in the extended (EXT) configuration. There is evidence of extended structure in several of our new targets, however only in HATLASJ120127.6-014043, which benefits from EXT data, the typical multiple images of a lensing event are clearly detected and resolved.

Starting from the B13 sample, I excluded three cluster scale lenses for which the lens modelling is complicated by the need for three or more mass models for the foreground objects (HATLASJ114637.9-001132, HATLASJ141351.9-000026, HATLASJ132427.0+284449). I also removed those sources where the multiple images are not fully resolved by the SMA and therefore are not usable for source reconstruction, i.e. HATLASJ090302.9-014127, HATLASJ091304.9-005344, HATLASJ091840.8+023048, HATLASJ113526.2-014606, HATLASJ144556.1-004853, HATLASJ132859.2+292326. Finally I have not considered in my analysis HATLASJ090311.6+003907, also known as SDP.81, which has been extensively modelled using high resolution data from the Atacama Large Millimetre Array (ALMA Partnership et al., 2015, Swinbank et al., 2015, Rybak et al., 2015, Dye et al., 2015, Hatsukade et al., 2015, Tamura et al., 2015, Hezaveh et al., 2016). Finally, I have added HATLASJ120127.6-014043 to this sample, the source for which our group obtained new SMA data. Therefore, my final sample comprises 12 objects, which are included in Table 3.2.1.

The measured 870 μm flux density for each source is reported in Table 3.2.1. It was computed by adding up the signal inside a customized aperture that encompasses the source emission. The quoted uncertainties correspond to the root-mean-square variation of the primary-beam corrected signal measured within the same aperture in 100 random positions inside the region defined by

Table 3.2.1: List of *H*-ATLAS lensed galaxies with SMA imaging data selected for the lens modelling and source reconstruction. Most are taken from B13, excluding group/cluster scale lenses and sources which are not clearly resolved into multiple images by the SMA. The list also includes candidate lensed galaxies from N17 for which we have obtained new SMA observations. However only one of them is clearly resolved into multiple images because of the limited resolution achieved and therefore only this object, HATLAS J120127.6-014043, is considered for the lens modelling. Reading from left to right, columns following the identifier are: redshifts of the lens and of the background galaxy (from N17; when no spectroscopic redshift is available the photometric one is provided instead, in italic style), SPIRE/*Herschel* flux densities at 250, 350 and 500μm (from N17), flux density from the SMA, array configuration of the observations performed with the SMA (SUB=sub-compact, COM=compact, EXT=extended, VEX=very extended).

H-ATLAS IAU Name	$z_{\rm opt}$	$z_{\rm sub-mm}$	F_{250} (mJy)	F_{350} (mJy)	F_{500} (mJy)	$F_{\rm SMA}$ (mJy)	SMA Array Configuration
SMA data from Bussmann et al. (2013)							
HATLASJ083051.0+013225	0.6261+1.0002	3.634	248.5±7.5	305.3±8.1	269.1±8.7	76.6±2.0	COM+EXT
HATLASJ085358.9+015537	-	2.0925	396.4±7.6	367.9±8.2	228.2±8.9	50.6±2.6	COM+EXT+VEX
HATLASJ090740.0-004200	0.6129	1.577	477.6±7.3	327.9±8.2	170.6±8.5	20.3±1.8	COM+EXT
HATLASJ091043.0-000322	0.793	1.786	420.8±6.5	370.5±7.4	221.4±7.8	24.4±1.8	COM+EXT+VEX
HATLASJ125135.3+261457	-	3.675	157.9±7.5	202.3±8.2	206.8±8.5	64.5±3.4	COM+EXT
HATLASJ125632.4+233627	0.2551	3.565	209.3±7.3	288.5±8.2	264.0±8.5	85.5±5.6	COM+EXT
HATLASJ132630.1+334410	0.7856	2.951	190.6±7.3	281.4±8.2	278.5±9.0	48.3±2.1	EXT
HATLASJ133008.4+245900	0.4276	3.1112	271.2±7.2	278.2±8.1	203.5±8.5	49.5±3.4	COM+EXT
HATLASJ133649.9+291800	-	2.2024	294.1±6.7	286.0±7.6	194.1±8.2	37.6±6.6	SUB+EXT+VEX
HATLASJ134429.4+303034	0.6721	2.3010	462.0±7.4	465.7±8.6	343.3±8.7	55.4±2.9	COM+EXT+VEX
HATLASJ142413.9+022303	0.595	4.243	112.2±7.3	182.2±8.2	193.3±8.5	101.6±7.4	COM+EXT+VEX
New SMA observations							
HATLASJ120127.6-014043	-	*3.80±0.58*	67.4±6.5	112.1±7.4	103.9±7.7	52.4±3.2	COM+EXT
HATLASJ120319.1-011253	-	*2.70±0.44*	114.3±7.4	142.8±8.2	110.2±8.6	40.4±2.4	COM+EXT
HATLASJ121301.5-004922	*0.191±0.080*	*2.35±0.40*	136.6±6.6	142.6±7.4	110.9±7.7	23.4±1.7	COM+EXT
HATLASJ132504.3+311534	*0.58±0.11*	*2.03±0.36*	240.7±7.2	226.7±8.2	164.9±8.8	35.2±2.2	COM
HATLASJ133038.2+255128	*0.20±0.15*	*1.82±0.34*	175.8±7.4	160.3±8.3	104.2±8.8	19.1±1.9	COM
HATLASJ133846.5+255054	*0.42±0.10*	*2.49±0.42*	159.0±7.4	183.1±8.2	137.6±9.0	27.4±2.5	COM
HATLASJ134158.5+292833	*0.217±0.015*	*1.95±0.35*	174.4±6.7	172.3±7.7	109.2±8.1	20.9±1.5	COM

the primary beam of the instrument. As explained in Chapter 2, our lens modelling and source reconstruction are performed on interefometric data by adopting a natural weighting scheme. The SMA *dirty* images obtained with this scheme are shown in the left panels of Fig. 3.4.1.

B13 modelled the SMA observed galaxies with a fully parametric model applied on the *uv*-plane. The lenses were assumed to be Singular Isothermal Ellipsoids (SIE; Kormann et al., 1994), the sources single or multiple Sérsic profiles. In his method, the sources are lensed into a model image plane using the publicly available software *GRAVLENS*, then analyzed with the software *MIRIAD* in order to obtain the set of visibilities that generate that observation. The χ^2 minimization is performed between the real and imaginary part of this model visibilities and the observed ones. The best-fit parameters are the one that minimize the statistic.

The B13 sources probe a wide range in luminosity ($\log L_{FIR}$ from 12.45 to 13.18) and size (half-light radii spanning from 0.40 kpc to 4.14 kpc, median $r_{half} = 1.6$ kpc). Three sources possess a surface star formation rate Σ_{SFR} above the theoretical limit of 1000 $M_\odot yr^{-1} kpc^{-2}$ for an Eddington powered optically thick disk, with a median value of approximately 200 $M_\odot yr^{-1} kpc^{-2}$.

3.3 Implementation Notes

In order to compare my findings with the results presented in B13, I model the mass distribution of the lenses as a SIE, i.e. assuming a density profile of the form $\rho \propto r^{-2}$, r being the elliptical radius. The choice of a SIE over a more generic power-law profile, $\rho \propto r^{-a}$, is also motivated by the results of the modelling of other lensing systems from literature (e.g. Dye et al., 2015, 2014, Barnabè et al., 2009, Dye et al., 2017), which show that $a \sim 2$, and by the need of keeping to a minimum the number of free parameters. In fact, the resolution of the SMA data analyzed here is a factor $\times 3 - 4$ worse than the one provided by the optical and near-infrared imaging data - mainly from the Hubble space telescope - used in the aforementioned literature.

However it is important to point out that a degeneracy between different lens model profiles can lead to biased estimates of the source size and magnification. In fact, as first discussed by Falco et al. (1985), a particular rescaling of the density profile of the lens, together with an isotropic scaling of the source plane coordinates, produces exactly the same observed image positions and flux ratios (but different time delays). This is known as the mass-sheet transformation (MST) and represents a special case of the more general source-position transformation described by Schneider and Sluse (2014). Schneider and Sluse (2013) showed that the MST is formally broken by assuming a power-law model for the mass distribution of the lens, although there is no physical reason why the true lens profile should have such an analytic form. Furthermore, the power-law model is also affected by the $\sigma - q - a$ degeneracy between the lens mass (expressed in terms of the 1D velocity dispersion σ), the axis ratio (q) and the slope (a). In fact, as discussed in Nightingale and Dye (2015), different combinations of these three parameters produce identical solutions in the image plane, but geometrically scaled solutions in the source plane, thus affecting the measurement of the source size and magnification. However, the same author also showed that the use of a randomly initialized adaptive grid (the same adopted in this work), with a fixed number of degree-of-freedom, removes the biases associated with this degeneracy. We will test our assumption of a SIE profile in a future work using available HST and ALMA data, by comparing the lens modelling results obtained for $a = 2$ with those derived for a generic power-law model.

The SIE profile is described by 5 parameters: the displacement of the lens centroid, $\Delta x_{\rm L}$ and $\Delta y_{\rm L}$, with respect to the centre of the image, the Einstein radius, $\theta_{\rm E}$, the minor-to-major axis ratio, $q_{\rm L}$, the orientation of the semi-major axis, $\theta_{\rm L}$, measured counter-clockwise from West. In order to reduce the number of free parameters, we do not include an external shear, unless it is needed to improve the modelling, i.e. it is suggested by bad retrieved source reconstruction, or if it is known from near-IR observations that the lens is near a field that causes a non-negligible source of exernal shear. In fact, this only happens for of

HATLAS J091043.1-000321. Here, the shear effect is described by two additional parameters: the shear strength, γ, and the shear angle, θ_γ, also measured counter-clockwise from West, thus raising the total number of free parameters from 5 to 7.

The lens parameter space is explored using MULTINEST (Feroz and Hobson, 2008, Feroz et al., 2009), a Monte Carlo technique implementing the nested sampling described in Skilling (2006). Flat priors are adopted for the lens model, within the range:

0.1 arcsec $\leq \theta_\mathrm{E} \leq 3.0$ arcsec;

$0° \leq \theta_\mathrm{L} < 180°$;

$0.2 \leq q_\mathrm{L} < 1.0$;

-0.5 arcsec $\leq \Delta x_\mathrm{L} \leq 0.5$ arcsec; -0.5 arcsec $\leq \Delta y_\mathrm{L} \leq 0.5$ arcsec;

$0.0 \leq \gamma \leq 0.3$; $0° \leq \theta_\gamma < 180°$ if a source of external shear is present.

In order to lighten the computational effort, a mask is applied to the IP pixels, keeping only those relevant, i.e. containing the lensed image, with minimum background sky. These are then traced back to the SP where they define the area used for the source reconstruction.

As suggested in Nightingale and Dye (2015), a nuisance in lens modeling algorithms is the existence of unrealistic solutions, occupying significant regions of the parameter space where the Monte Carlo method gets stuck. In general these local minima of the evidence correspond to a reconstructed SP that resembles a demagnified version of the observed IP. In order to avoid them, the first search of the parameter space is performed on a selected grid of values of the free parameters, following the methods presented in Nightingale and Dye (2015). Then, the regions occupied by unrealistic solutions are excluded from the subsequent search. Once the best lens model parameters are identified, a final MULTINEST run is employed to sample the posterior distribution function (PDF), and to estimate the corresponding uncertainties, which are quoted as the 16th and 84th percentile of the PDF.

In previous work (i.e. Hezaveh et al., 2013) it is assumed that the observed visibilities suffer from antenna-based phase errors. These errors are dealed by

modelling the self-calibration extra parameters alongside the other lensing parameters. However, in this sample, all the antenna phase errors are already removed by self-calibration.

A fundamental quantity provided by the lens modelling is the magnification factor, μ. This is defined as the ratio between the total flux density of the source, as measured in the SP, and the total flux density of the corresponding images in the IP. In practice I estimate it as $\mu = F^{\rm IP}_{N\sigma}/F^{\rm SP}_{N\sigma}$ where $F^{\rm SP}_{N\sigma}$ is the flux density contributed by all the pixels in the SP with signal-to-noise ratio SNR $\geq N$, while $F^{\rm IP}_{N\sigma}$ is the summed flux density of the all pixels within the corresponding region in the IP. I compute the value of μ for $N = 3$ and $N = 5$, taking the latter as our reference case. The uncertainty on the magnification factor is derived by calculating μ 1000 times, each time perturbing the lens model parameters around their best-fitting values; the final magnification factor is the median of the resulting distribution with errors given by the 16th and 84th percentile of the same distribution.

3.4 Results and discussion

The best-fitting values of the lens model parameters are reported in Table 3.4.1, while the results of the source reconstruction are shown in Fig. 3.4.1. The first panel on the left is the SMA dirty image, generated by adopting a natural weighting scheme. The second and the third panels from the left show the reconstructed IP and the residuals, respectively. The latter are derived by subtracting the model visibilities from the observed ones and then imaging the differences. The panel on the right shows the reconstructed source with contours at 3σ (black curve) and 5σ (white curves), while the second panel from the right shows the image obtained by assuming the best-fitting lens model and performing the gravitational lensing directly on the reconstructed source. The lensed image obtained in this way is unaffected by the sampling of the uv plane and can thus help to recognize in the SMA dirty image those features that are

Table 3.4.1: Results of the modelling for the lens mass distribution, for which a SIE profile is assumed. The parameters of the model are: the normalization of the profile, expressed in terms of the Einstein radius ($\theta_{\rm E}$); the rotation angle ($\theta_{\rm L}$; measured counter-clockwise from West); the minor-to-major axis ratio ($q_{\rm L}$); the position of the lens centroid from the centre of the images in Fig. 3.4.1; the shear strength (γ) and the shear angle (θ_γ; counter-clockwise from West).

IAUname	$\theta_{\rm E}$ (arcsec)	$\theta_{\rm L}$ ($^\circ$)	$q_{\rm L}$	$\Delta x_{\rm L}$ (arcsec)	$\Delta y_{\rm L}$ (arcsec)	γ	θ_γ ($^\circ$)
HATLASJ083051.0+013225	0.31±0.03	38.5± 7.5	0.33±0.07	-0.49±0.04	+0.07± 0.04	-	-
	0.58±0.05	172.6±16.8	0.82±0.08	+0.18±0.03	-0.63±0.05	-	-
HATLASJ085358.9+015537	0.54±0.01	62.3±30.0	0.95±0.05	-0.22±0.03	+0.03±0.03	-	-
HATLASJ090740.0-004200	0.65±0.02	143.7± 7.0	0.75±0.07	-0.09±0.02	-0.06±0.05	-	-
HATLASJ091043.1-000321	0.91±0.03	112.9±10.2	0.62±0.09	0.00±0.07	+0.33±0.05	0.20±0.05	76.0±12.0
HATLASJ120127.6-014043	0.82±0.04	169.0±6.7	0.58±0.09	+0.06±0.06	+2.00±0.05	-	-
HATLASJ125135.4+261457	1.10±0.02	28.0±2.5	0.51±0.06	-0.23±0.05	+0.39±0.04	-	-
HATLASJ125632.7+233625	0.69±0.03	24.6±7.4	0.54±0.09	-0.05±0.10	-0.10±0.06	-	-
HATLASJ132630.1+334410	1.76±0.05	149.4±9.0	0.62±0.08	-0.49±0.10	+0.67±0.10	-	-
HATLASJ133008.4+245900	1.03±0.02	172.1±2.2	0.51±0.03	-1.54±0.08	+0.95±0.04	-	-
HATLASJ133649.9+291801	0.41±0.02	38.5±4.3	0.53±0.12	+0.22±0.05	+0.20±0.04	-	-
HATLASJ134429.4+303036	0.96±0.01	82.7±1.5	0.53±0.07	+0.34±0.06	+0.02±0.03	-	-
HATLASJ142413.9+022303	0.98±0.02	91.0±4.9	0.79±0.04	+1.09±0.03	+0.33±0.04	-	-

really associated with the emission from the background galaxy.

The estimated magnification factors, $\mu_{3\sigma}$ and $\mu_{5\sigma}$, are listed in Table 3.4.2 for the two adopted values of the signal-to-noise ratios in the SP, i.e. SNR ≥ 3 and SNR ≥ 5, respectively. The area, $A_{\rm dust}$, of the regions in the SP used to compute the magnification factors is also listed in the same table together with the corresponding *effective radius*, $r_{\rm eff}$. The latter is defined as the radius of a circle of area equal to $A_{\rm dust}$. We note that, despite the difference in the value of the area in the two cases, the derived magnification factors are consistent with each other. In fact, as the area decreases when increasing the SNR from 3 to 5, the centre of the selected region, in general, moves away from the caustic, where the magnification is higher. The two effects tend to compensate each other, thus reducing the change in the total magnification. Below I discuss the findings with respect to the results of B13 and other results from the literature.

3.4.1 Source by source description

Fig. 3.4.2 compares my estimates of the lens mass model parameters with those of B13. In general I find good agreement, although there are some exceptions (e.g. HATLASJ133008.4+245900), particularly when multiple lenses are involved in the modelling, i.e. for HATLASJ083051.0+013225 and HATLASJ142413.9+022303. I briefly discuss each case individually.

HATLASJ083051.0+013225: This is a relatively complex system (see Fig. 1 of N17), with two foreground objects at different redshifts (B17) revealed at 1.1 μm and 2.2 μm by observations with *HST*/WFC3 (N17; Negrello et al. in prep.) and *Keck*/AO (Calanog et al., 2014), respectively. However the same data show some elongated structure north of the two lenses, which may be associated with the background galaxy, although this is still unclear due to the apparent lack of

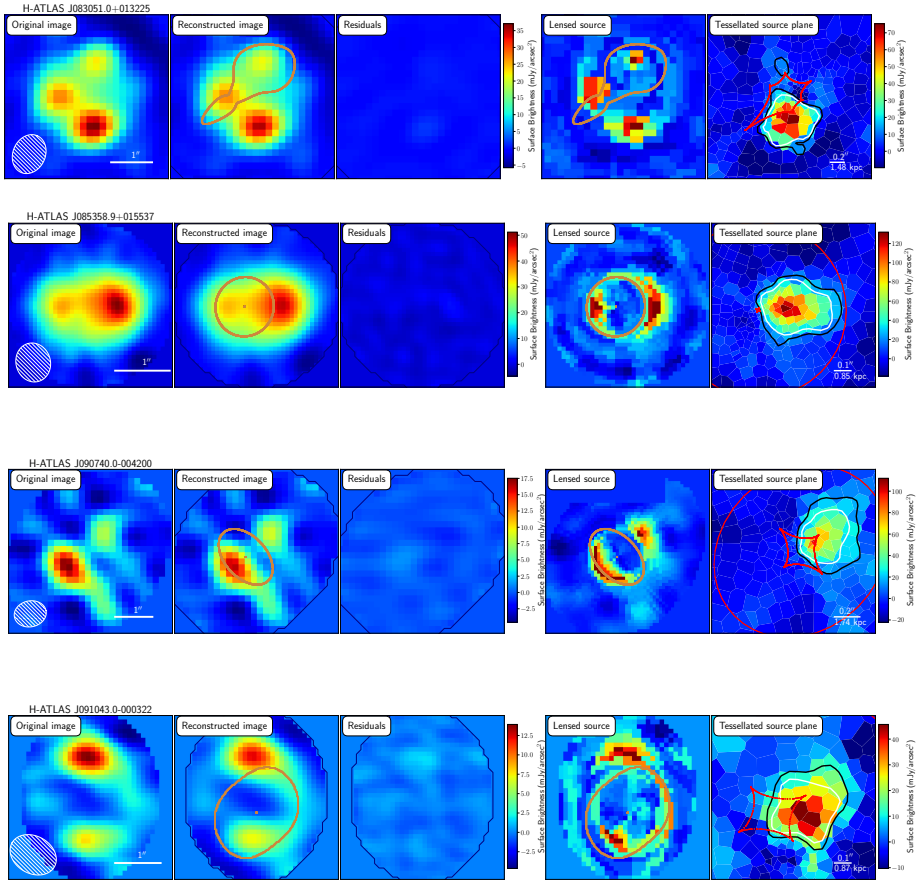

Figure 3.4.1: Results of the lens modelling and source reconstruction. From left to right: input SMA image (created using a natural weighting scheme); minimum χ^2 image; residuals obtained by first subtracting the observed visibilities with the model ones and then transforming back to the real space; image obtained by lensing the reconstructed source plane using the best-fitting lens model; the reconstructed background source with contours at 3 σ (black curve) and 5 σ (white curve). The caustics and the critical lines are shown in brown (in the second and fourth panels from left) and in red (in the right panel), respectively. The white hatched ellipse in the bottom left corner of the leftmost panels represents the SMA synthesized beam.

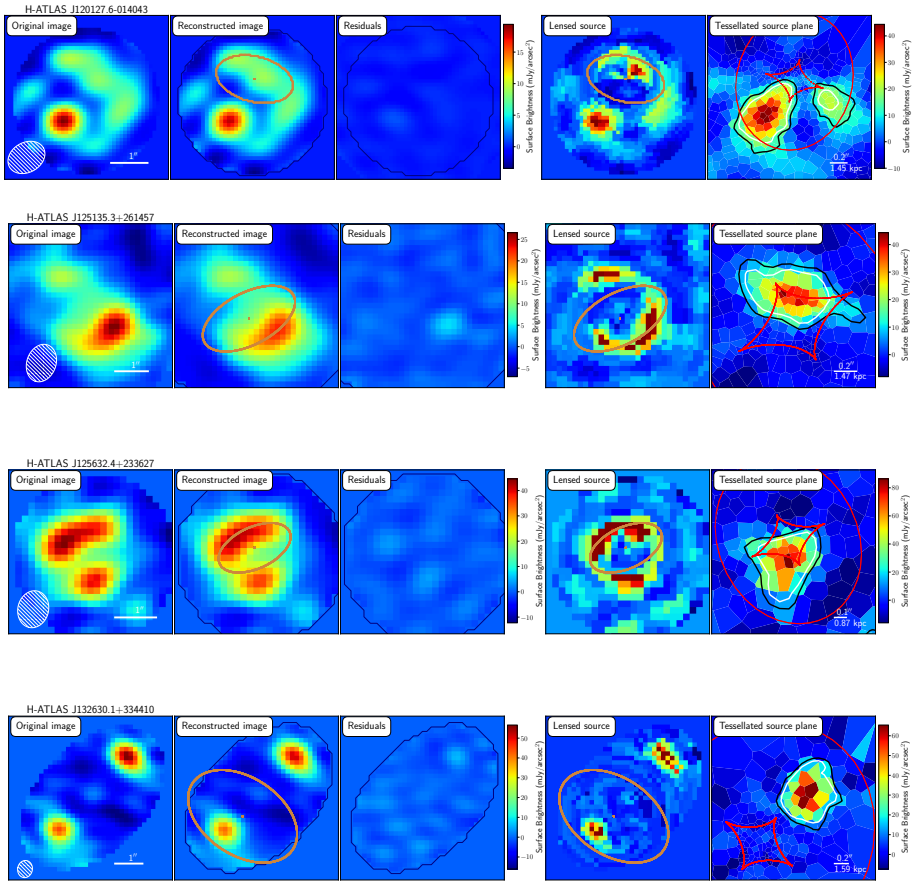

Figure 3.4.1: *- continued*

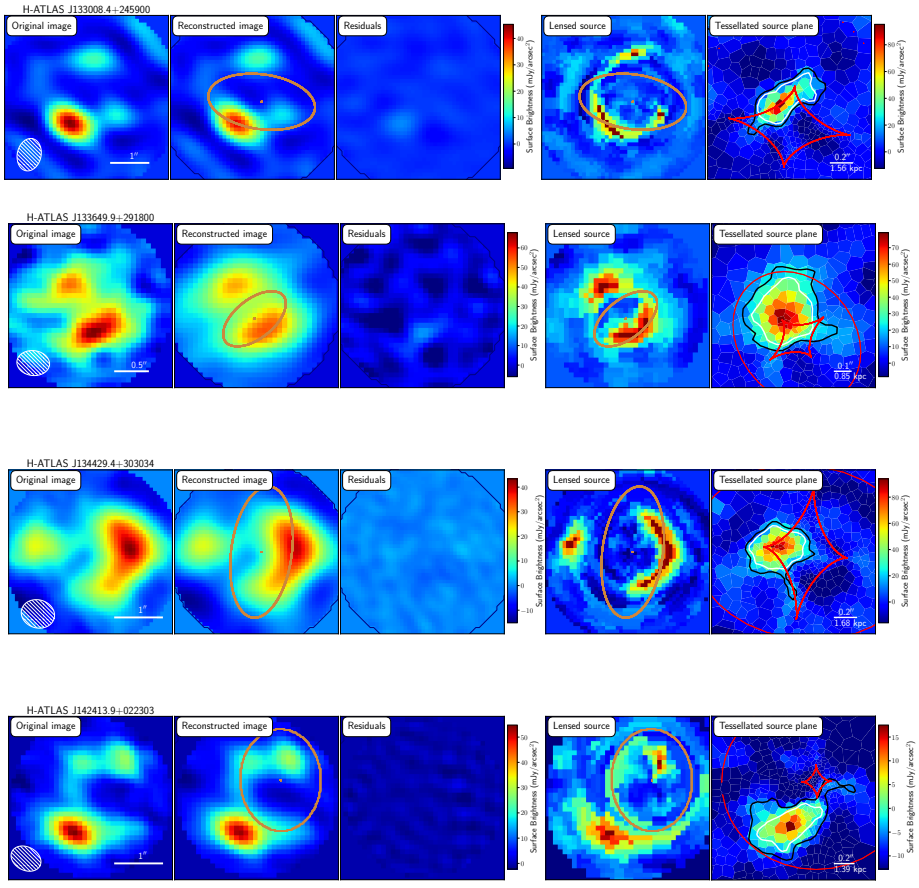

Figure 3.4.1: *- continued*

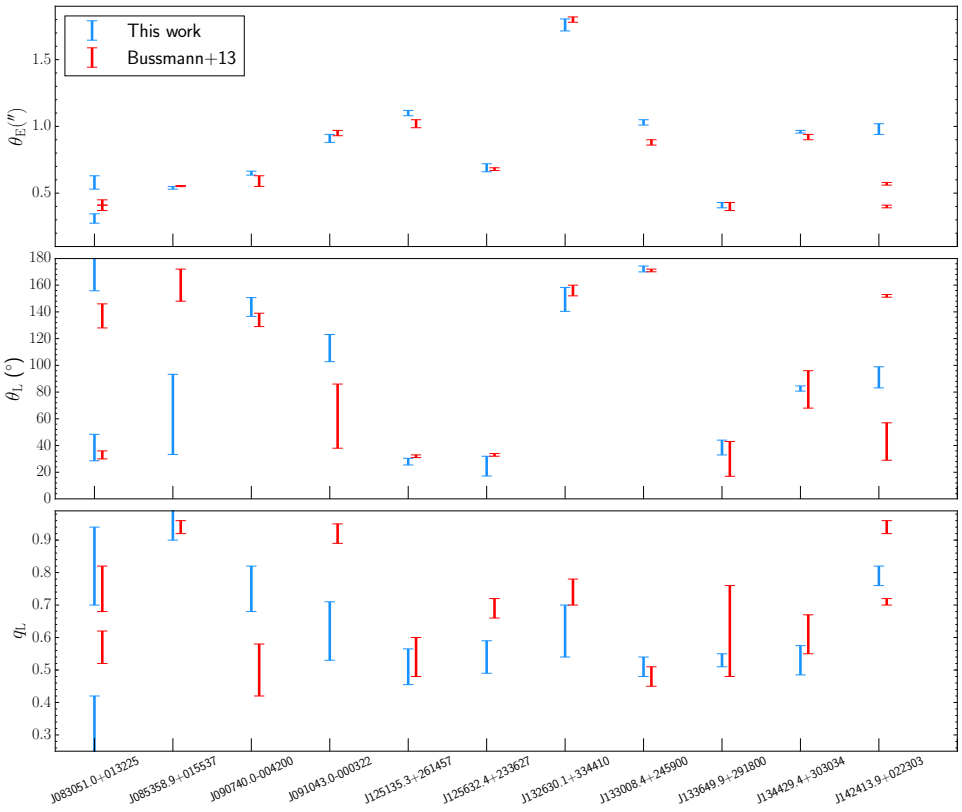

Figure 3.4.2: Comparison between my results (blue error bars) and those of B13 (red error bars) for the parameters of the SIE lens mass model: Einstein radius, θ_E, rotation angle, θ_L, and minor-to-major axis ratio, q_L. Two data-points are plotted whenever two lenses are employed in lens modeling (HATLASJ083051.0+013225, HATLASJ142413.9+022303).

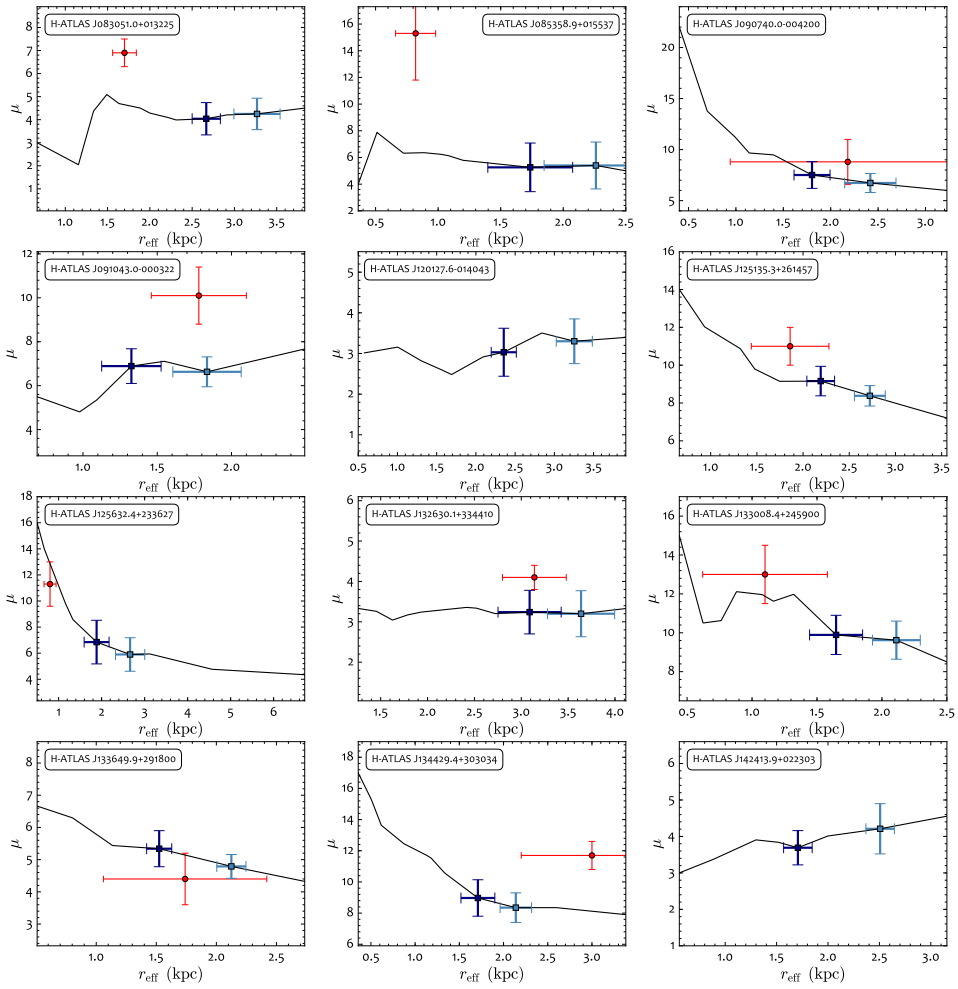

Figure 3.4.3: Magnification profiles of the reconstructed sources. The magnification factor, μ, is evaluated in steps of SNR in the SP, from two up to the maximum and shown as a function of the effective radius of the area defined by the SP pixels with SNR above the adopted steps. The squares mark the values of the magnification calculated for SNR $= 3$ (outermost; light blue square) and SNR $= 5$ (innermost; dark blue square). The red point is the magnification factor estimated by B13. I have placed it at a radius corresponding to $2 \times r_{\rm half}$, as this is the radius of the region in the SP used by B13 to compute the magnification. For HATLASJ142313.9+022303, the point of B13 is located outside the plotted region, at $r_{\rm eff} \sim 7$ kpc.

Table 3.4.2: Lens modeling results: source properties. Magnifications, $\mu_{3\sigma}$ and $\mu_{5\sigma}$, are evaluated as the ratio between the total flux density of the region in the SP with SNR≥ 3 and SNR≥ 5, respectively, and the total flux density of the corresponding region in the IP. $A_{\rm dust,3\sigma}$ and $A_{\rm dust,5\sigma}$ are the areas of the regions with SNR≥ 3 and SNR≥ 5 in the source plane, while $r_{\rm eff,3\sigma}$ and $r_{\rm eff,5\sigma}$, are the radius of a circle with area equal to $A_{\rm dust,3\sigma}$ and $A_{\rm dust,5\sigma}$, respectively. FHWMs are the values of the FWHM of the major and minor axis length obtained from the Gaussian fit to the reconstructed source surface brightness, while $\rm FWHM_m = \sqrt{FWHM_{maj} \times FWHM_{min}}$.

H-ATLAS IAU name	$\mu_{3\sigma}$	$\mu_{5\sigma}$	$A_{\rm dust,3\sigma}$ (kpc^2)	$A_{\rm dust,5\sigma}$ (kpc^2)	$r_{\rm eff,3\sigma}$ (kpc)	$r_{\rm eff,5\sigma}$ (kpc)	FWHMs (kpc)	FWHMm (kpc)
HATLASJ083051.0+013225	4.25±0.68	4.04±0.70	33.5±5.6	22.3±2.8	3.27±0.27	2.67±0.17	1.64/1.46	1.54±0.10
HATLASJ085358.9+015537	5.40±1.76	5.26±1.82	16.1±6.0	9.5±3.7	2.26±0.41	1.74±0.34	1.72/1.14	1.37±0.33
HATLASJ090740.0-004200	6.73±0.93	7.51±1.31	18.4±4.1	10.2±2.0	2.42±0.27	1.80±0.19	1.83/1.24	1.46±0.18
HATLASJ091043.1-000321	6.63±0.68	6.89±0.79	10.6±2.7	5.5±1.6	1.84±0.23	1.33±0.20	1.32/1.17	1.24±0.19
HATLASJ120127.6-014043	3.30±0.55	3.03±0.59	33.3±4.8	17.4±2.4	3.25±0.23	2.36±0.16	1.87/1.33	1.57±0.07
HATLASJ125135.4+261457	8.38±0.54	9.16±0.78	23.3±2.9	15.1±2.1	2.72±0.17	2.19±0.15	2.19/1.12	1.56±0.08
HATLASJ125632.7+233625	5.90±1.29	6.85±1.67	22.3±5.6	11.1±3.4	2.66±0.34	1.88±0.29	1.36/1.32	1.34±0.23
HATLASJ132630.1+334410	3.20±0.57	3.24±0.54	41.6±8.4	29.9±5.9	3.64±0.36	3.09±0.34	2.06/1.67	1.86±0.17
HATLASJ133008.4+245900	9.62±0.98	9.89±1.01	14.0±2.4	8.5±2.1	2.11±0.18	1.65±0.20	1.64/0.70	1.07±0.10
HATLASJ133649.9+291801	4.79±0.37	5.34±0.56	14.2±1.6	7.3±1.0	2.13±0.12	1.52±0.10	1.57/1.40	1.48±0.09
HATLASJ134429.4+303036	8.35±0.95	8.97±1.17	14.4±2.4	9.2±1.8	2.14±0.18	1.71±0.19	1.52/1.00	1.24±0.12
HATLASJ142413.9+022303	4.21±0.69	3.69±0.47	19.7±2.4	9.1±1.5	2.51±0.14	1.71±0.14	2.04/1.11	1.50±0.12

counter-images (a detailed lens modelling of this system performed on ALMA+*HST*+*Keck* data is currently ongoing; Negrello et al. in prep.). In my modelling I have assumed that the two lenses are at the same redshift, consistently with the treatment by B13. However, compared to B13, the derived Einstein radius is higher for one lens ($0.57''$ versus $0.43''$) and lower for the other ($0.31''$ versus $0.39''$). The discrepancy is likely due to the complexity of the system, which may induce degeneracies among the model parameters; however it is worth mentioning that while I keep the position of both lenses as free parameters, B13 fixed the position of the second lens with respect to the first one, by setting the separation between the two foreground objects equal to that measured in the near-IR image.

HATLASJ085358.9+015537: This system was observed with *Keck*/NIRC2 in the K_s-band (Calanog et al., 2014). The background galaxy is detected in the near-IR in the form of a ring-like structure that was modelled by Calanog et al. assuming a SIE model for the lens and a Sérsic profile for the background source

surface brightness. The modelling of the SMA data gives results for the lens mass model consistent with those of Calanog et al., both indicating an almost spherical lens. B13 also find a nearly spherical lens ($q_{\rm L} \sim 0.94$) but with a different rotation angle ($\theta_{\rm L} \sim 160^{\circ}$ versus $\theta_{\rm L} \sim 62^{\circ}$), even though the discrepancy is less than 3σ once we consider that a more spherical lens naturally possess a bigger confidence interval in $\theta_{\rm L}$ than an elliptical lens.

HATLASJ090740.0-004200: This is one of the first five lensed galaxies discovered in *H*-ATLAS (Negrello et al., 2010), and is also known as SDP.9. High-resolution observations at different wavelengths are available for this system, from the near-IR with *HST*/WFC3 (Negrello et al., 2014), to sub-mm with NOEMA (Oteo et al., 2017a) or 1.1mm with ALMA (Wong et al., 2017), to the X-ray band with Chandra (Massardi et al., 2018). The results of my lens modelling of the SMA data are consistent with those obtained by other groups at different wavelengths (e.g. Dye et al., 2014, Massardi et al., 2018, , see next Chapter). However, B13 found a significantly lower lens axis-ratio compared to our estimate ($q_{\rm L} = 0.50$ versus $q_{\rm L} = 0.75$).

HATLASJ091043.1-000321: This is SDP.11, another of the first lensed galaxies discovered in *H*-ATLAS (Negrello et al., 2010). *HST*/WFC3 imaging data at 1.1μm reveals an elongated Einstein ring (Negrello et al., 2014), hinting to the effect of an external shear possibly associated with a nearby edge-on galaxy. In fact, Dye et al. (2014) introduced an external shear in their lens modelling of this system, which they constrained to have strength $\gamma \sim 0.23$. I also account for the presence of external shear in my analysis. The results are consistent with those of Dye et al. They also agree with the Einstein radius estimated by B13, although my lens is significantly more elongated and has a higher rotation angle. It is worth noticing, though, that B13 does not introduce an external shear in their analysis, which may explain the difference in the derived lens axial ratio.

HATLASJ120127.5-014043: This is the *H*-ATLAS source confirmed to be lensed with the new SMA data. It is the only object in the sample that still lacks a spectroscopic measure of the redshift of the background galaxy. The redshift estimated from the *Herschel*/SPIRE photometry is $z_{\rm sub-mm} = 3.80 \pm 0.58$. The

reconstructed source is resolved into two knots of emission, separated by ~ 3.5 kpc.

HATLASJ125135.4+261457: The estimated Einstein radius is slightly higher than reported by B13 ($\theta_E = 1.10 \pm 0.02''$ versus $\theta_E = 1.02 \pm 0.03''$) while the rotation angle of the lens is smaller ($\theta_L = 28 \pm 2.5°$ versus $\theta_L = 38 \pm 1°$). The reconstructed source is quite elongated, extending in the SW to NE direction, with a shape that deviates from a perfect ellipse. This might suggest that, at the scale probed by the SMA observations, the source comprises two partially blended components. This morphology is not accounted for by a single elliptical Sérsic profile, which may explain the observed discrepancies with the results of B13.

HATLASJ125632.7+233625: For this system I find a lens that is more elongated compared to the value derived by B13 ($q_L = 0.54 \pm 0.09$ versus $q_L = 0.69 \pm 0.03$). The reconstructed source morphology has a triangular shape which may bias the results on the lens parameters when the modelling is performed under the assumption of a single elliptical Sérsic profile, as in B13.

HATLASJ132630.1+334410: The background galaxy is lensed into two images, separated by $\sim 3.5''$, none of them resembling an arc. This suggests that the source is not lying on top of the tangential caustic, but away from it, although still inside the radial caustic to account for the presence of two images. As revealed by *HST*/WFC3 observations (see N17, their Fig. 3), the lens is located close to the southernmost lensed image. The lack of extended structures, like arcs or rings, makes the lens modelling more prone to degeneracies. Despite that, there is a good agreement with the results of B13.

HATLASJ133008.4+245900: Besides the lens modelling performed by B13 on SMA data, this system was also analysed by Calanog et al. (2014) using *Keck*/AO K_s-band observations, where the background galaxy is detected. The configuration of the multiple images is similar in the near-IR and in the sub-mm suggesting that the stellar and dust emission are co-spatial. I derive an Einstein radius $\theta_E = 1.03''$, higher than B13's result ($\theta_E = 0.88''$). The estimate is instead in agreement with the finding of Calanog et al. (2014) and Negrello et al. (in

prep.; based on *HST*/WFC3 imaging data). Interestingly, the reconstructed background source is very elongated. This is due to the presence of two partially blended knots of emission, a main one extending across the tangential caustic and a second, fainter one located just off the fold of the caustic. This is another example where the assumption that the source is represented by a single Sérsic profile, made by B13, is probably affecting the estimated lens model parameters.

HATLASJ133649.9+291801: This is the single-lens system in the sample with the smallest Einstein radius, $\theta_{\rm E} = 0.4''$. The lens modelling gives results consistent with those of B13.

HATLASJ134429.4+303036: This is the 500 μm brightest lensed galaxy in the entire N17 sample. The observed lensed images indicate a typical cusp configuration, similar to what was observed in the well studied lensed galaxy SDP.81 (e.g. Dye et al., 2015), where the background galaxy lies on the fold of the tangential caustic. According to the modelling the lens is significantly elongated ($q_{\rm L} = 0.53$) in the North-South direction, consistent with what is indicated by available *HST*/WFC3 imaging data for the light distribution of the foreground galaxy (see Fig. 3 of N17). I estimate a higher Einstein radius than the one reported by B13, although the two results are still consistent within 2σ.

HATLASJ142413.9+022303: This source - a 500 μm "riser" - was first presented in Cox et al. (2011) while the lens modelling, based on SMA data, was performed in Bussmann et al. (2012). Observations carried out with *HST*/WFC3 and *Keck*/AO (Calanog et al., 2014) revealed two foreground galaxies, separated by $\sim 0.3''$, although only one currently has a spectroscopic redshift, $z = 0.595$ (B13). No emission from the background galaxy is detected in the near-IR. B13 modelled the system using two SIE profiles. I attemped the same but found no significant improvement in the results compared to the case of a single SIE mass distribution, which I have adopted here. I find $\theta_{\rm E} = 0.97''$, consistent with the value derived from the lens modelling of ALMA data performed by Dye et al. (2017), which also assumed a single SIE profile. On the other hand B13 obtained $\theta_{\rm E,1} = 0.57''$ and $\theta_{\rm E,2} = 0.40''$ for the two lenses. In this case the comparison with the B13 results is not straightforward. It is also

important to note, as shown in Fig. 3.4.1 [see also Dye et al. (2017)], that the background source has a complex extended morphology, which cannot be recovered by a single Sérsic profile. Bussmann et al. (2012) modelled this system assuming two Sérsic profiles for the background galaxy but their results, particularly for the position of the second knot of emission in the SP, disagree with mine and with the findings of Dye et al. (2017).

According to these findings, in single-lens systems the use of an analytic model for the source surface brightness does not bias the results on the SIE lens parameters as long as the background galaxy is not partially resolved into multiple knots of emission. A way to overcome this problem would be to test the robustness of the results by adding a second source during the fitting procedure. However, the drawback of this approach is the increase in the number of free parameters and, therefore, the increased risk of degeneracies in the final solution.

3.4.2 Source magnifications and sizes

Fig. 3.4.3 shows, for each source, how the value of the magnification varies with the size of the region in the SP, as defined by the SNR of the pixels and here expressed in terms of $r_{\rm eff}$. The values of $\mu_{3\sigma}$ and $\mu_{5\sigma}$ are shown at the corresponding effective radii (light and dark blue squares, respectively), together with the magnification factor estimated by B13 (red dots). The latter is placed at a radius $r_{\rm eff} = 2 \times r_{\rm half}$, where $r_{\rm half}$ is the mean half-light radius of the Sérsic profile used by B13 to model the source surface brightness. It is calculated as $r_{\rm half} = a_{\rm s}\sqrt{1-\varepsilon}$, with $a_{\rm s}$ and ε being the half-light semi-major axis length and ellipticity of the Sérsic profile provided by B13. B13 computed the magnification factor for an elliptical aperture in the SP with semi-major axis length equal to $2 \times a_{\rm s}$. It is easy to show that the area of this region is exactly equal to

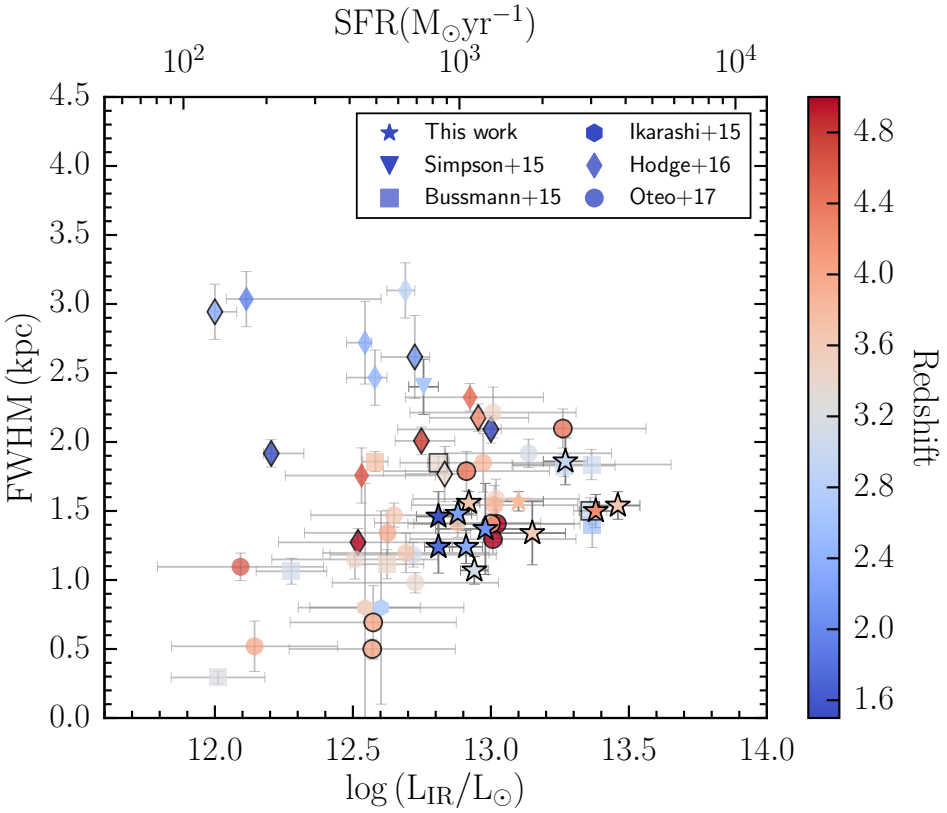

Figure 3.4.4: FWHMs of the sources in our sample (stars) as a function of their infrared luminosity, compared to results from literature: Simpson et al. (2015, triangle), Bussmann et al. (2015, squares), Ikarashi et al. (2015, hexagons), Hodge et al. (2016, diamonds), Oteo et al. (2017b, circles). All the sources taken from literature were fitted or (for the lensed ones) modelled using Gaussians and here we report, as an effective radius, the geometric mean of the values of the FWHM along the minor and the major axis. The only exception is the point of Simpson et al. which represents the median of the $FWHM_{major}$ values for their sample (see Section 3.4.2). The data points are colored according to their redshift. Most objects have a photometric redshift estimate; those with a spectroscopic redshift measurement are highlighted by a dense black outline.

Table 3.4.3: Intrinsic properties of the 12 sources in our sample. The correction for the effect of lensing has been implemented by using the value $\mu = \mu_{3\sigma}$ for the magnification as reported in Table 3.4.2. The dust temperature, T_{dust}, and the dust luminosities, L_{FIR} (integrated in the rest-frame wavelength range 40-120 μm and L_{IR} (integrated over 8-1000 μm in the rest-frame), are derived by fitting the *Herschel* and SMA photometry with a modified blackbody spectrum with dust emissivity index $\beta = 1.5$, as in Bussmann et al. (2013). Star formation rates, SFR, are estimated from L_{IR} following Kennicutt and Evans (2012). The dust luminosity and SFR densities are computed as $\Sigma_{FIR} = L_{FIR}/A_{dust,3\sigma}$, $\Sigma_{IR} = L_{IR}/A_{dust,3\sigma}$ and $\Sigma_{SFR} = SFR/A_{dust,3\sigma}$, with the values of $A_{dust,3\sigma}$ taken from Table 3.4.2.

IAUname	T_{dust} K	$\log L_{FIR}$ ($L_\odot$)	$\log L_{IR}$ ($L_\odot$)	SFR ($M_\odot yr^{-1}$)	$\log \Sigma_{FIR}$ ($L_\odot$ kpc^{-2})	$\log \Sigma_{IR}$ ($L_\odot$ kpc^{-2})	Σ_{SFR} ($M_\odot yr^{-1}$ kpc^{-2})
HATLASJ083051.0+013225	44.4±0.6	13.15±0.08	13.44±0.08	3540±560	11.63±0.08	11.91±0.08	105±25
HATLASJ085358.9+015537	37.4±0.7	12.94±0.17	12.97±0.17	1220±400	11.73±0.16	11.77±0.16	75±34
HATLASJ090740.0-004200	43.9±1.2	12.60±0.06	12.86±0.06	940±130	11.34±0.08	11.59±0.08	51±11
HATLASJ091043.1-000321	39.4±0.9	12.73±0.05	12.82±0.05	860±90	11.71±0.13	11.80±0.13	81±22
HATLASJ120127.6-014043	35.9±3.9	13.07±0.08	13.07±0.08	1530±260	11.55±0.07	11.55±0.07	46±10
HATLASJ125135.4+261457	41.2±0.7	12.81±0.03	12.96±0.03	1190±80	11.45±0.06	11.60±0.06	51±7
HATLASJ125632.7+233625	40.0±0.6	13.11±0.11	13.22±0.11	2140±470	11.76±0.13	11.87±0.13	96±32
HATLASJ132630.1+334410	38.6±0.6	13.21±0.09	13.27±0.09	2440±430	11.59±0.10	11.65±0.10	59±16
HATLASJ133008.4+245900	44.4±0.8	12.66±0.05	12.95±0.05	1150±120	11.52±0.07	11.80±0.07	82±15
HATLASJ133649.9+291801	36.0±0.7	12.93±0.03	12.93±0.03	1090±80	11.78±0.05	11.77±0.05	77±11
HATLASJ134429.4+303036	38.1±0.4	12.89±0.05	12.94±0.05	1140±130	11.73±0.08	11.79±0.08	80±16
HATLASJ142413.9+022303	39.6±1.0	13.20±0.08	13.32±0.08	2740±450	11.91±0.06	12.03±0.06	139±28

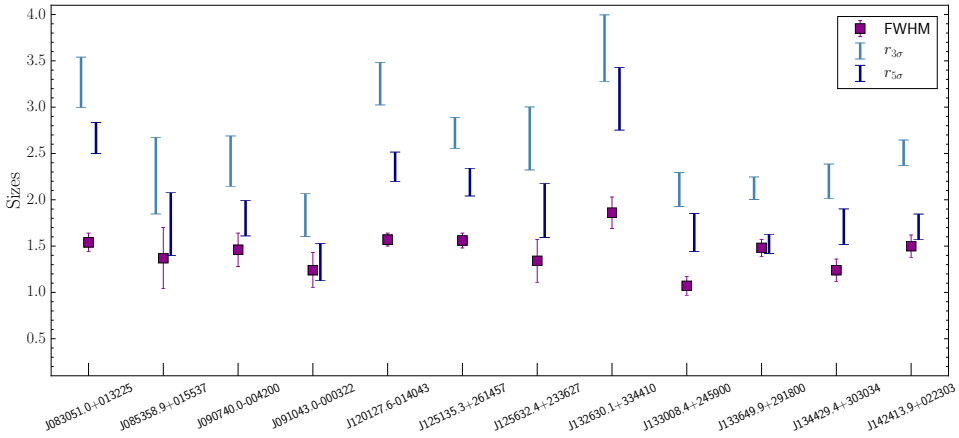

Figure 3.4.5: Comparison between the measured 5σ and 3σ effective radius and the geometric mean of the values of the FWHM along the minor and the major axis obtained from a Gaussian fit to the reconstructed source plane. The FWHMs are systematically lower then the reported effective radii obtained for a certain value of the signal-to-noise ratio, due to lost features not retrieved by the Gaussian fit.

Table 3.4.4: Same as in Table 3.4.3, but this time assuming $\mu = \mu_{5\sigma}$ and $A_{\rm dust} = A_{{\rm dust},5\sigma}$. The dust temperature is not listed here because it does not depend on the magnification, unless differential magnification is affecting the far-IR to sub-mm photometry.

IAUname	$\log L_{FIR}$ ($L_\odot$)	$\log L_{IR}$ ($L_\odot$)	SFR ($M_\odot yr^{-1}$)	$\log \Sigma_{FIR}$ ($L_\odot$ kpc^{-2})	$\log \Sigma_{IR}$ ($L_\odot$ kpc^{-2})	Σ_{SFR} ($M_\odot yr^{-1}$ kpc^{-2})
HATLASJ083051.0+013225	13.17±0.08	13.46±0.08	3720±650	11.83±0.06	12.11±0.06	167±35
HATLASJ085358.9+015537	12.95±0.18	12.98±0.18	1250±430	11.98±0.21	12.01±0.21	132±69
HATLASJ090740.0-004200	12.56±0.08	12.81±0.08	840±150	11.55±0.09	11.80±0.09	82±22
HATLASJ091043.1-000321	12.72±0.05	12.81±0.05	840±100	11.98±0.15	12.07±0.15	152±48
HATLASJ120127.6-014043	13.12±0.09	13.10±0.09	1650±320	11.87±0.06	11.86±0.06	95±23
HATLASJ125135.4+261457	12.77±0.04	12.92±0.04	1090±90	11.60±0.07	11.75±0.07	72±12
HATLASJ125632.7+233625	13.04±0.12	13.15±0.12	1840±450	12.00±0.16	12.11±0.16	166±65
HATLASJ132630.1+334410	13.20±0.08	13.27±0.08	2410±400	11.73±0.10	11.79±0.10	81±21
HATLASJ133008.4+245900	12.65±0.05	12.94±0.05	1120±110	11.72±0.12	12.01±0.12	132±35
HATLASJ133649.9+291801	12.88±0.05	12.88±0.05	980±100	12.02±0.06	12.01±0.06	134±23
HATLASJ134429.4+303036	12.86±0.06	12.91±0.06	1060±140	11.90±0.09	11.95±0.09	116±27
HATLASJ142413.9+022303	13.26±0.06	13.38±0.06	3130±400	12.30±0.08	12.42±0.08	344±71

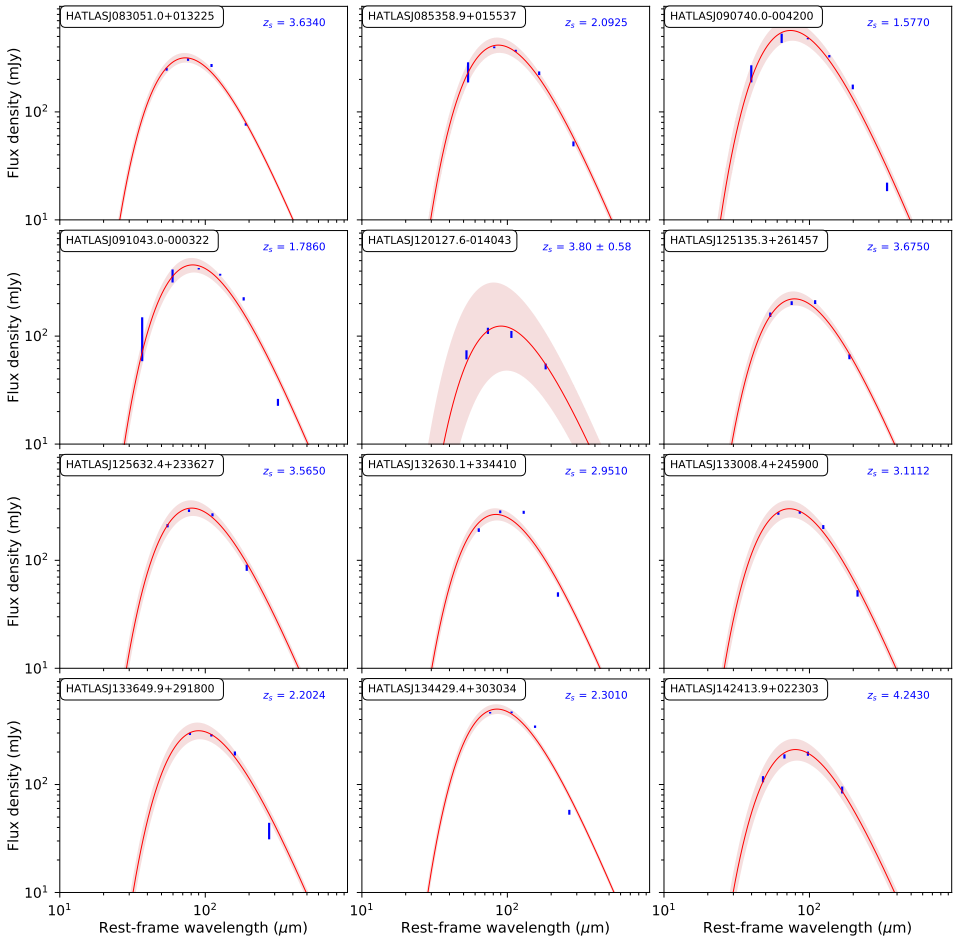

Figure 3.4.6: Observed far-IR to sub-mm SEDs of the 12 sources (blue error bars; from *Herschel* and SMA) together with the best-fitting modified blackbody spectrum (red curve; assuming dust emissivity index $\beta = 1.5$). The shaded red area shows the 68% confidence region associated with the best-fitting model. The redshift of the source is reported on the top-right corner of each panel. The redshift is spectroscopic for all the sources but one, i.e. HATLAS J120127.6-014043. This accounts for the significantly larger uncertainity in the fit to the SED of HATLAS J120127.6-014043 compared to the other sources.

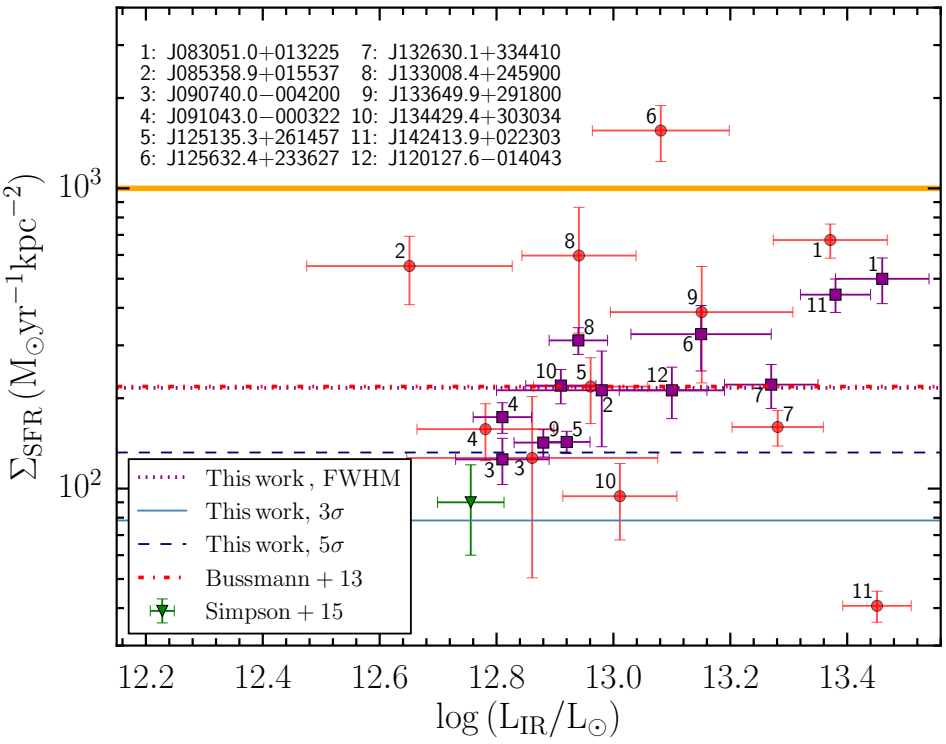

Figure 3.4.7: Star formation rate surface density as a function of infrared luminosity for the sources in our sample. The dark magenta squares correspond to the case $\mu = \mu_{5\sigma}$ and $A_{\rm dust} = A_{\rm dust,FWHM}$. The dotted dark magenta line marks their median value. The median value of $\Sigma_{\rm SFR}$ for the case $\mu = \mu_{5\sigma}$ and $A_{\rm dust} = A_{\rm dust,5\sigma}$ is shown by the dotted blue line, while the case of $\mu = \mu_{3\sigma}$ and $A_{\rm dust} = A_{\rm dust,3\sigma}$ is the continuous cyan line. For comparison we show the data points from B13 (red dots; calculated as explained in Section 3.4.3) and the median value of the SFR surface density of DSFGs from the Simpson et al. (2015) sample (green triangle). The yellow line marks the Eddington limit for a radiation pressure supported starburst galaxy (Thompson et al., 2005, Andrews and Thompson, 2011).

$\pi \times (2 \times r_{\rm half})^2$.

In general I find lower values of the magnification factor compared to B13. Discrepancies are to be expected for systems like HATLASJ083051.0+013225 and HATLASJ142413.9+022303, where the best-fitting lens model parameters differ significantly from those of B13. However a similar explanation may be also applied to systems like HATLASJ085358.9+015537, HATLASJ091043.0-000322, and HATLAS134429.4+303034. In HATLAS125135.3+261457 and HATLASJ125632.4+233626 the reconstructed source morphology is indicative of the presence of two partially blended components. The complexity of the source is not recovered by a single Sérsic profile and a significant fraction of the source emission lies beyond the region defined by B13 to compute μ. As a consequence their magnification factor is higher than our estimate. HATLASJ090740.0-004200, HATLASJ132630.1+334410 and HATLASJ133649.9+291800 are the only systems where my findings are quite consistent with those of B13 for both the source size and the magnification.

In Fig. 3.4.4 I show the effective radius of the dust emitting region in DSFGs at $1.5 \lesssim z \lesssim 5$ from the literature, as a function of their infrared luminosity ($L_{\rm IR}$, integrated over the rest-frame wavelength range 8-1000 μm). Most of these estimates are obtained from ALMA continuum observations by fitting an elliptical Gaussian model to the source surface brightness. The value of $r_{\rm eff}$ reported in the figure is the geometric mean of the values of the FWHM of the minor and major axis lengths, unless otherwise specified. I provide below a brief description of the source samples presented in Fig. 3.4.4.

Simpson et al. (2015) carried out ALMA follow-up observations at 870μm, with $\sim 0.3''$ resolution, of 52 DSFGs selected from the SCUBA-2 Cosmology Legacy Survey (S2CLS). They provide the median value of the FWHM of the major axis for the sub-sample of 23 DSFGs detected at more than 10 σ in the ALMA maps: $\mathrm{FWHM}_{\rm major} = 2.4 \pm 0.2$ kpc. The median infrared luminosity of the same sub-sample is $L_{\rm IR} = (5.7 \pm 0.7) \times 10^{12} L_{\odot}$. These are the values I show in Fig. 3.4.4 (triangular symbols), bearing in mind that I have no information on

the ellipticity of the sources to correct for. Therefore, when comparing with other data sets, the Simpson et al. point should be considered as an upper limit.

Bussmann et al. (2015) have presented ALMA 870 μm imaging data, at 0.45$''$ resolution, of 29 DSFGs from the *Herschel* Multi-tiered Extragalactic Survey (HerMES; Oliver et al., 2012). The sample includes both lensed and unlensed objects. Lens modelling is carried out assuming an elliptical Gaussian. The un-lensed galaxies are also modelled with an elliptical Gaussian. Their results are shown in Fig. 3.4.4 (square symbols), with FWHM$= 2 \times r_s$, where r_s is the geometric mean of the semi-axes, as reported in their Table 3. The infrared luminosity of the lensed sources have been corrected for the magnification. I only show the sources in their sample that are not resolved into multiple components as no redshift and infrared luminosity are available for the individual components. This reduces their sample to nine objects: eight strongly lensed and one un-lensed.

Ikarashi et al. (2015) have exploited ALMA 1.1 μm continuum observations to measure the size of a sample of 13 AzTEC-selected DSFGs with $z_{\rm phot} \sim 3-6$ and $L_{\rm IR} \sim 2-6 \times 10^{12} L_{\odot}$. They fit the data in the *uv*-plane assuming a symmetrical Gaussian. In Fig. 3.4.4 I show their findings as FWHM$= 2 \times R_{c,e}$ (hexagon symbols), where $R_{c,e}$ is the value they quote in their Table 1 for the half-width at half-maximum of the symmetric Gaussian profile. Their 1.1 μm flux densities have been rescaled to 870 μm by multiplying them by a factor 1.5 (see Oteo et al. 2017). For most of the sources in the Ikarashi et al. sample the redshift is loosely constrained, with only lower limits provided. Therefore I only consider here two sources in their sample with an accurate photometric redshift, i.e. ASXDF1100.027.1 and ASXDF1100.230.1.

Hodge et al. (2016) used high resolution ($0.16''$) ALMA 870μm continuum observations of a sample of 16 DSFGs with $1 \lesssim z \lesssim 5$ and $L_{\rm IR} \sim 4 \times 10^{12}\, L_{\odot}$ from the LABOCA Extended *Chandra* Deep Field South (ECDFS) sub-mm survey (LESS; Karim et al., 2013, Hodge et al., 2013) to investigate their size and morphology. Their results are represented by the diamond symbols in Fig. 3.4.4.

Oteo et al. (2017b, 2016) have performed ALMA 870 μm continuum

observations, at $\sim 0.12''$ resolution, of 44 ultrared DSFGs (i.e. with *Herschel*/SPIRE colors: $F_{500\mu m}/F_{250\mu m} > 1.5$ and $F_{500\mu m}/F_{350\mu m} > 1$). They confirmed a significant number of lensed galaxies, which I do not consider here because no lens modelling results are available for them yet. I only consider un-lensed objects for which Oteo et al. provide a photometric or a spectroscopic redshift (Oteo et al., 2016, Riechers et al., 2017, Fudamoto et al., 2017). When a source is resolved into multiple components, each component is fitted individually and an estimate of the SFR (and, therefore, of L_{IR}) is provided based on the measured 870 μm flux density. The circles in Fig. 3.4.4 show their findings.

In order to compare with the data from literature I also fit my reconstructed source surface brightness using an elliptical Gaussian model. The derived values of the FWHM along the major and the minor axis of the ellipse are reported in Table 3.4.2 together with their geometric mean $FWHM_m = \sqrt{FWHM_{maj} \times FWHM_{min}}$. However the reader should be warned that the use of a single Gaussian profile to model the observed surface brightness of DSFGs could bias the inferred sizes because of the clumpy nature of these galaxies, as partially revealed by my SMA data. In fact, I find that the values of $FWHM_m$ are systematically lower than those of $r_{eff,5\sigma}$ and $r_{eff,3\sigma}$, as demonstrated in Fig.3.4.5.

With this caveat in mind, I show in Fig. 3.4.4 the size of the dust emitting region derived from the Gaussian fit to our reconstructed source surface brightness. The infrared luminosity, obtained from a fit to the observed spectral energy distribution (see Section 3.4.3 for details), has been corrected for lensing by assuming[1] $\mu = \mu_{5\sigma}$.

In Fig. 3.4.4 the data points are coloured according to their redshift. Most of the objects have a photometric redshift estimate; those with a spectroscopic redshift are highlighted by a black line. We observe a significant scatter in the distribution of the source sizes, particularly at the lowest luminosities, with values ranging from $\lesssim 0.5$ kpc to $\gtrsim 3$ kpc. The lack of sources with $r_{eff} \lesssim 1$ kpc

[1] Note that, according to Fig. 3.4.3, the magnification factor does not change significantly between the scales $r_{eff} = r_{eff,5\sigma}$ and $r_{eff} = FWHM_m$

at $L_{IR} \gtrsim 10^{13} L_{\odot}$ is possibly a physical effect. In fact, such luminous sources would have extreme values of the SFR surface brightness, and, therefore, would be quite rare. The absence of $z > 3.5$ sources with $r_{eff} \gtrsim 1.5$ kpc and $L_{IR} \lesssim 3 \times 10^{12} L_{\odot}$ is likely due to their lower surface brightness, which makes these objects difficult to resolve in high resolution imaging data. Based on these considerations it is challenging to draw any conclusion about the dependence of the size on either luminosity or redshift.

The sources in my sample have a median effective radius $r_{eff,5\sigma} \sim 1.77$ kpc, rising to $r_{eff,3\sigma} \sim 2.46$ kpc if I consider all the pixels in the SP with SNR > 3, while the median FWHM of the Gaussian model is ~ 1.47 kpc. These values are consistent with what observed for other DSFGs at similar, or even higher, redshifts.

3.4.3 Star formation rate surface densities

I derive the star formation rate, SFR, of the sources in my sample from the magnification-corrected IR luminosity, L_{IR}, using the Kennicutt and Evans (2012) relation:

$$\mathrm{SFR}\,(M_{\odot}\,\mathrm{yr}^{-1}) \sim 1.3 \times 10^{-10}\,L_{IR}\,(L_{\odot}) \tag{3.1}$$

which assumes a Kroupa initial mass function (IMF). B13 provide an estimate of the total far-infrared (FIR) luminosity, L_{FIR} (integrated over the rest-frame wavelength range 40-120 μm), of the sources in their sample by performing a fit to the measured *Herschel*/SPIRE and SMA photometry using a single temperature, optically thin, modified blackbody spectrum with dust emissivity index $\beta = 1.5$. The normalization of the spectrum and the dust temperature, T_{dust}, were the only free parameters. I have repeated that exercise using the *Herschel*/SPIRE photometry from the latest release of the *H*-ATLAS catalogues (Valiante et al., 2016, Furlanetto et al. in prep.; as listed in N17, their Table 4), including also the *Herschel*/PACS photometric data points, where available. The fit is performed using a Monte Carlo approach outlined in N17, to account for

uncertainities in the photometry and in the redshift when the latter is not spectroscopically measured, as in the case of HATLASJ120127.6-014043. The observed spectral energy distribution (SED) and the best-fitting model are shown in Fig. 3.4.6. he larger uncertainty in the source photometric redshift is reflected in a larger uncertainty in the retrieved parameters, immediately visible in the fit. It is worth noticing that effects such as data blending - due to the relatively large angular resolution of PACS/SPIRE instruments -, unresolved flux or differential magnification - the fact that the μ retrieved for emission at 880 μm is not necessarily the same μ of the emission at different wavelengths - might affect the SED fitting, particularly in those sources where the χ^2 appears bad.

The inferred infrared luminosities and star formation rates are listed in Table 3.4.3 and they have been corrected for the effect of lensing by assuming $\mu = \mu_{3\sigma}$ (see Table 3.4.2). To directly compare with B13 I also report, in the same table, the magnification-corrected far-IR luminosity. Table 3.4.4 shows the same results but corrected assuming $\mu = \mu_{5\sigma}$. The dust temperature is not listed in that table because it does not depend on lensing, unless differential magnification is affecting the far-IR to sub-mm photometry, thus biasing the results of the SED fitting. Unfortunately this is something that cannot be tested with the current data.

In both Table 3.4.3 and Table 3.4.4 I report the dust luminosity and star formation rate surface densities, defined as $\Sigma_{\rm IR} = {\rm L_{IR}}/A_{\rm dust}$ and $\Sigma_{\rm SFR} = {\rm SFR}/A_{\rm dust}$ respectively. Both are corrected for the magnification and computed using the value of $A_{\rm dust}$ corresponding to the adopted SNR threshold in the SP.

Fig. 3.4.7 shows the SFR surface density of the sources in our sample as a function of their infrared luminosity (squares). I find median values $\Sigma_{\rm SFR,FWHM} = 215 \pm 114\, M_\odot\ {\rm yr}^{-1}{\rm kpc}^{-2}$ (dark magenta line) inside the region of radius $r = {\rm FWHM_m}$, and $\Sigma_{\rm SFR,5\sigma} = 132 \pm 69\, M_\odot\ {\rm yr}^{-1}{\rm kpc}^{-2}$ (dashed blue line) and $\Sigma_{\rm SFR,3\sigma} \sim 78 \pm 25\, M_\odot\ {\rm yr}^{-1}{\rm kpc}^{-2}$ (dotted cyan line) inside the regions in the source plane with SNR $\geq$ 5 and SNR $\geq$ 3, respectively. The red circles are the findings of B13 for the same sources. I have computed them by taking the

FIR luminosity quoted by B13 and first converting it into L_{IR} (by multiplying L_{FIR} by a factor 1.9, as reported in B13) and then into SFR using Eq. (3.1). Then I have divided the SFR by the source area calculated as $A_{dust} = \pi r_{half}^2$. Finally I have divided the result by 2. In fact, by definition, the region within the circle of radius r_{half} contributes only half of the total luminosity (and therefore SFR) of the source. The median value of the SFR surface densities calculated in this way is $\Sigma_{SFR} \sim 219\, M_\odot\ \mathrm{yr}^{-1}\mathrm{kpc}^{-2}$ (dot-dashed red line) which is similar to our estimate inside the region of radius FWHM, although the data points of B13 (red circles) display a much larger scatter than ours, and higher than our estimate inside the region defined with SNR. It is notable that the SFR surface density calculated in this way - although consistent with what done in other works (e.g. Simpson et al., 2015, Oteo et al., 2017c) - is not representative of the galaxy as a whole, but only of the central region, where the emission is likely to be more concentrated. Therefore such an estimate should be taken as an upper limit for the SFR surface brightness of the whole galaxy. However I cannot exclude that individual star forming regions, resolved in higher resolution imaging data, may show significantly higher values of Σ_{SFR}.

I also show, in the same figure, the median SFR surface density of DSFGs from the Simpson et al. (2015) sample (green triangle). They estimated $\Sigma_{SFR} = 90 \pm 30\, M_\odot\ \mathrm{yr}^{-1}\mathrm{kpc}^{-2}$, assuming a Salpter IMF, which decreases to $\Sigma_{SFR} \sim 67\, M_\odot\ \mathrm{yr}^{-1}\mathrm{kpc}^{-2}$ if I assume a Kroupa IMF as in Eq. (3.1). Their estimate of the SFR surface density is consistent with ours, although their sample has a lower infrared luminosity on average. However their way of calculating Σ_{SFR} is exactly the same I have adopted to draw the B13 data points in Fig. 3.4.7 and therefore it is affected by the same caveat discussed above.

The solid yellow line, at $\sim 1000\, M_\odot\ \mathrm{yr}^{-1}\mathrm{kpc}^{-2}$, marks the theoretical limit for the SFR surface density in a radiation pressure supported star forming galaxy (Thompson et al., 2005, Andrews and Thompson, 2011). None of our sources are close to that limit, at variance with what was found by B13. However I cannot exclude, as mentioned before, that individual star forming regions, not fully resolved by our current data, may reach the theoretical limit or even exceed it.

3.5 Conclusions

This Chapter is based on the reassessment of the results of lens the lens modelling and source reconstruction presented in Bussmann et al. (2013) on the SMA observations of a sample of 11 lensed galaxies selected from the *H*-ATLAS. Our group observed 7 new H-ATLAS sources, one of which is resolved into the typical multiple images of strong lensing, confirming the lensing nature of the source. This source is included in the sample, rising the total number of modelled source to 12.

My lens modelling is based on the Regularized Semilinear Inversion method described in Warren and Dye (2003) and Nightingale and Dye (2015), modified to deal directly with the observed visibilities in the *uv* plane, as extensively reported in Chapter 2. SLI is a semi-parametric method, meaning that the source surface brightness counts are retrieved by pixelizing (or tesselating as in this case) both the observed image plane and the source plane. This differs from what was done in B13, where the source was assumed to be described by a single Sérsic profile. In this way, I'm able to retrieve the original source morphology, which, for these kind of sources, is usually clumpy.

As expected, when the reconstructed source does not display complex morphologies, my results for the lens mass model agree in general with those of B13. The only exceptions involve the modelling of multiple lens systems (just two in our sample), where degeneracies between model parameters are more likely to occur.

The adopted source reconstruction technique allows me to define a signal-to-noise ratio map in the source plane. I use it to define the area of the dust emitting region in the source plane and its corresponding magnification, while in B13, the source extension is an arbitrary factor of the half-light radius of the adopted Sérsic profile. I report the size of the reconstructed sources in my sample as the radius of a circle whose area corresponds to all the source plane pixels with SNR > 5 (or SNR > 3). However, for a more straightforward comparison with results in literature, I also quote the value of the FWHM obtained from a

Gaussian fit to the reconstructed source plane. For almost 50 percent of our sample the estimated effective radii are larger than $2 \times r_{\rm half}$, i.e. the radius of the region chosen by B13 to represent the source physical size when computing the magnification. As a consequence, I derived, in general, lower magnification factors than those quoted in B13.

Once corrected for the magnification, the sources still retain very high star formation rates SFR $\sim 900 - 3500\, M_{\odot}{\rm yr}^{-1}$, assuming that the bulk of sub-mm emission is due to young stars. With a median effective radius $r_{\rm eff,5\sigma} \sim 1.77$ kpc ($r_{\rm eff,3\sigma} \sim 2.46$ kpc) and a median FWHM ~ 1.47 kpc, the sample has a median SFR surface density $\Sigma_{\rm SFR,5\sigma} \sim 132\, M_{\odot}$ yr^{-1} kpc^{-2} ($\Sigma_{\rm SFR,3\sigma} \sim 78\, M_{\odot}$ yr^{-1} kpc^{-2} or $\Sigma_{\rm SFR,FWHM} \sim 215\, M_{\odot}$ yr^{-1} kpc^{-2} from the Gaussian fit). This is consistent with what is observed for other DSFGs at similar redshifts, but it is only $\sim$10 percent of the limit achievable in a radiation pressure supported starburst galaxy.

4

A benchmark study of SF/AGN co-evolution

Since the discovery of the high-z population of sub-mm galaxies, different evolutionary models have been introduced in the literature to account for the existence of this population, rarely observed in the local Universe. A key aspect that has been investigated in recent years is the growing evidence of a connection in the central region of the forming galaxy between the star formation and the nuclear activities, driven by gravitational accretion onto a supermassive nuclear black hole (Franceschini et al., 1999). This co-evolution is able to affect the evolution of the whole system, since star formation refills the torus reservoir of the central AGN with large amounts of gas in the first stages of the system evolution, and the growing energetic feedback coming from the AGN can then completely quench star formation processes in the galaxy in the latter stages of its

evolution.

Star formation usually takes place with very intense episodes that build up most of the observed stellar mass, as per measurements of stellar metallicities $Z_* \geq Z_\odot$ (Thomas et al., 2005, Gallazzi et al., 2014), star formation efficiency $f_* \equiv M_*/f_b M_H \leq 0.2$ coming from weak-lensing observations (Velander et al., 2014, Hudson et al., 2015, Mandelbaum et al., 2016) or abundance matching arguments (Moster et al., 2018). These short episodes occur at redshifts $z > 1$, and generate a homogeneous stellar population.

After this phase of very intense star formation, the galaxy undergoes a quenching phase, via a feedback mechanism likely coming from the Active Galactic Nucleus (AGN). The gas is swept away, star formation stops. Observations of α-enhancement in ETGs show a defect of iron compared to α elements, hinting at the fact that the quenching phase should occur before SN*Ia* explosions are able to spread iron in the galaxy environments. The mechanism responsible for the quenching is therefore due to feedback coming from the central supermassive black hole (BH). In fact, almost every massive ETGs observed in the local Universe host at the center a BH with masses $M_{\rm BH} \sim 10^7 - 10^9 M_\odot$. This is a clear signal that a coevolution between the BH build-up and the stellar component has taken place (Franceschini et al., 1999, Kormendy and Ho, 2013, Shankar et al., 2016, van den Bosch, 2016).

In this Chapter I report multiwavelength observations of two H-ATLAS sources, H-ATLASJ090740.0-004200 and H-ATLASJ091043.1-000322, whose source emission has been detected from X-ray with Chandra to near-IR with HST to sub-mm/mm with SMA and ALMA (Massardi et al., 2018). For the first source, I also modelled the lens, reconstructing the source morphology, clearly retrieving a co-spatiality between the Chandra and ALMA emissions. The second source presents some complications that make lens modelling hard to achieve, primarly the presence of a strong source of external shear close to lensed emission. In order to link the Massardi et al. (2018) results with a more general phenomenological analysis, I also briefly report in the next Section the fundamentals of the SISSA-PD galaxy evolutionary model, and how they relate to

gravitational lensing.

4.1 The SISSA-PADOVA model

The model foundations are built on two main components: dark matter, hirerchically accreting from merging and aggregation of minor components, and baryonic matter, collapsing anti-hierachically inside the dark matter gravitational well, i.e. the more massive the baryonic component, the faster the evolutionary steps. In this scenario, the baryonic initial mass $M_{\rm bar}$ plays a fundamental role in determining the evolution of the system: the more massive the baryonic component, the shorter are the single evolutionary phases. As a consequence, the central AGN forms earlier with a bigger mass, so its feedback processes quenching the star formation inside the whole galaxy are more efficient. Initial conditions play a fundamental role in determining the final state of the system, and in principle there's no need to make assumptions on the environment surrounding the system, or other cosmological parameters such as the epoch of reionization.

A summary of the evolutionary steps for the baryonic component (i.e. physical sizes, mass, timescales) are reported in Lapi et al. (2018) (L18 hereafter, see Fig. 4.1.1). A comprehensive discussion of the model is beyond the scope of this Chapter, and I refer the reader to the main references for further details. Here I report the key concepts, and how they relate with observations and modeling of gravitationally lensed DSFGs. All the following reported equations are taken from L18. All the scaling relations are normalized to the values obtained for a reference mass $M_* = 10^{11} M_\odot$, with star formation efficiency $f_* \sim 0.2$ and infall fraction, i.e. the fraction of available baryons that cools down and fall in the starforming regions, $f_{inf} \sim 0.6$. The general solution for different M_* are shown in Fig. 4.1.2.

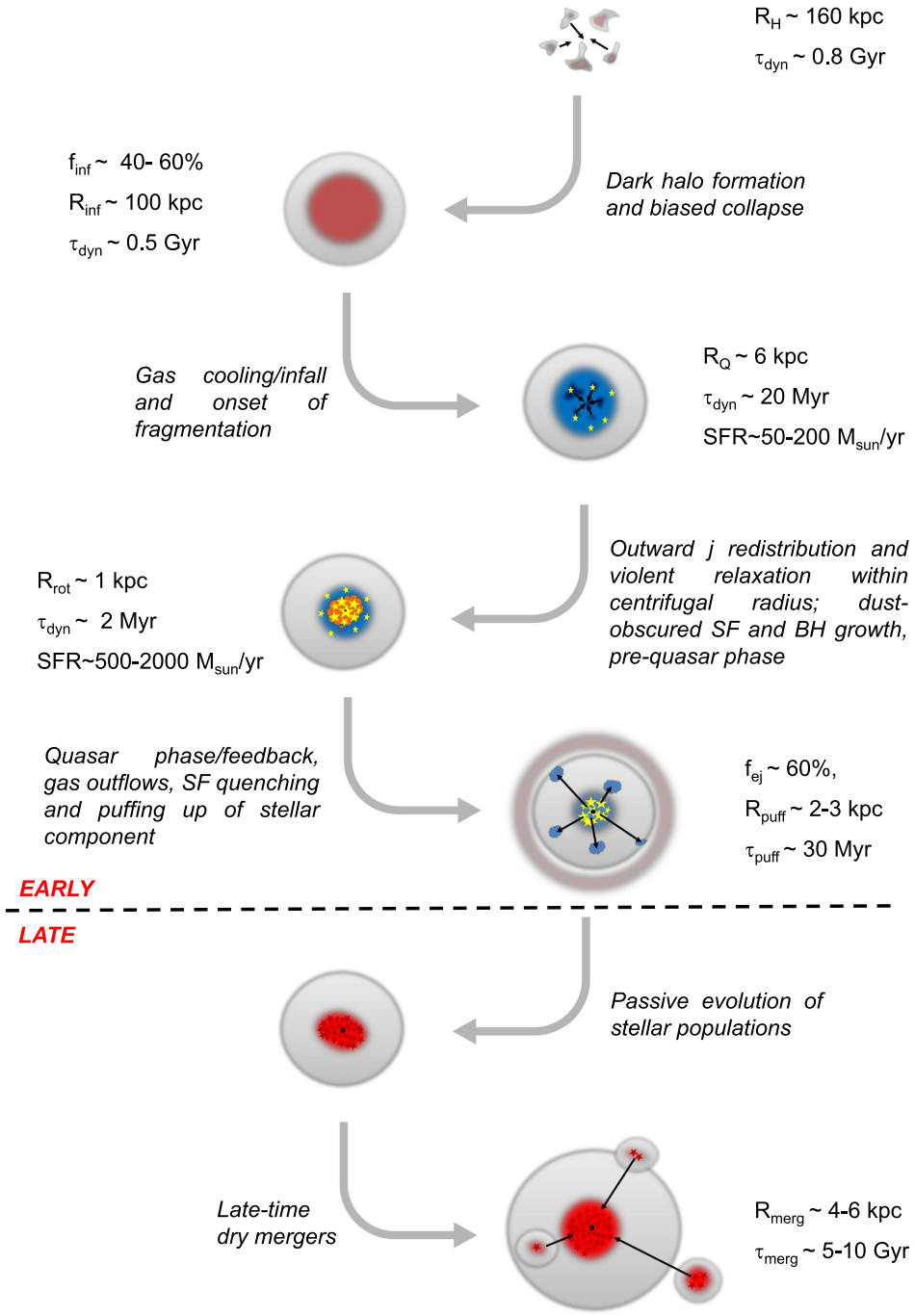

Figure 4.1.1: ETGs progenitors size and timescale evolution for a $M_* = 10^1 1 M_\odot$ galaxy in the SISSA-PD model. Early (order of 10^8 yr) and late (several Gyr) evolutionary steps are separated by a dashed black line. From Lapi et al. (2018).

4.1.1 Collapse, cooling and fragmentation

The low-angular momentum baryons collapse (*biased collapse scenario*, see Eke et al., 2000, Fall, 2002, Romanowsky and Fall, 2012, Shi et al., 2017) inside the inner regions of the in-situ dark matter gravitational well, with halo-radius

$$R_H \sim 160 f_{\mathrm{inf},\,0.2}^{-1/3} M_{*,\,11}^{1/3} \left[E_z/E_{z=2}\right]^{-1.3} \text{ kpc}. \tag{4.1}$$

with $E_z = \Omega_\Lambda + \Omega_M(1+z)^3$ a redshift-dependent term.

The gas cools, fragments and infall down to the infall-size

$$R_{\mathrm{inf}} \sim f_{\mathrm{inf}} R_H \sim 96 f_{\mathrm{inf},\,0.6} f_{*,\,0.2}^{-1/3} M_{*,\,11}^{1/3} \left[E_z/E_{z=2}\right]^{-1.3} \text{ kpc}, \tag{4.2}$$

on a dynamical timescale of

$$t_{\mathrm{dyn}}(R_{\mathrm{inf}}) \sim 5 \times 10^8 f_{\mathrm{inf},\,0.6} \left[E_z/E_{z=2}\right]^{-1/2} \text{ years}. \tag{4.3}$$

This is consistent with both observations of DSFGs and high-resolution simulations (Simpson et al., 2015, Hodge et al., 2013, Narayanan et al., 2015).

The gas falls toward the center of the halo, and a fraction becomes available for star formation. The final radius is set by dynamic arguments, particularly stability against fragmentation for rotating disk. This is verified whenever the Toomre (Toomre, 1964) parameter $Q \equiv \sqrt{2}\Omega\sigma/\pi G\Sigma$, with $\Omega \equiv v/R^2$ the angular velocity, Σ and σ respectively the gas surface density and velocity dispersion, is higher than the critical values of 0.7 - 1 - 2 for thick, thin and composite disks. The final radius is

$$R_Q \sim 6.3\, Q\sigma_{60}^{-1}\, \lambda_{0.0035} \times f_{\mathrm{inf},\,0.6}^{s} f_{*,\,0.2}^{-2/3} M_{*,11}^{2/3} \left[E_z/E_{z=2}\right]^{-1/6} \text{ kpc}, \tag{4.4}$$

reached in a timescale

$$t_{\mathrm{dyn}}(R_Q) \sim 2.2 \times 10^7\, Q^{3/2} \sigma_{60}^{-3/2}\, \lambda_{0.0035}^{3/2} \times f_{\mathrm{inf},\,0.6}^{(3s-1)/2} f_{*,\,0.2}^{-1/2} M_{*,11}^{1/2} \left[E_z/E_{z=2}\right]^{-1/4} \text{ years}. \tag{4.5}$$

Once reaching the size R_Q, gas fragmentation generates the formation of single smaller clumps, with masses $M_{\rm clumps} \leq 10^{-1} M_{\rm inf}$, that migrate toward the center over a timescale

$$t_{\rm migr}(R_Q) \sim 3.2 \times 10^8 \text{ years}. \tag{4.6}$$

Star formation is active during the whole infall phase, regulated by processes such as supernovae energy feedbacks and stellar wind. The typical estimate is

$$\text{SFR}(R_Q) \leq 50 - 200\, M_\odot \text{yr}^{-1}, \tag{4.7}$$

over a timescale

$$t_{\rm SFR} \sim 1 - 2 \times 10^9 \text{ years}, \tag{4.8}$$

consistent with near-IR observations of $z \sim 1 - 2$ star-forming galaxies (Genzel et al., 2014, van Dokkum et al., 2015, Barro et al., 2016).

4.1.2 Compactation

After 10^7 years, gas and clumps are infalled within R_Q. The process continues until gravitational and centrifugal force balance, at radius

$$R_{\rm rot} \sim 1.3\, \lambda^2_{0.0035} f^{2s-1}_{\rm inf,\,0.6} f^{-1/3}_{*,\,0.2} M^{1/3}_{*,11} \left[E_z/E_{z=2}\right]^{-1/3} \text{ kpc}, \tag{4.9}$$

over a dynamical timescale of

$$t_{\rm dyn}(R_{\rm rot}) \sim 2 \times 10^6\, \lambda^3_{0.0035} f^{3s-2}_{\rm inf,\,0.6} \left[E_z/E_{z=2}\right]^{-1/2} \text{ years}. \tag{4.10}$$

In this phase, the star formation proceeds at rates

$$\text{SFR}(R_{\rm rot}) \leq 500 - 2000\, M_\odot \text{yr}^{-1}, \tag{4.11}$$

over a timescale

$$t_{\rm SFR}(R_{\rm rot}) \sim 1 - 2 \times 10^8 \text{ years}. \tag{4.12}$$

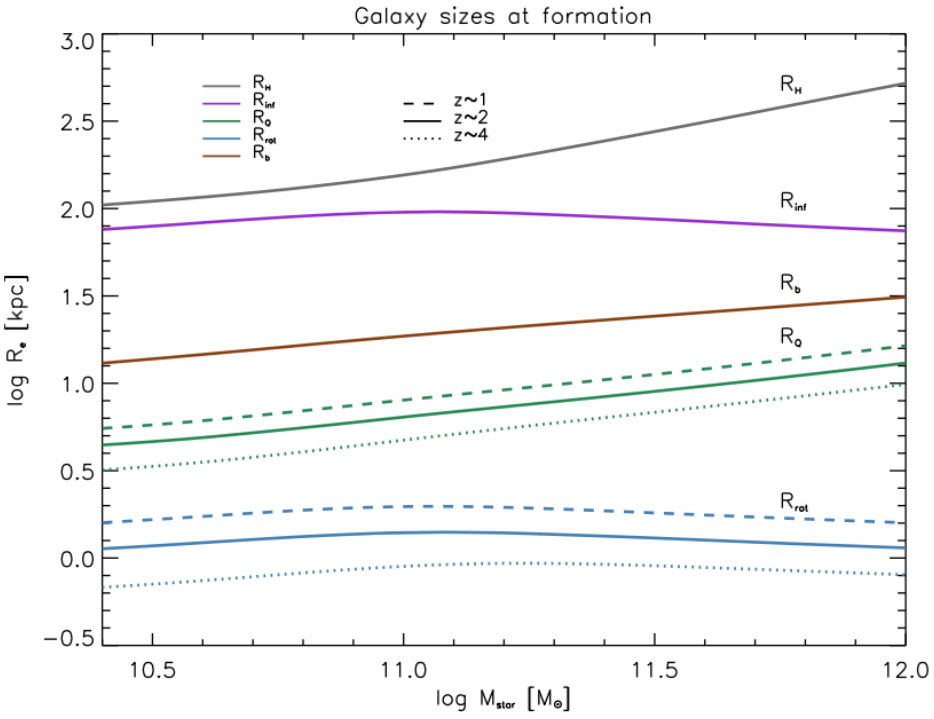

Figure 4.1.2: ETGs progenitor sizes at redshift $z \sim 2$ (solid line), $z \sim 1$ (dashed line) and $z \sim 4$ (dotted line) as a function of stellar mass M_*. DM halo-radius from Eq. 4.1 is in gray, infall-radius from Eq. 4.2 in purple, baryonic size from Eq. 4.13 in brown, fragmentation size from Eq. 4.4 in green, centrifugal size from Eq. 4.9 in blue. From L18.

In a radius of approximately 1 kpc around the galaxy center high values of SFRs are expected. In a short period of time, the most massive stars die through supernova explosions, filling the environment with high amount of dust and metals. From an observational standpoint, the model predicts a strongly or completely obscured SF in the inner regions within $R_{\rm rot}$, probed mainly with observations carried out at sub-mm/mm bands, and a mildly obscured SF in the region between $R_{\rm Q}$ and $R_{\rm rot}$, probed directly observing the UV/optical radiation field of newborn stars that escapes the dusty environments. The two SFRs regions are disconnected and the morphologies are highly irregular and clumpy, as confirmed by different observations of $z \sim 1-2$ SF galaxies (Hodge et al., 2016, Barro et al., 2017, Talia et al., 2018), along with reconstruction of strongly lensed sources at different wavelengths (e.g. Enia et al., 2018, Dye et al., 2014, 2018).

At the end of this phase, the innermost parts of the system are baryon-dominated. This region spans a radius of

$$R_b \sim 18.8 f_{\rm inf,\,0.6}^{1/2} f_{*,\,0.2}^{-1/3} M_{*,11}^{1/3} \left[E_z/E_{z=2}\right]^{-1/3} \text{ kpc}, \tag{4.13}$$

larger than $R_{\rm Q}$ and $R_{\rm rot}$.

The gas inflow towards the central regions creates the conditions for the formation and accretion onto a central supermassive BH. All this material thickens the reservoir (that is, the dusty torus of the AGN), accreting onto the central BH, creating an AGN in the central regions, with fundamental consequences on the future development of the whole system.

4.1.3 Feedback

The subsequent evolution of the galaxy is characterized by the ejection from the central regions of material via feedbacks mechanism i.e. from the quasar phase of the central AGN or from supernovae and stellar winds. These mechanism regulate, and later quench, star formation in the galaxy. Roughly speaking, if the

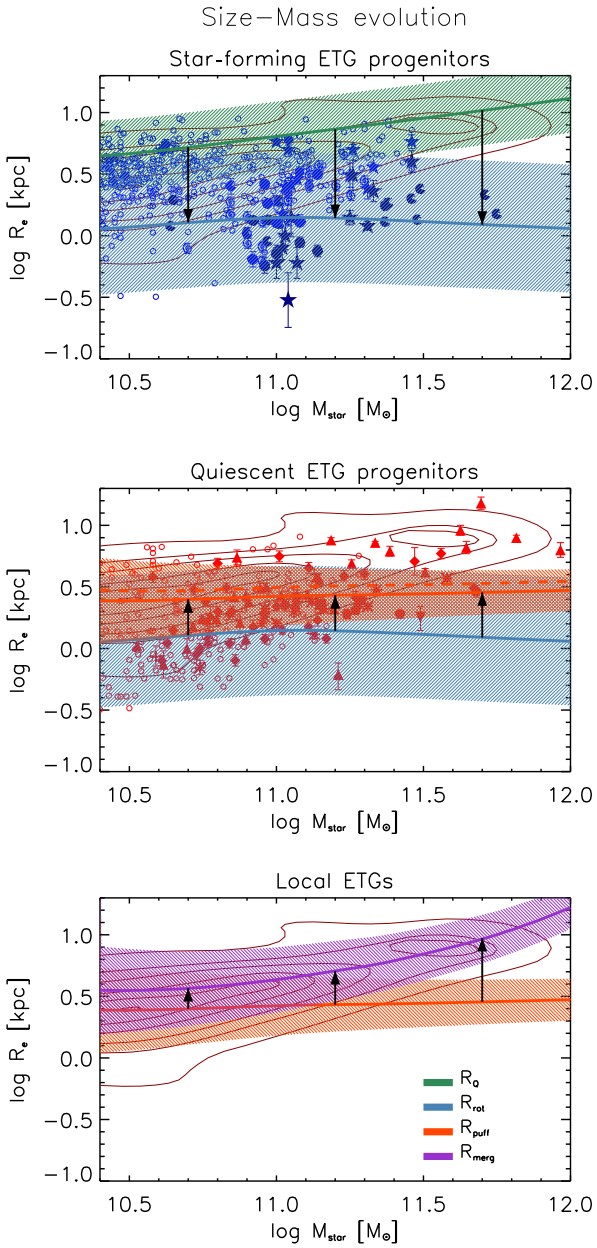

Figure 4.1.3: Size-mass relationship predicted by model for massive ETGs. The symbols refers to high-z observations of DSFGs. Top panel: starforming ETG progenitors; middle panel: quiescent ETG progenitors; bottom panel: local observations of ETGs, with dark red contours coming from the ATLAS^{3D} survey by Cappellari et al. (2013). The green line refers to the fragmentation size R_Q (Eq. 4.4), blue line to centrifugal size $R_{\rm rot}$ of Eq. 4.9, orange line refers to $R_{\rm puff}$ as in Eq. 4.14, magenta line to $R_{\rm merg}$ (Eq. 4.15). Black arrows highlight the evolution from a size to the other. From L18, and references therein.

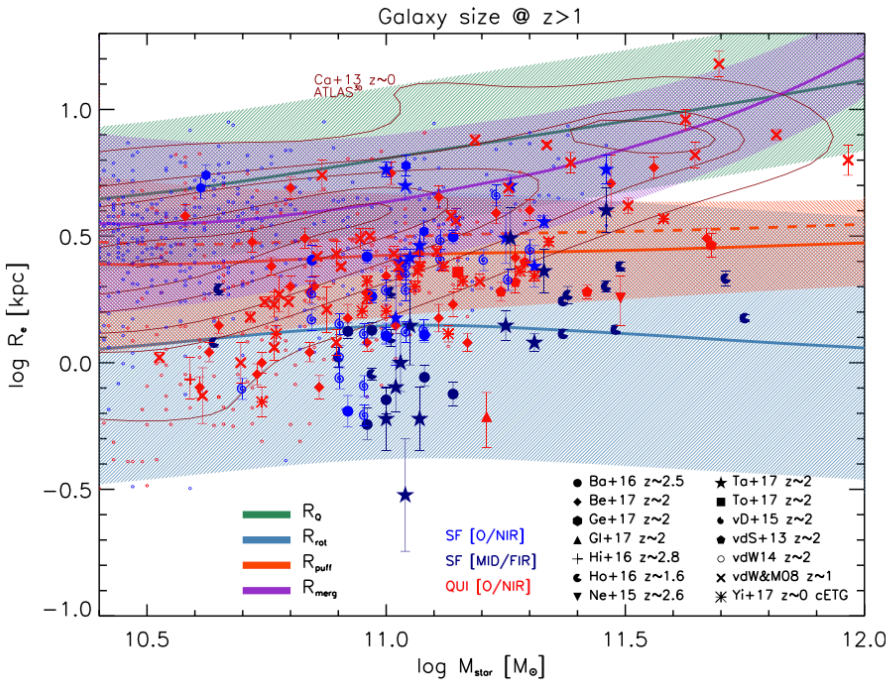

Figure 4.1.4: Composite version of Fig. 4.1.3, with each datapoint reference reported on the bottom right. Red points are for quiescent galaxies, light-blue points refer to star-forming galaxy sizes measured from optical/nearIR observations, dark-blue points to sizes measured from mid-/far-IR observations. From L18.

stellar mass of the system is higher than $10^{12} M_{\odot}$ the AGN is formed, accreting matter at super-Eddington rates, with size and mass even higher than the remaining collapsing material. The radiative feedback wipes out the remaining matter, halting the collapse and the SF inside the galaxy. For stellar mass lower than $\sim 10^{12} M_{\odot}$, the AGN does not form, and the main feedback mechanism comes from supernovae explosions and stellar winds. Since the infalling mass is lower than the previous case, weaker feedbacks are able to wipe out the material and quench the galaxy.

In this phase, there's a change in the typical sizes, since the gravitational potential of the system changes, relaxing toward higher radius. The final size of the system will depend on the ratio between the gas expulsion timescale and the dynamical timescale, a process also called *puffing-up*. In the puff-up scenario, the size of the innermost part of quasars probed with farIR/sub-mm observations are on average smaller than ones with SFR reduced by the feedback mechanisms.

Approximated expression for the final radius $R_{\rm puff}$, related to the initial $R_{\rm in}$, are derived in Ragone-Figueroa and Granato (2011):

$$\begin{aligned} \frac{R_{\rm puff}}{R_{\rm in}} &\sim \left(1 + \frac{\chi f_{\rm out}}{1 - \psi f_{\rm out}}\right) \text{ for } R_{\rm in} \sim 3\,\text{kpc}, \\ \frac{R_{\rm puff}}{R_{\rm in}} &\propto \left(\frac{R_{\rm in}}{2.7\text{kpc}}\right)^{-\varphi} \text{ for } f_{\rm out} \geq 0.4. \end{aligned} \tag{4.14}$$

with $f_{\rm out} \equiv M_{\rm out}/M_{\rm inf}$ being the mass ejected fraction, $\chi \sim 1.1$ and $\varphi \sim 0.7$ for an impulsive ejection, $\chi \sim 0.8$ and $\varphi \sim 0$ for a slow ejection. The retrieved size are once again in accordance with nearIR/optical observations of quiescent galaxies at $z \sim 1 - 2$ (Newman et al., 2015, Belli et al., 2017, Glazebrook et al., 2017, Toft et al., 2017, Hill et al., 2018). Furthermore, these processes should already be present even at higher redshifts, since the relaxation timescales are extremely fast.

4.1.4 Late evolution

In this final stage of evolution of the proto-ETG, the size and mass of the galaxy increase by means of dry mergers. Assuming $r \propto M^k$, with $k = 0.56$ for local ETGs (Lange et al., 2015),

$$\frac{R_{\text{merg}}}{R_{\text{in}}} = \frac{(1+\eta)^2}{1+\eta^{2-k}}, \tag{4.15}$$

with $\eta \equiv M_{\text{acc}}/M_{\text{in}}$. Predicted post dry-mergers sizes are also in accordance with local ETGs observations (Cappellari, 2016).

4.2 Observational evidence and gravitational lensing

According to the model, it is possible to probe the different evolutionary phases of a proto-ETG simply by observing a sample of high-z galaxies at different wavelengths. In fact, different emissions probe different physical components and evolutionary stages in the source. During the initial phases, the central regions of the galaxy are completely (or almost) enshrouded in dust, therefore the bulk of emission comes from far-IR/sub-mm, that is the dust-reprocessed light of newborn stars. At some point, the AGN forms and starts accreting. Its emission is initially heavily obscured by the dusty environments, but towards the final steps of the puffing-up phase, the X-ray emission is powerful enough to escape the dust. The AGN is now detectable in X-rays. At its activity peak, there's a combination of different emissions coming from the X-ray or radio (probing the AGN) and far-IR/sub-mm (mostly probing star formation processes). After the puffing-up phase, an optical QSO is clearly visible, still emitting in X-ray and radio bands, while the sub-mm emission declines as a consequence of quenching, and the galaxy is now visible in the optical and near-IR bands, probing the evolved stellar component. A schematic evolution of far-IR and bolometric X-ray luminosities for two galaxies at $z = 2$ and halo masses $M_H \sim 10^{12} M_\odot$ is reported in Fig. 4.2.1.

Observing these objects during the early stages of evolution yields a strong

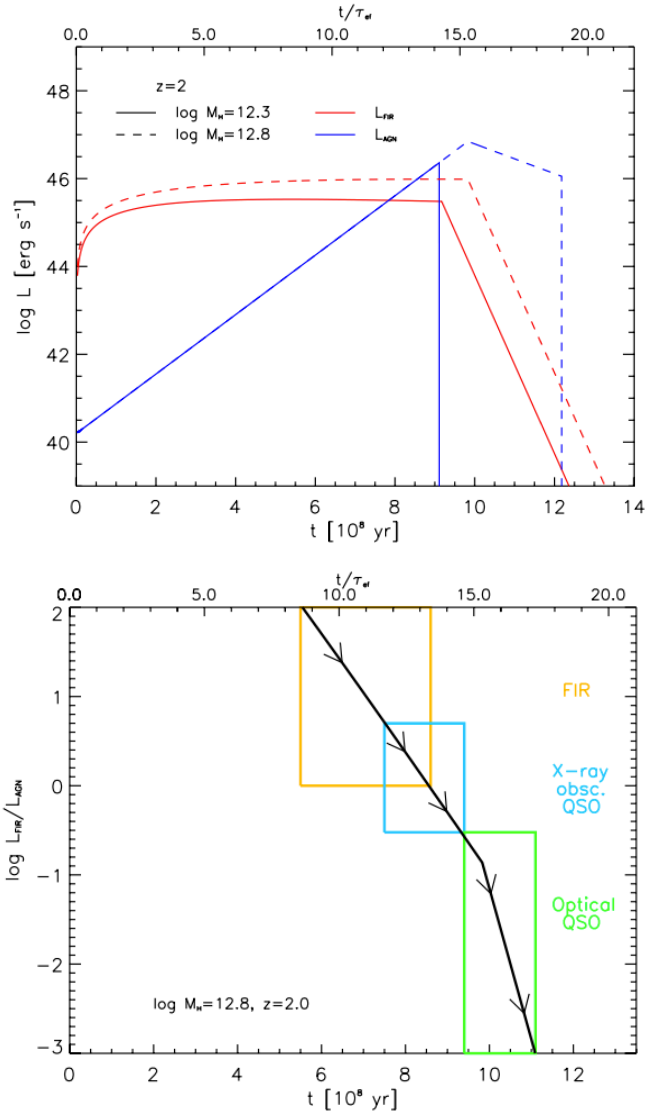

Figure 4.2.1: The different evolutionary phases of the proto-ETG at redshift $z = 2$, highlighting the luminosities evolution. Top panel: red lines are the far-IR/sub-mm luminosity, probing star formation. Blue lines are the bolometric AGN luminosity, probing BH accretion. Dashed lines refers to a halo mass of $M_H = 6 \times 10^{12} M_\odot$, solid lines to a halo mass of $M_H = 2 \times 10^{12} M_\odot$. Bottom panel: the different phases of AGN/galaxy co-evolution as a function of the ratio between the far-IR luminosity and the AGN luminosity. Orange highlights the FIR-bright phase, cyan box the obscured X-ray QSO phase, green the optically bright QSO phase. From Lapi et al. (2014).

far-IR/sub-mm emission, and no emission from X-ray or radio. Observations carried out during the late stages, during or after the puffing-up stage, reveal the optical quasars and the evolved stellar component. In later stages, after dry merging, there's virtually no emission coming from dust or gas. The galaxy is completely quenched, and is a typical ETG observed in the local Universe. Simultaneously observed emission from X-ray to far-IR/sub-mm and radio probes the co-evolutionary stage in the galaxy evolution (blue box in the bottom panel of Fig. 4.2.1). High-resolution observations of these kind of objects are crucial to validate the co-evolutionary scenario. This is the case of two lensed galaxies observed in the H-ATLAS survey (see Sec. 3.1), H-ATLASJ090740.0-004200 and H-ATLASJ091043.1-000322 (Massardi et al., 2018), both showing a clear detection in X-rays co-spatial with the sub-mm emission. I will present the observations and lens modeling of Chandra, HST and ALMA high-spatial resolution data of these two sources in the next section. Other sources such as SDP.81 clearly hint at the presence of an obscured central AGN from radio observations (Mancuso et al., 2017).

Work on Submillimetre Common-User Bolometer Array (SCUBA, Hughes et al., 1998, Holland et al., 1999) detected galaxies led to the definition of the term "sub-mm galaxies", recognizing them as a distinct population rarely seen in the local Universe, but extremely frequent at high-z. This population is responsible for the peak of the SF history in the Universe at redshift $z \sim 2$, also known as the *cosmic noon* (see Madau and Dickinson, 2014). A similar independent analysis performed on BH accretion rate history led to similar results, with a peak between redshifts $z = 1 - 2$, and is reported in Fig 4.2.2. The shapes of the time histories for both distributions, though probing independent samples and populations, are the same. In a major merger scenario, the formation of the central BH is expected as a consequence of merging, while the SF is ongoing, therefore the emission peak of BHAR should be somewhat delayed with respect to the SFR peak. Conversely, in the co-evolution scenario the peaks are coeval in the history of the Universe. This argument is still debated today, and

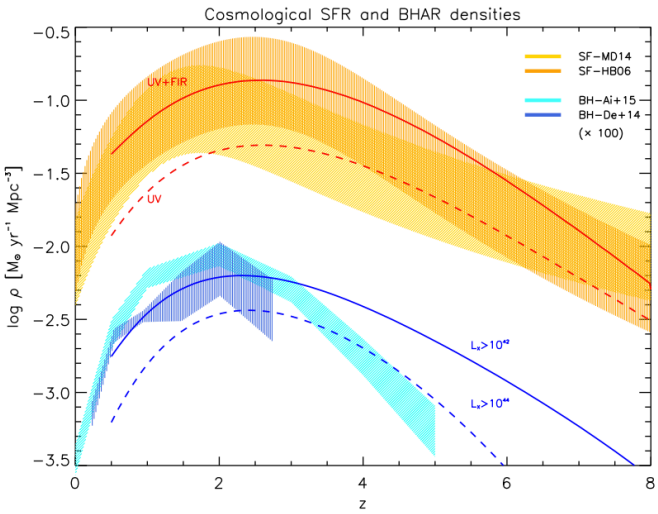

Figure 4.2.2: BH accretion rate density (blue lines) and average SFR (red lines) as a function of redshift. Dashed line is the UV-inferred SFR, solid line the UV+far-IR. The BHAR is multiplied by 100 for illustration clarity. Solid blue line is obtained integrating AGN bolometric luminosity down to $L_X \geq 10^{42}$ erg s^{-1}, dashed line to $L_X \geq 10^{44}$ erg s^{-1}. From Mancuso et al. (2016).

requires more data to be properly addressed.

This remarkable similarity between BHAR measurements and SF is also observed with follow-up observations of galaxies selected in each region of the M_*-SFR plane, where starforming galaxy are seen to lie along the so-called *main sequence* of starforming galaxy. Rodighiero et al. (2015) selected a number of DSFGs at $1.5 < z < 2.5$ in the COSMOS field, combining far-IR photometry with X-ray stacking. They found that the underlying relation between stellar masses and SFR and between stellar masses and BHAR is similar for starburst objects (a factor >4 over the main sequence), starforming objects (exactly on the main sequence), and passive objects (below the main sequence). There's a relation between stellar component, starforming component and the ratio of BH/AGN luminosities during every phase of these objects (Fig. 4.2.3). Delvecchio et al. (2015) extended this analysis, and found that the relation is still

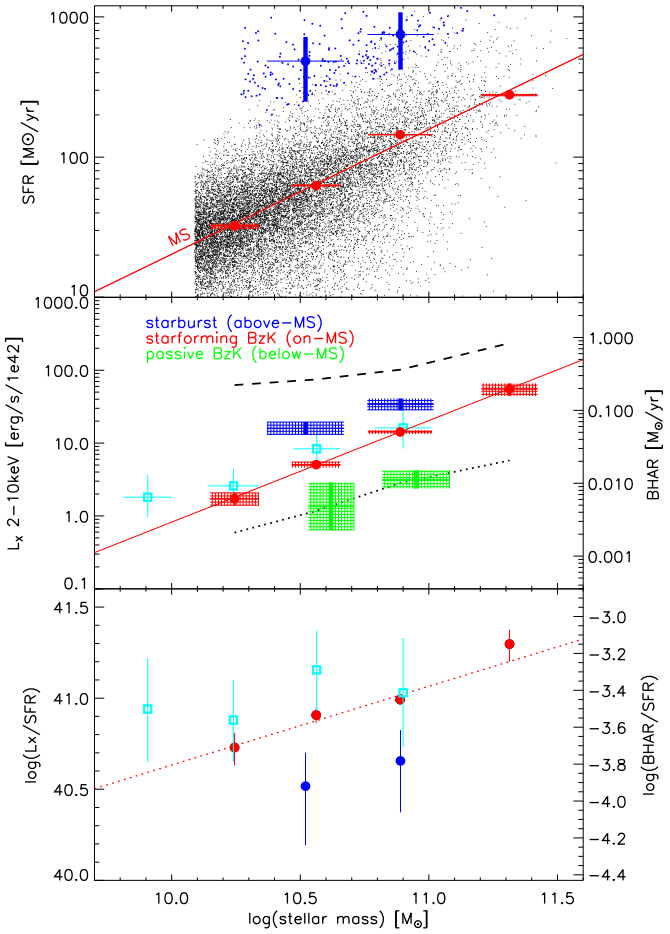

Figure 4.2.3: Main sequence relations for BHAR and SF. Top panel is the mass-SFR relation, red circles are the SFR from far-IR+UV analysis, black dots UV-inferred SFR, black line the MS relation, blue points the average SFR for the starburst sample in two mass bins. Middle panel, BHAR at $1.5 < z < 2.5$ obtained from X-ray stacking, for starburst (blue), MS-galaxies (red) and quiescent sources (green), red line is the fit for the MS sample. Bottom panel: the ratio between bolometric X-ray luminosity L_X and SFR for starburst (blue) and MS galaxies (red), dotted red line is the linear fit. From Rodighiero et al. (2015).

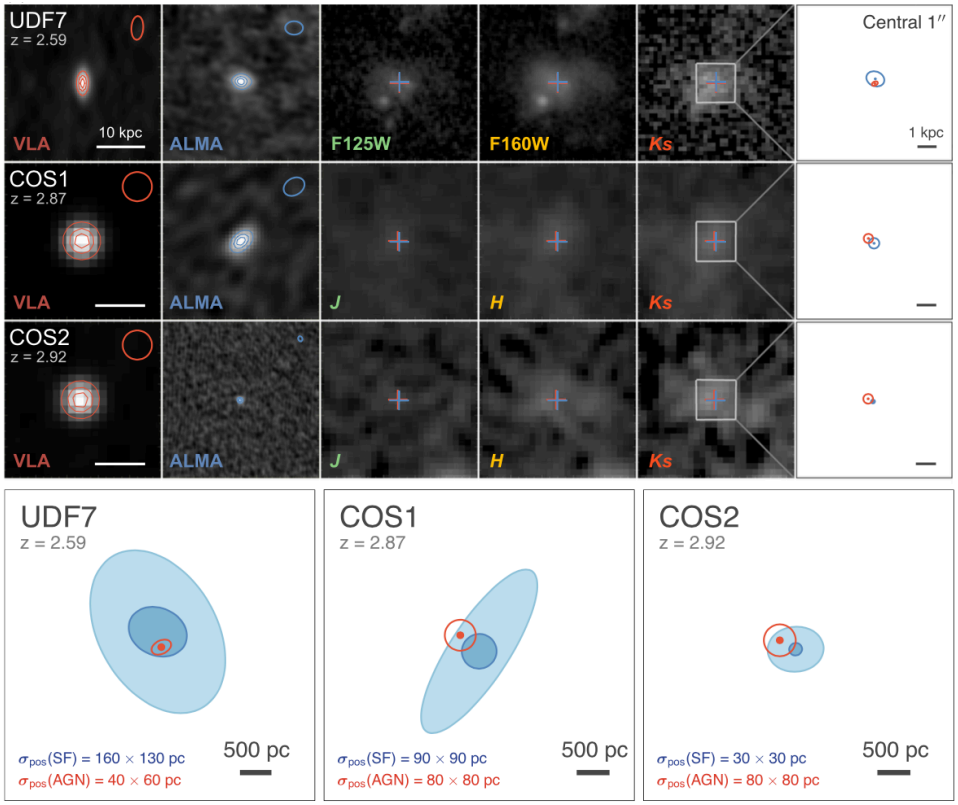

Figure 4.2.4: Multiwavelength imaging of three radio-dominated AGN. Top panels: from left to right, cutouts are from VLA, ALMA, 1.25 μmm 1.6 μm, 2.15 μm observations. The rightmost panel is a diagram of the central region, within 1″, red contours AGN 3σ position inferred from VLA, blue contours 3σ star-forming region inferred from ALMA. VLA traces directly the AGN, ALMA the star formation, the near-IR data the stellar distribution. Bottom panels: a close-up of the central 5 kpc of the three galaxies in the sample. There's a clear cospatiality between the star forming regions and the AGN. From Rujopakarn et al. (2018).

valid at different redshifts.

In addition to multiwavelength studies of these objects, another tool to investigate the co-evolution is with high-resolution imaging, something that is now possible to achieve with to ALMA. Tadaki et al. (2017) observed a CO disk in a $z \sim 2.5$ galaxy within 1 kpc of the dust peak. Hodge et al. (2016) showed how in a sample of 8 ALMA observed DSFGs the ALMA component is always central with respect to emission in other bands (i.e. HST); furthermore, the cumulative flux distribution as a function of radius (Fig. 6 of the paper) shows how the sub-mm component is enclosed within a few kpc from the core, while the stellar component is more relaxed and extended. Rujopakarn et al. (2018) combined VLA and ALMA high-resolution observations of three DSFGs, clearly showing a cospatiality between the AGN and the SF components withing 1 kpc (Fig. 4.2.4). Nowadays, ALMA is able to perform these kind of analysis at resolution of ~ 30 mas, i.e. ~ 230 pc at $z = 3$.

4.3 Buried AGN in two lensed galaxies

As shown in the previous Chapters, there are different ways to validate the co-evolution scenario. Probing the highest angular scales in high-z objects experiencing both intense star formation and AGN activity is crucial to distinguish between different galaxy evolution models. In this sense, the magnification and increase in angular resolution generated by a gravitational lens is ideal for these kinds of studies. A gravitational lens allows us to distinguish details otherwise hardly accessible, as long as some lens modeling and source reconstruction techniques are involved.

That's the case for H-ATLASJ090740.0-004200, from now on SDP.9, and H-ATLASJ091043.1-000322, from now on SDP.11, as presented in Massardi et al. (2018). The sources were discovered in the first 16 deg^2 of the H-ATLAS survey (see Sec. 3.1), and were confirmed as strong lenses with both near-IR HST/WFC3 observations (Dye et al., 2014, Negrello et al., 2014, for lens modeling) and sub-mm (Bussmann et al., 2013). CO lines detection with the

Z-spec spectrometer (Lupu et al., 2012) put the sources at redshift $z = 1.577 \pm 0.008$ (SDP.9) and $z = 1.786 \pm 0.005$ (SDP11). The lenses are two massive elliptical galaxies at redshift $z = 0.6129$ (SDP.9) and $z = 0.7932$ (SDP11).

Between January and March 2015, Cycle 16 Chandra ACIS-S observations (P.I. Massardi) were executed. The sources were selected thanks to their mid-IR excess in the spectral energy distribution. (see Fig. 6 of Negrello et al., 2014), suggesting upper-limit AGN bolometric luminiosities of $L_{\rm AGN} \sim 5.1 \times 10^{45}$ erg s^{-1} and $L_{\rm AGN} \sim 4.3 \times 10^{46}$ erg s^{-1} respectively for SDP.9 and SDP.11.

Despite the relatively low (for lensing) angular resolution of 0.5 arcsec, high-energy Chandra photons in the range 0.5-7 kev are detected (14 each), spatially distributed along the image plane matching the sub-mm emission rather than the near-IR. This is shown in Fig. 4.3.1, where the ALMA 1.3 mm observations come from two publicly available different projects, ID:2015.1.00415 PI: Wong for SDP.9, 2015.1.01362 PI: Gordon for SDP.11, both observed in Cycle 3. I performed lens modeling and source reconstruction of the former ALMA data, and I will present the results in the next Section.

Both X-ray images clearly indicate the presence of highly obscured nuclear activity. For SDP.9, the observed 2-10 keV apparent flux is $\sim 3.6 \times 10^{-15}$ erg cm^{-2} s^{-1}, and the absorption corrected X-ray luminosity is 3.7×10^{43} erg s^{-1}, decreasing to 5.9×10^{42} erg s^{-1} once corrected for magnification. The emission spectrum of SDP.9 is fitted with a photon-index power-law of index $\Gamma = 1.1 \pm 1.0$, and a column density of $\sim 5.2 \times 10^{22}$ cm^{-2} if a $\Gamma = 1.8$ is assumed as typical for AGN and quasars. For SDP.11, 2-10 keV apparent flux is $\sim 1.2 \times 10^{-14}$ erg cm^{-2} s^{-1}, absorption corrected X-ray luminosity 1.2×10^{44} erg s^{-1}, lowered to 1.5×10^{43} erg s^{-1} once magnification is accounted. The spectral index Γ is 1.0 ± 0.9, and once again the column density for a $\Gamma = 1.8$ power-law is $\sim 3.2 \times 10^{22}$ cm^{-2}.

Estimated contribution from star-formation processes to the 2-10 keV

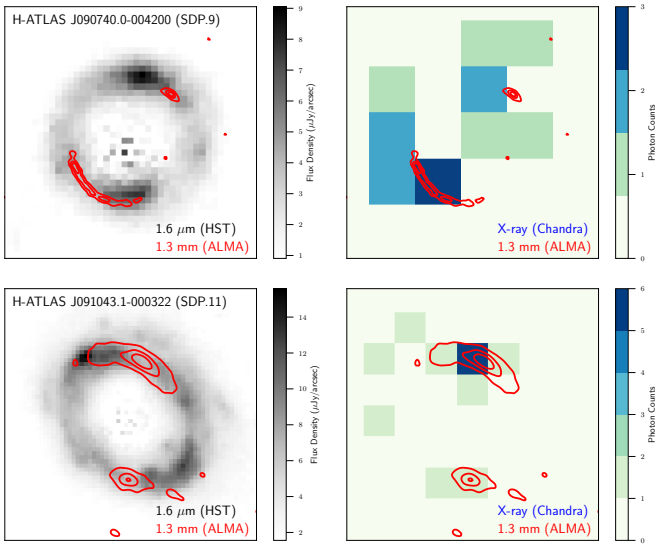

Figure 4.3.1: Multiwavelength observations of the H-ATLAS sources SDP.9 (box size 2.7"×2.7") and SDP.11 (4"×4"). Left panels: HST/WFC3 imaging at 1.6 μm, with superimposed ALMA 1.3 mm contours. Right panels: Chandra ACIS 0.5-7 kev images, with superimposed ALMA 1.3 mm contours. In both case, the cospatiality between the ALMA and Chandra peak is clearly visibile directly in the image plane. This is later confirmed in the reconstructed source.

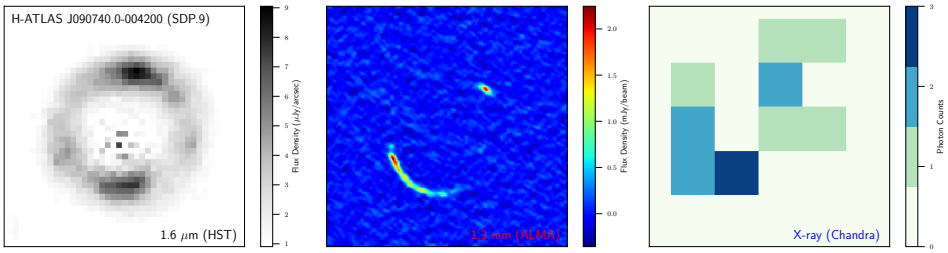

Figure 4.4.1: Image planes of SDP.9. Left panel: HST/WFC3 imaging at 1.6 μm. Middle panel: ALMA 1.3 mm cleaned image. Right panel: Chandra ACIS 0.5-7 keV image. Each panel is centered in the same position and have the same scale.

luminosities, obtained from the SED fitting retrieved SFRs applied to the Ranalli et al. 2003 relation, leads to values of 1.9×10^{42} erg s^{-1} for SDP.9 and 3.3×10^{42} erg s^{-1} for SDP.11, that is a factor 3 to 4.5 lower than the X-ray intrinsic luminosities.

These X-ray emissions indicate nuclear activity due to gravitational accretion simultaneous to heavily obscured star formation. The coincidence between the sub-mm and the X-ray peaks in the image plane is a sign of cospatiality between the two regions in the source plane. In the next Section, I will show the correctness of this scenario with lens modeling and source reconstruction of the available data for SDP.9.

4.4 SDP.9 LENS MODELING

In Massardi et al. (2018) I modelled HST/WFC3 1.6 μm, ALMA 1.3 mm and Chandra 2-10 kev emissions (image planes showed in Fig. 4.4.1). Low-angular resolution and scarcity of photons for the latter only allows me to identify the position of the reconstructed emission peak, rather than the full morphology. Regarding ALMA data, as showed in the literature (see Hezaveh et al., 2016, Dye et al., 2018), in order to perform lens modeling correctly, a proper evaluation of the visibility associated noise is mandatory. This is achieved by subtracting

Table 4.4.1: Results of the modelling for the HST 1.6 μm and ALMA 1.3 mm data for SDP.9. The parameters of the model, for which a SIE profile mass distribution is assumed, are: the normalization of the profile, expressed in terms of the Einstein radius ($\theta_{\rm E}$); the rotation angle ($\theta_{\rm L}$; measured counter-clockwise from West); the minor-to-major axis ratio ($q_{\rm L}$); the position of the lens centroid from the centre of the images in Fig. 4.4.1.

	$\theta_{\rm E}$ (arcsec)	$\theta_{\rm L}$ ($^\circ$)	$q_{\rm L}$	$\Delta x_{\rm L}$ (arcsec)	$\Delta y_{\rm L}$ (arcsec)
HST 1.6 μm	0.66$\pm$0.04	142.51$\pm$7.51	0.77$\pm$0.02	-0.09$\pm$0.02	-0.04$\pm$0.05
ALMA 1.3 mm	0.65$\pm$0.04	143.19$\pm$9.09	0.77$\pm$0.04	-0.10$\pm$0.03	+0.01$\pm$0.03

subsequent visibilities along a single baseline in a 30 seconds time bin, and taking the rms of the residuals as the noise variance for all the baseline associated visibilities within the same time bin. In order to reduce computational effort, a time averaging of the visibilities in the same 30 second bin is employed, slightly reducing the final total angular resolution. Lens modeling and source reconstruction is then performed on this visibility data set. I reported in Chapter 2 the methodology, and in Chapter 3 some implementation technicalities are reported that are also adopted here.

Lens parameter searches have been performed on both HST and ALMA data. The lens mass distribution is assumed to be described by a SIE profile, thus the total number of parameter is 5: the Einstein radius $\theta_{\rm E}$, related to the lens mass; the position angle $\theta_{\rm L}$ measured counter-clockwise from East; the lens ellipticity $q_{\rm L}$; the position of the lens centroid with respect to the image center, $\Delta x_{\rm L}$ and $\Delta y_{\rm L}$. The results are reported in Tab. 4.4.1. There's an excellent agreement in the retrieved parameters for both data sets, and the same agreement is found with lens modeling of the SMA data for the same source I showed in the previous Chapter (see Tab. 3.4.1).

The retrieved magnification factors μ, depending on the SNR of the reconstructed source (from 3σ to 5σ) are $\mu_{_{1.6\,\mu{\rm m}}} = 7.80$ to 8.33 for the HST data,

Table 4.4.2: Source properties. Magnifications, $\mu_{3\sigma}$ and $\mu_{5\sigma}$, are evaluated as the ratio between the total flux density of the region in the SP with SNR$\geq$ 3 and SNR$\geq$ 5, respectively, and the total flux density of the corresponding region in the IP. $A_{\mathrm{dust},3\sigma}$ and $A_{\mathrm{dust},5\sigma}$ are the areas of the regions with SNR$\geq$ 3 and SNR$\geq$ 5 in the source plane, while $r_{\mathrm{eff},3\sigma}$ and $r_{\mathrm{eff},5\sigma}$, are the radius of a circle with area equal to $A_{3\sigma}$ and $A_{5\sigma}$, respectively.

	$\mu_{3\sigma}$	$\mu_{5\sigma}$	$A_{3\sigma}$ (kpc^2)	$A_{5\sigma}$ (kpc^2)	$r_{\mathrm{eff},3\sigma}$ (kpc)	$r_{\mathrm{eff},5\sigma}$ (kpc)
HST 1.6 μm	7.80$\pm$0.44	8.32$\pm$0.49	20.43$\pm$1.80	11.45$\pm$1.60	2.550$\pm$0.117	1.909$\pm$0.144
ALMA 1.3 mm	17.39$\pm$3.86	18.73$\pm$4.43	0.82$\pm$0.34	0.44$\pm$0.16	0.510$\pm$0.098	0.375$\pm$0.064

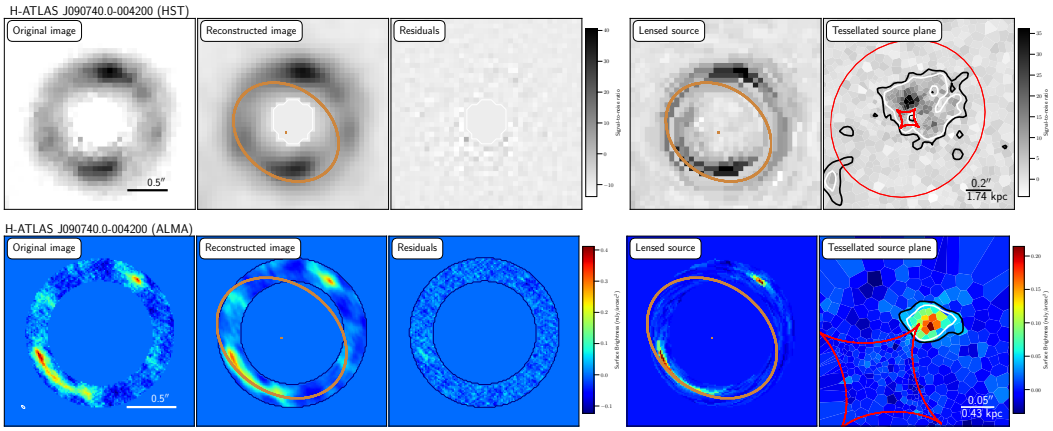

Figure 4.4.2: Source planes of SDP.9. Upper panel HST/WFC3, lower panel ALMA. From left to right: input image (generated with a natural weighting scheme for ALMA); minimum χ^2 image; residuals, obtained by subtracting the first two panel for HST, and subtracting the observed visibilities with the model ones and then transforming back to the real space for ALMA; image obtained by lensing the reconstructed source plane using the best-fitting lens model; the reconstructed background source with contours at 3σ (black) and 5σ (white). The critical lines and caustics are shown in brown (in the second and fourth panels from left) and in red (in the right panel), respectively. The white ellipse in the bottom left corner of the leftmost panel of the ALMA set is the image synthesized beam. Adapted from Massardi et al. (2018).

and $\mu_{1.3\,\mathrm{mm}} = 17.39$ to 18.73 for the ALMA data. The discrepancy is mainly due to the closer position to the lens caustic (in red) of the ALMA emission with respect to the more extended HST light. $\mu_{1.6\,\mu\mathrm{m}}$ is higher than the value of 6.3 reported in Dye et al. (2014), though consistent within 2.5σ. In that case, the lens was modelled with a power-law profile. $\mu_{1.3\mathrm{mm}}$ is almost twice the value of $\mu_{880\,\mu\mathrm{m}}$ reported in Bussmann et al. (2013), and ~ 3 times the value presented in Enia et al. (2018) and in Chapter 3. This is expected, since the ALMA observations are at higher resolution than the SMA observations. The reconstructed source is therefore extremely compact and closer to the caustic than the SMA signal.

This result clearly indicates the need of a degree of caution whenever de-lensing the observed flux density with a lens-modeling retrieved magnification, even in the sub-mm domain. In this case, the best strategy is to demagnify the observed fluxes with the proper μ, and then perform SED fitting. I adopted this strategy for this work, demagnifying the PACS/SPIRE fluxes with the μ_{880} reported in Chapter 3, and the ALMA flux with the $\mu_{1.3\,\mathrm{mm}}$ previously reported. Then I performed SED fitting with a modified blackbody spectrum with dust emissivity index $\beta = 1.5$, using the Kennicutt and Evans (2012) relation to derive the SFR from the integrated $8 - 1000$ μm infrared luminosity, which assumes a Kroupa (2001) IMF.

The best-fit results are $T_{\mathrm{dust}} = 42.5 \pm 0.1$ K, $\log L_{\mathrm{IR}} = 12.84 \pm 0.06\, L_{\odot}$ and a SFR of $900 \pm 100\, M_{\odot}\ \mathrm{yr}^{-1}$ for the SNR at 3σ in the source plane, $T_{\mathrm{dust}} = 42.7 \pm 0.1$ K, $\log L_{\mathrm{IR}} = 12.79 \pm 0.04\, L_{\odot}$ and a SFR of $810 \pm 80\, M_{\odot}\ \mathrm{yr}^{-1}$ for the SNR at 5σ in the source plane, slightly lower than the result reported in Chapter 3 for the same source, based on Herschel/SPIRE, Herschel/PACS and SMA data alone.

The reconstructed source morphologies obviously follow the different physical mechanisms that generate the emission (Fig. 4.4.2). The near-IR emission directly traces the starlight that's able to escape the dusty environment, that is the starlight coming from the outer part of the system. It is fairly extended, with a surface area of ~ 11 to 20 kpc^2 (black and white contours, corresponding to 3σ and 5σ), leading to an effective radius of ~ 1.90 to 2.55 kpc. The sub-mm signal is

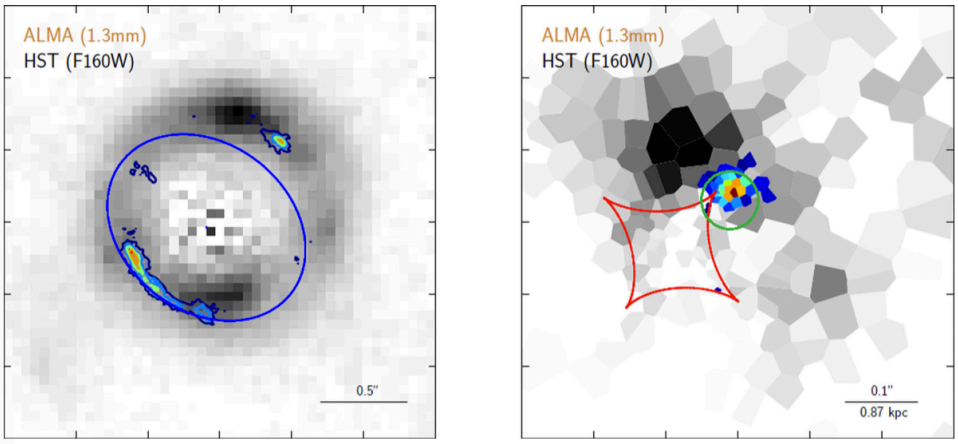

Figure 4.4.3: *Left panel*: HST/WFC3 image plane (grey scale) with superimposed ALMA 1.3 mm contours. The critical line is plotted in blue. *Right panel*: the reconstructed source plane on Voronoi tesserae. The green circle highlights the position of the reconstructed Chandra emission peak within 5σ, tracer of the nuclear activity. There is a clear coincidence with the ALMA signal, tracer of star formation. The caustic is plotted in red. Angular and physical scale are in black in the bottom right of each panel. From Massardi et al. (2018).

the dust reprocessed light of the UV-radiation fields of newborn stars instead, and so it highlights the star forming regions, in the innermost parts of the galaxy. These regions are more compact with a surface area of ~ 0.4 to $0.8\,\mathrm{kpc}^2$, corresponding to an effective radius of ~ 350 to 500 pc (see Tab. 4.4.2). The distance between the two emission peaks is ~ 0.9 kpc. Inside this reconstructed star forming regions, I obtain a $\Sigma_{\mathrm{SFR},3\sigma} \sim 1100 \pm 450\,\mathrm{M}_\odot\,\mathrm{yr}^{-1}\,\mathrm{kpc}^{-2}$ and $\Sigma_{\mathrm{SFR},5\sigma} \sim 1870 \pm 670\,\mathrm{M}_\odot\,\mathrm{yr}^{-1}\,\mathrm{kpc}^{-2}$, appreciably higher than the Eddington limit of $10^3\,\mathrm{M}_\odot\,\mathrm{yr}^{-1}\,\mathrm{kpc}^{-2}$ in a radiation pressure supported starburst galaxy, at variance with the results presented in Chapter 3 (a order of magnitude lower), mainly due to the small size and compactness of the region.

In order to investigate the co-evolution scenario, I performed a first-order lens modeling on the available Chandra 2-10 keV data. I was able to identify the reconstructed position of the peak signal, that is cospatial with the sub-mm

emission. The 5σ position is highlighted with the green circle in Fig. 4.4.3. From this analysis, star formation and AGN activity coexist within an unresolved region of radius ~ 375 pc. Any further analysis requires higher-resolution data.

4.5 Conclusions

In the past decades, it has been extensively confirmed by a number of different observations that there exists a co-evolution between the star formation and the AGN components in the innermost part of DSFGs. So far, this scenario was investigated only with detectable AGN, with X-ray luminosities high enough to be observed at $z > 1$, corresponding to galactic ages of 10^9 yr, in a relatively late stage. Strong lensing allows the observer to observe at earlier evolutionary stages, approximately at the peak of SF and AGN activity (Fig. 4.2.1). The galaxies presented in this Chapter, H-ATLAS J090740.0-004200 and H-ATLAS J091043.1-000322, fall into this category. These galaxies feature intrinsic SFR $\sim 10^2$ $M_\odot$ yr^{-1}, with stellar masses (coming from SED fitting of the near-IR available data, see Negrello et al. (2014)) of $M_* \sim 9.1 \times 10^{10}$ (SDP.9, opportunely demagnified with $\mu_{\rm HST}$) and $M_*/\mu \sim 18.7 \times 10^{11}$ (SDP.11). This values imply a young age $\tau_{\rm age} \sim 10^8$ yr, and place the sources $\approx 0.4 - 0.6$ dex over the main-sequence in the SFR-M_* diagram (Rodighiero et al., 2011, 2014). These galaxies are younger than MS galaxies with the same SFR, making them richer in gas, with masses $M_{\rm gas} \geq 10^{10}$ $M_\odot$, leading to a lower limit value of the depletion time $\tau_{\rm depl} \geq 10^7$ yr, with a more realistic value of $\tau_{\rm depl} \geq 10^7$ yr when the objects will move from the starbursts region to the MS of starforming galaxies or below it.

As for the AGN, the intrinsic X-ray luminosities are $L_{\rm X} \leq 10^{43}$ erg s^{-1}, 3 to 4.5 higher than the star-formation expected $L_{\rm X}$. $L_{\rm AGN}$ is of the order of 10^{44} erg s^{-1}, corresponding to a BH mass of $M_{\rm BH} \sim 10^6$ $M_\odot$ if a Eddington ratio of ~ 1 is assumed (Alexander et al., 2008). These galaxies lies slightly below the MS of AGN (Rybak et al., 2015). The final BH relic mass, evaluated from the ratio $M_{\rm BH}/M_* \sim 10^{-3}$, is expected to be $M_{\rm BH} \geq 10^8$ $M_\odot$, with associated

bolometric luminosity $L_{\rm AGN} \sim 10^{46}$ erg s^{-1}, as expected by the evolutionary model to the far-IR luminosity of the star formation. At that point, the AGN feedback should be enough to quench the SF processes, terminating the BH accretion, and moving the galaxy to the passive stage of its evolution.

Lens modelling and source reconstruction results clearly supports a cospatiality between the two components, within a radius of ~ 375 pc, a compact region with respect to the more diffuse near-IR emission ~ 2 kpc. Future multiwavelength observations of strongly-lensed DSFGs known to host a buried AGN will create a reliable sample, able to properly address the co-evolutionary scenario thanks to the angular resolutions otherwise hardly accessible with present-day instrumentation.

5

The molecular gas content in high-z starbursts

One of the key results obtained in the past two decades of studies of galaxy formation and evolution, mainly thanks to observations coming from the Herschel Space Observatory, is the detection of a natural correlation for the bulk of starforming galaxies between the stellar masses (M_*) and the star formation rates (SFR), the so called Main Sequence (MS hereafter, Rodighiero et al., 2011, see Fig. 5.0.1). In a M_*-SFR plot, there are three distinct regions: the MS, that is a tight correlation between the two quantities; the starburst (SB) region, with enhanced values of SFRs; the passive region, where star formation has been quenched and the galaxies evolve passively. This is usually explained by assuming that starforming galaxies spend most of their life in a (quasi) steady state of

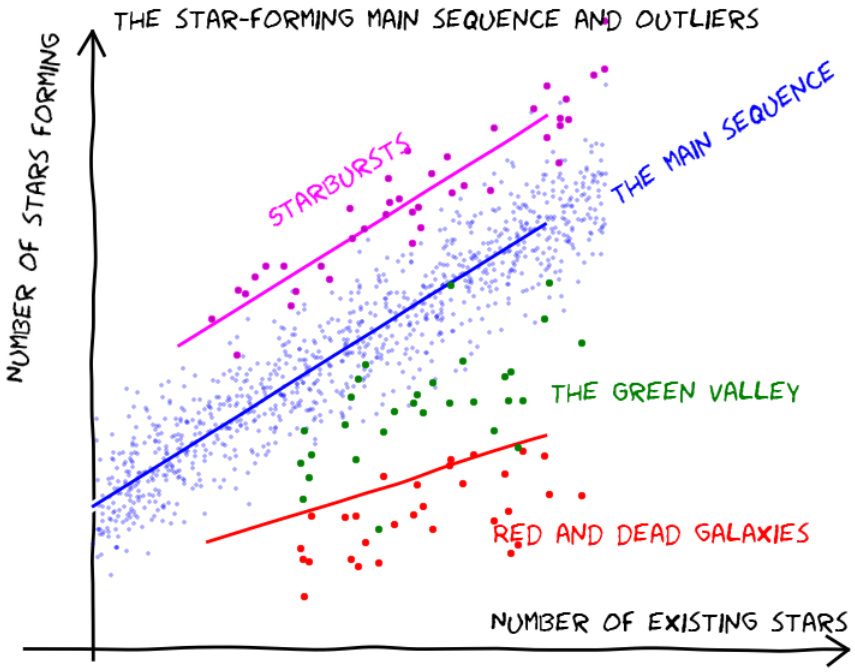

Figure 5.0.1: Cartoon rendition of a typical M_*-SFR plot of starforming galaxies. Blue points and line represents the Main Sequence; magenta points and line the starbursts outliers, usually identified with a fine line of factor 4 above the MS. Passive, quenched massive galaxies are the red points and line (*red and dead*). The fringe region between MS and the red and dead region is usually called *the green valley*. From the CANDELS collaboration (URL: http://candels-collaboration.blogspot.com/2013/02/star-formation-in-mountains.html)

secular growth, while stochastic episodes (i.e. gas inflow, mergers) trigger short-lived and intense starburst episodes. Similarly, two different ways of Black Hole (BH) accretion seem to hold: secular processes that dominate the growth of intermediate-low luminosity BHs (through continuous gas refuelling, Rodighiero et al., 2015), and a different growth history strictly connected to the starburst activity in off-MS star-forming galaxies experienced by the most luminous population of AGN. These objects show indications of enhanced AGN activity indeed: a larger average X-ray luminosities (Rodighiero et al., 2015) and an AGN fraction among SB that is high both in the local universe (up to 50 - 80% of local starbursts host an AGN, Alexander and Hickox, 2012) and at high-z, where nearly all of the extreme SBs host heavily obscured AGN (Massardi et al., 2018, Rodighiero et al., 2011). Moreover, AGN host galaxies on the MS are only 10% (see e.g. Kashino et al., 2017). This implies that the AGN duty cycle is higher above the MS (and the Black Hole accretion rate, hereafter BHAR, more efficient).

Many observational efforts have been recently devoted to understand what triggers the fast gas consumption rate in these spectacular sources (Silverman et al., 2015). Mergers are often invoked as the more likely mechanism (but it is not clear if this is sufficient to explain the enhanced star formation efficiencies of SBs compared to normal galaxies, Silverman et al. 2018 in prep.). It is tempting to ask if the merger mechanism enhancing SFR in many SBs could be responsible also for the AGN ignition (as classic paradigmatic simulations suggest, e.g. Di Matteo et al., 2005, Capelo et al., 2015, Steinborn et al., 2018). This scenario is still quite debated (e.g. Mancuso et al., 2016, and references therein). However, even if mergers are generally not considered as the main driver of BH activation, the starburst population might represent the most likely place to look for such kinds of causal effects.

Simulations and observations further suggest that the BHAR is associated with feedback effects, such as powerful stellar winds and AGN driven outflows that have the potential to deplete the gas content of the hosts and then quench their SFR (see Lapi et al., 2018, , or Chaper 4 of this Thesis), up to their final

evolution into red and dead galaxies.

Here by using ALMA dust continuum measurements, the molecular gas properties of a SB sample in COSMOS at the peak of cosmic SFR and BHAR densities, $1.5 < z < 2.5$, is investigated.

The ultimate aim is to compare the gas properties of the AGN dominated SBs, with those of the non-AGN SB population, to infer if there is a significant difference in their gas content and optical morphologies. I will interpret eventual systematics as imprints of feedback induced by major mergers (if any).

This Chapter is based on the work presented in Rodighiero, Enia et. al, in prep.

5.1 The sample

The sample is composed of extremely efficient DSFGs at the peak of cosmic SFR density $1.5 < z < 2.5$, selected from the *Herschel* far-infrared catalog presented in Delhaize et al. (2017), but see also Delvecchio et al. (2015, 2017). Source identification, multiwavelength photometry, stellar masses and redshifts (photometric and/or spectroscopic) are originally from the COSMOS2015 sample (Laigle et al., 2016).

Starbursts (SBs) are selected to have a SFR well elevated above the Main Sequence at $z = 2$, at least a factor 4 in our case (as in Rodighiero et al., 2011, see next Section for a detailed description of the SFR computation).

Out of 1790 *Herschel* detected sources in this redshift bin, we identified a starting sample of 164 SBs (see Figure 5.1.1). The analysis performed here is limited to galaxies with stellar masses greater than $10^{10} M_{\odot}$ (to ensure an unbiased, mass complete selection, see Laigle et al., 2016), reducing the SB sample to 152 objects.

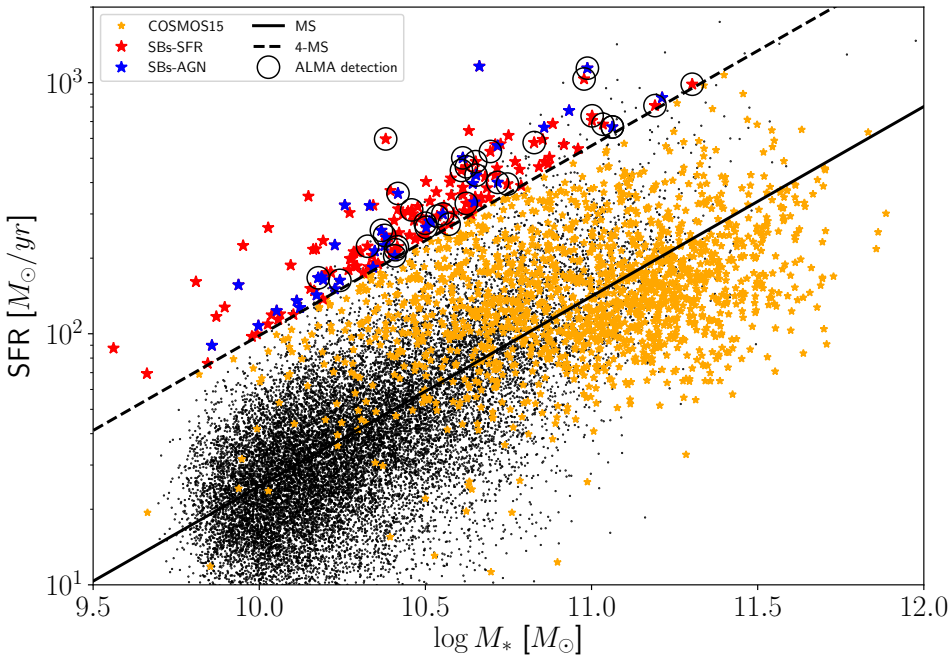

Figure 5.1.1: Sample selection in the COSMOS field at $1.5 < z < 2.5$, in the SFR-M_* plane. Orange stars mark the original *Herschel* sample (Delvecchio et al., 2017). Red and blue stars highlight the position of starbursts, selected to lie a factor four above the MS at $z = 2$. The sources with an ALMA detection are indicated with black open circles. For reference, I also include a population of star-forming BzK as black dots (from the GOODS and COSMOS fields, Daddi et al., 2007)

5.2 SED fitting and AGN classification

The multiwavelength SEDs of the SB sources are fitted in order to derive their physical properties, and to disentangle the potential AGN emission from that related to the host-galaxy. SED-fitting is performed both with *M*AGPHYS code (da Cunha et al., 2008) and the three-component SED-fitting code SED3FIT by Berta et al. (2013), which accounts for an additional AGN component.

The *M*AGPHYS code is designed to reproduce a variety of galaxy SEDs, from weakly star-forming to starbursting galaxies, over a wide redshift range. This code relies on a condition of energy balance between the dust-absorbed stellar continuum and the reprocessed dust emission at infrared wavelengths. This recipe ensures that optical and infrared emission originating from star formation are linked in a self-consistent manner, but does not account for a possible AGN emission components. The three-component SED-fitting code presented by Berta et al. (2013) combines the emission from stars, dust heated by star formation, and a possible AGN dusty torus component from the library of Feltre et al. (2012) (see also Fritz et al., 2006). This approach results in a simultaneous three-component fit. For each best-fit parameter, the code provides a corresponding probability distribution function (PDF), which enables the user to obtain reliable confidence ranges for parameter estimates. Each observed SED is decomposed by using the best available redshift (either spectroscopic or photometric) as input, in order to derive integrated galaxy properties, such as SFR and M_*, for each individual source. The SFR is derived from the total IR (8-1000 μm) luminosity taken from the best-fit galaxy SED (i.e. corrected for a possible AGN emission), assuming a Kennicutt (1998) conversion factor scaled to a Chabrier (2003) IMF. In order to quantify the relative incidence of a possible AGN component, the fit has been performed on each individual SED, both with the three component SED3FIT approach and the *M*AGPHYS code. The fit obtained with the AGN is preferred if the reduced χ^2 value of the best fit is significantly (at $\geq$99% confidence level, on the basis of a Fisher test) smaller than that obtained from the fit without the AGN; see Delvecchio et al. (2014) for

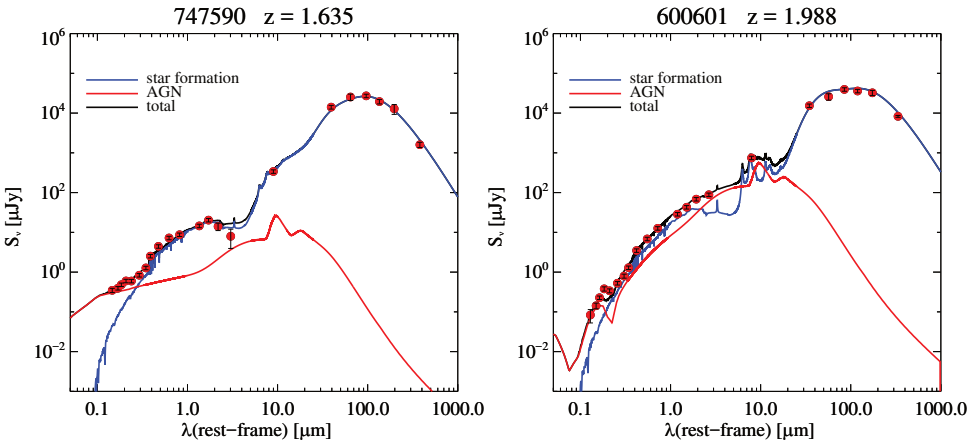

Figure 5.2.1: Two examples of best-fit SEDs of starburst dominated by SFR processes (upper panel) and by a dusty AGN (lower panel). Coloured lines represent the corresponding best-fit templates of AGN (red), galaxy star formation (blue), and the sum of the two (black).

details. From this analysis, 35 out of 152 starbursts (about 23%) show a $\geq$99% significant AGN component in their best fit (see Figure 5.2.1 for some examples of the SED fitting results). In the following, I will refer to these two classes as AGN dominated SBs (SBs-AGN) and SFR dominated SBs (SBs-SFR), respectively.

Out of 152 SBs in the starting sample, only eight have been detected as X-ray AGN (Laigle et al., 2016), six of which are identified by the AGN classification (i.e. 75%). This check ensures recovering the bulk of the classical X-ray/AGN selection, extending the sample to include also the most obscured active sources, that reveal themselves at mid-IR wavelengths (e.g. Bongiorno et al., 2012, Gruppioni et al., 2016).

5.3 Morphological analysis

A visual inspection on the COSMOS/HST ACS *i*-band images of all the SBs (corresponding to their UV-restframe emission) has been performed. This

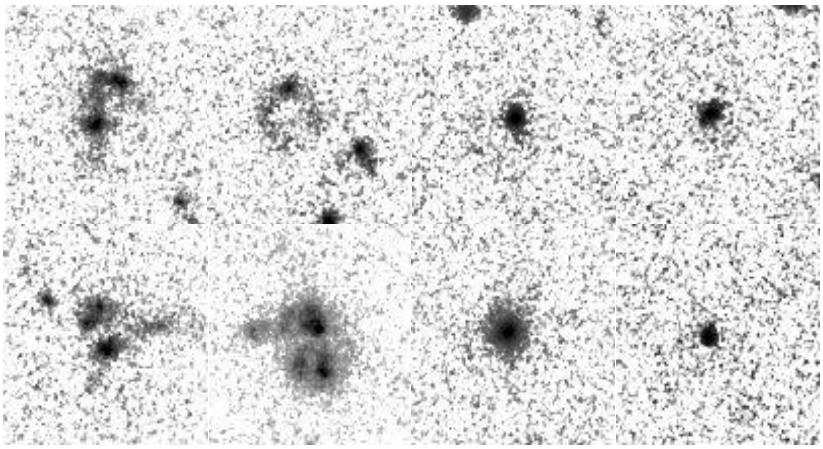

Figure 5.3.1: Morphological examples of SFR dominated starbursts (left) and AGN dominated starbursts (right). HST-ACS cutouts have a size of 5" x 5".

analysis reveals that the two starburst classes have different typical morphologies: pure star-forming starbursts (SBs-SFR) are disturbed systems (∼82% of the sample), with evident tidal interaction between multiple components (possibly ongoing mergers); SBs-AGN are (∼55%) dominated by regular compact and symmetric morphologies (nucleated objects similar to the blue nugget sources proposed by Tacchella et al., 2016, in the HST images). Typical examples of the different classes are shown in Fig. 5.3.1.

This morphological analysis should be taken carefully, since it is obviously limited by the shallowness of the COSMOS/HST imaging, but also by the huge intrinsic dust extinction associated to the SBs, that allows only a minor contribution of un-absorbed UV light to escape the obscured star-forming regions (Puglisi et al., 2017). Apart from these limitations, the results are interpreted as a supporting evidence that SBs-AGN are probably more compact and dense sources, perhaps corresponding to a final merger stage (as many local ULIRGs), when the original gas of the progenitors has been driven by dynamical interactions toward a common barycenter and the central super massive BHs (SMBH) are fed.

5.3.1 ALMA counterparts

I then searched for possible ALMA millimetric counterparts of the SBs in the public archive. The bulk of ALMA observations come from two different programs, 2103.1.00034.S and 2015.1.00137.S, both P.I. Nick Scoville. These observations are aimed at the characterization of the interstellar medium of more than ~ 200 galaxies at the peak of cosmic star formation and AGN activity, with sources spanning a redshift range between $z \sim 1.5$ and $z \sim 2.7$. Both programs observed the sources in band 7 at 870μm. The calibrated measurement sets are from the ALMA archive and were calibrated running the data reduction scripts with the Common Astronomy Software Applications (CASA).

From the reference SBs sample of 152 objects, adopting a search radius of 2.5", I identified four duplicated observations between the programs, two of which were previously undetected sources (z12_6 and z23_18). I kept only the latest observations of both.

The final sample comprises 33 sources with a clear detection above 3σ. Fluxes and associated errors were evaluated with CASA, by fitting the emissions with a bi-dimensional Gaussian, and are reported in Table 5.3.1. An independent flux estimation was also executed on the full dataset, by summing the signal inside customized apertures centered on the sources, with uncertainties measured as the root-mean-square variation of the signal evaluated with the same apertures in 100 random positions within the primary beam region. The results were consistent with each other. I include in the photometric analysis the fluxes computed with the former method.

SED fitting of the ALMA data has been performed by applying a top-hat filter on the data points centered on the continuum frequency and covering the full ALMA bandwidth. For the 33 ALMA detected sources, I included the 870μm flux in the observed SED, and performed a second fitting run, as described in Section 5.2. The updated physical parameters are reported in Table 5.3.1.

Table 5.3.1: Main observational and physical parameters of the SBs with an ALMA continuum detection. Redshifts between parenthesis are spectroscopic.

ID_COSMOS15	RA [deg]	DEC [deg]	z	L_{IR} [$L_\odot$]	M_* [$M_\odot$]	M_{gas} [$M_\odot$]	AGN	$F_{870\,\mu m}$ [mJy]	$F_{1.3mm}$ [mJy]	$F_{3.0mm}$ [mJy]
182648	150.64316	1.558194	1.6887	11.115	10.4616	10.341	yes	0.49±0.10	-	-
221280	149.76807	1.617000	2.3220	11.185	10.4703	10.782	yes	1.11±0.22	-	-
244448	150.01202	1.652130	(1.5180)	10.645	10.7505	10.972	no	2.01±0.25	-	-
280968	149.79010	1.711870	1.7844	11.343	10.4035	10.885	no	1.33±0.25	-	-
323041	149.81653	1.779770	2.0933	11.244	10.5122	10.519	yes	1.38±0.46	-	-
349784	150.48938	1.821710	1.9693	11.100	10.8425	11.128	no	1.59±0.34	-	-
386956	150.34194	1.880208	2.2493	11.346	10.6594	10.702	no	1.88±0.30	-	-
505526	150.42101	2.068100	2.2684	10.666	11.0934	11.813	yes	11.93±0.71	-	-
506667	150.72984	2.071170	2.4433	11.200	10.5955	11.091	no	2.23±0.77	-	-
524710	149.76853	2.099614	2.1059	11.321	10.4187	10.715	no	1.72±0.23	-	-
571598	150.61642	2.167971	1.5052	11.167	10.8600	11.293	no	5.39±0.23	-	-
578926	150.40103	2.180390	(2.3341)	11.567	10.9570	11.118	no	2.05±0.55	-	-
600601	150.13263	2.211940	1.9875	11.184	11.1349	11.582	yes	-	2.46±0.10	-
600601	150.13265	2.211946	1.9875	10.752	11.1349	11.581	yes	8.27±0.44	-	-
605409	149.76813	2.219876	(1.7766)	11.112	10.8708	11.085	no	3.78±1.03	-	-
640026	150.03663	2.270976	1.7977	11.313	10.2632	10.849	yes	1.09±0.27	-	-
642313	149.60419	2.275064	2.0069	11.254	10.6391	11.177	no	1.77±0.31	-	-
651584	149.92196	2.289929	2.3341	11.600	10.8786	11.127	no	4.93±0.34	-	-
734578	149.52823	2.413200	1.9641	11.765	10.5523	11.393	no	-	1.88±0.23	-
745498	150.46551	2.429549	1.6332	10.731	10.7144	10.856	no	3.47±0.34	-	-
747590	150.22447	2.433010	1.6351	10.903	10.6513	10.786	no	1.60±0.24	-	-
752016	150.33683	2.439920	2.2682	11.585	10.7232	11.165	no	4.50±0.31	-	-
754372	150.06907	2.444010	2.4355	11.439	11.0108	10.968	yes	4.86±0.65	-	0.275±0.065
769248	150.25528	2.466839	(2.2640)	10.903	10.5134	11.130	no	3.80±0.42	-	-
794848	150.09341	2.507339	2.1990	11.365	10.7362	11.149	yes	3.09±0.25	-	-
810228	150.11307	2.528020	2.0167	11.264	10.6265	11.188	no	-	-	0.137±0.060
815012	150.60329	2.536536	(2.2872)	11.119	11.1034	11.193	no	6.70±0.35	-	-
818426	150.72202	2.541904	2.2664	11.607	10.6405	11.308	yes	1.01±0.30	-	-
842595	149.99796	2.578227	2.4200	11.693	10.7809	11.232	yes	1.97±0.32	-	-
902320	150.03726	2.669600	(1.5990)	10.274	10.9826	11.662	no	6.41±0.39	-	0.147±0.057
917423	149.99218	2.693436	2.1284	11.330	10.7933	11.082	no	1.77±0.34	-	-
917546	150.16165	2.691588	(1.9745)	10.937	10.4437	10.657	yes	1.39±0.25	-	-
951838	150.26832	2.749270	2.0186	11.128	9.9814	10.577	yes	1.60±0.24	-	-
980250	150.01611	2.792355	1.7598	10.533	11.1303	11.375	no	5.03±0.25	-	-

5.4 Dust and molecular gas masses

Dust masses (M_{dust}) have been derived following the procedure described in Magdis et al. (2012), by fitting the SED in the IRAC-ALMA observed frame with the Draine and Li (2007) models. The total gas mass (M_{gas}, which incorporates both the molecular and atomic phases) can be inferred from the dust mass through a dust-to-gas ratio (DGR, e.g. Magdis et al., 2012, Eales et al., 2010b): $M_{gas} = M_{dust}/DGR$.

For the gas metallicity (Z) we adopt a solar metallicity for the whole sample (assuming the local $M_* - Z$ relation for ellipticals provides identical results, while the Fundamental Metallicity Relation by Mannucci et al. (2010, 2011) provides M_{gas} statistically larger by $\sim$0.15 dex, without impact on our main conclusions).

Without any direct Carbon Monoxide (CO) observations of the sources, I cannot provide a more direct and robust estimate of the gas masses. However the presented method avoid the introduction of any bias due to an assumed α_{CO} conversion factor. I refer to Magdis et al. (2012), Genzel et al. (2015), Scoville et al. (2016), Tacconi et al. (2018) for a comprehensive discussion on the implication of using gas masses derived from dust masses or CO luminosities.

5.5 Results and discussions

Here I report the main results of the analysis of the gas masses computed for the SBs with an ALMA continuum detection. Out of 24 sources, 10 objects turn out to be SBs-AGN, thus representing 40% of the full sample. It should be noted that this limited ALMA detected data-set is representative of the whole SB population in this redshift range (both in term of M_*, elevation above the MS and AGN content, as can be seen in Figure 5.1.1).

For subsequent comparative analyses, a reference sample is used as originally compiled by Sargent et al. (2014) that includes 'typical' star-forming galaxies at $z \leq 3$ with measurements of their CO luminosity. In addition, local ULIRGs and high-z starbursts are added that have a determination of CO, thus avoiding larger

uncertainties in the CO-to-gas conversion factor.

Detailed references for the various samples included are reported in Sargent et al. (2014). Here, I provide a brief summary of the reference data. The sample includes: normal SF galaxies at low redshift with CO-detections (HERACLES survey, Leroy et al., 2012) (COLDGASS, Saintonge et al., 2011); normal SF galaxies at intermediate and high-redshift with CO-detections (Geach et al., 2011, Daddi et al., 2010a,b, Tacconi et al., 2013); local starbursting galaxies with measured α_{CO} (Downes and Solomon, 1998, Papadopoulos et al., 2012). We added three high redshift starbursts : GN20 (z = 4.05; Tan et al., 2014), SMMJ2135-0102 (z = 2.325; Swinbank et al., 2011) and HERMES J105751.1+573027 (z = 2.957; Riechers et al., 2011) and the recent compilation of SBs by Silverman et al. (2015) and 2018 in prep., at $z \sim 1.6$.

5.5.1 Gas masses in SBs-AGN and SBs-SFR

Fig. 5.5.1 shows the gas masses of the SBs as a function of their M_*, divided into SBs-AGN and SBs-SFR (green and blue filled stars, respectively). As expected, the SB population is dominated by gas rich galaxies, with gas fractions (defined as $f_{\rm gas} = M_{\rm gas}/(M_{\rm gas} + M_*)$) spanning the range 45%-85%. This is partly overlapping with the typical $f_{\rm gas}$ ($\sim 50\%$) of the normal star-forming sources at similar z (open circles), reaching, however, much higher fractions when moving above the MS (similar results were observed by Scoville et al. (2016)). Local star-forming galaxies (both MS and ULIRGs/SBs) are instead much gas poorer, with $f_{\rm gas} \sim 10\%$, as expected on the basis of the observed gas fraction evolution with cosmic time (e.g. Tacconi et al., 2018, and references therein).

When looking at the separate gas fractions of SBs-AGN and SBs-SFR, there is no significant difference, providing average values of $f_{\rm gas} = 71 \pm 3\%$ and $f_{\rm gas} = 65 \pm 2\%$ for the two classes, respectively. This is different from what has been found by some authors for objects in the MS. For example, following a similar approach to estimating the gas masses from the dust continuum, Vito et al. (2014) found that, on average, (X-ray) AGN are hosted in galaxies that are

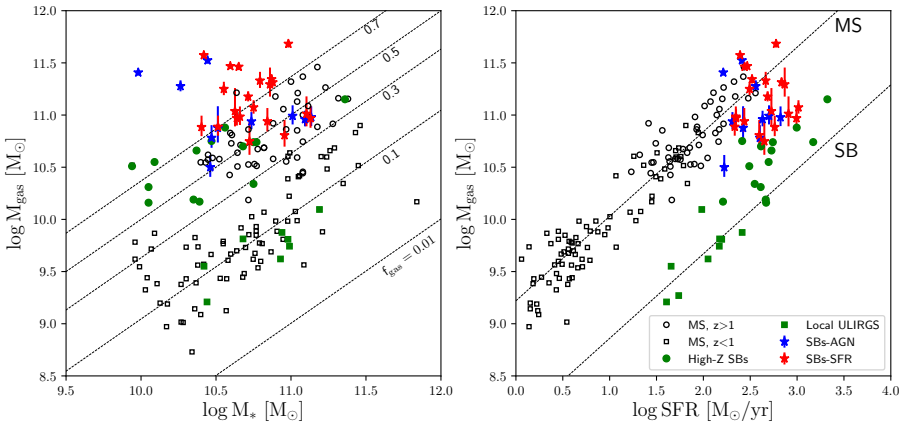

Figure 5.5.1: *Left panel:* Gas mass as a function of the stellar mass for the sample with an ALMA continuum detection (blue stars: SBs-AGN; red stars: SB-SFRs). Dotted lines are loci of constant gas fraction (i.e. $M_{\rm gas}/(M_{\rm gas} + M_*)$). Open black squares (circles) represent star-forming MS galaxies at $z < 1 (> 1)$ as compiled by Sargent et al. (2014). Green symbols show the local ULIRGs (filled green squares) and high-z starbursts (filled green circles). *Right panel:* Gas mass as a function of the SFR. Symbols are as in the previous panel. Empirical model curves (dashed lines) are described in Sargent et al. (2014) and mark the positions normal star-forming (MS) and ULIRGs/starbursts (SB).

much more gas rich than inactive galaxies (up to a factor of ten for the less massive galaxies). The authors interpret this result in a statistical sense, where probability of having an AGN in an active phase is correlated with the gas reservoir in the hosts (feeding both the SFR and the central SMBHs). Their work, however, does not include millimetric ALMA data, being limited to Herschel for the longest wavelength data used to extrapolate the dust and gas masses. Moreover, the quoted gas fractions of both AGN and normal galaxies are unusually low for the highest-z population ($\sim 1\%$ even for the most massive galaxies, i.e. $M_* = 10^{11}\,M_\odot$ at $z = 1$) and probably miss a large fraction of obscured AGN (that is recovered here through the dusty torus detection). The general interpretation is, however, complicated by opposite results found for example by Kakkad et al. (2017), who studied the gas content in AGN lying on the MS, through the observation of the CO luminosity. They found indication that $z = 1.5$ galaxies hosting an AGN have lower gas fraction than the average non-active star forming galaxies, supporting the idea that the host gas reservoirs have been reduced by feedback effects (or simply underwent faster gas depletion). Such differences might be attributed to the different selection criteria for the active population, and to the methods used to compute the global molecular gas content of galaxies.

To shed more light on these important issues concerning the most efficient star-forming sources, a further study of the distribution of $M_{\rm gas}$ as a function of SFR is reported in the right panel of Fig. 5.5.1, in order to compare the gas content and the star formation efficiency (i.e. SFE=SFR/$M_{\rm gas}$) of SBs-AGN and SBs-SFR. Clearly, the sample selected here turn to be "SFR-selected" by construction, with SFR$\geq\ 150\,M_\odot\ {\rm yr}^{-1}$ due to the requirement of being Herschel selected (see Fig. 5.1.1). It should be noticed that SBs lie on a contiguous sequence of increasing SFE, that fill the gap between the two paradigmatic sequences of normal galaxies and ULIRG/SBs (dotted lines, as from Sargent et al. (2014), usually interpreted as the main loci of two extremely different SF modes. These results support recent works suggesting the existence of a continuous increase in SFE with elevation from the main sequence (with

galaxy mergers as a possible physical driver, Silverman et al., 2015).

In this sample SBs-AGN have, on average, slightly shorter depletion times (τ_{depl}=1/SFE), with $\tau_{depl} \simeq 70$ Myr compared to SBs-SFR with $\tau_{depl} \simeq 115$ Myr, but a much larger statistics is required to make this conclusion significant.

This emerging scenario is corroborated by recent observations of molecular gas in high-z quasars (Perna et al., 2018), showing that $z > 1$ obscured and starbursting AGN have higher SFE with respect to normal star forming galaxies.

5.5.2 Comparison with the merger triggered SB-QSO evolutionary sequence

As mentioned earlier, it is possible to compare these results to the expectations of the AGN-galaxy co-evolutionary scenario, that predicts a luminous IR phase of buried SMBH growth, co-existing with a starburst (likely arising from a merger) before feedback phenomena deplete the cold molecular gas reservoir of the galaxy and an optically luminous quasar (QSO) is revealed (Hopkins et al., 2008, Menci et al., 2008).

On a qualitative side, it is observed that starbursting AGN have on average more compact and nucleated UV-restframe morphologies with respect to "inactive" SBs, suggesting that they are kept in a different dynamical evolutionary phase. This could correspond to the key transition when the late mergers trigger a high SFR, before the fully developed AGN phase. Simulations and observations, indeed, suggests a temporal delay from the peak of the SFR and the ignition of the AGN (Rodighiero et al., 2015, Bergvall et al., 2016, Lapi et al., 2016).

On the other hand, there is no significant reduction of gas fractions in the SBs-AGN hosts compared to "inactive" SBs-SFR companions. If major mergers are the main triggering mechanism of obscured BHAR in SBs, feedback phenomena (producing large outflows from the central BH) are not efficient in removing significant amount of molecular gas in the host galaxies, as required to suddenly quench these behemoths.

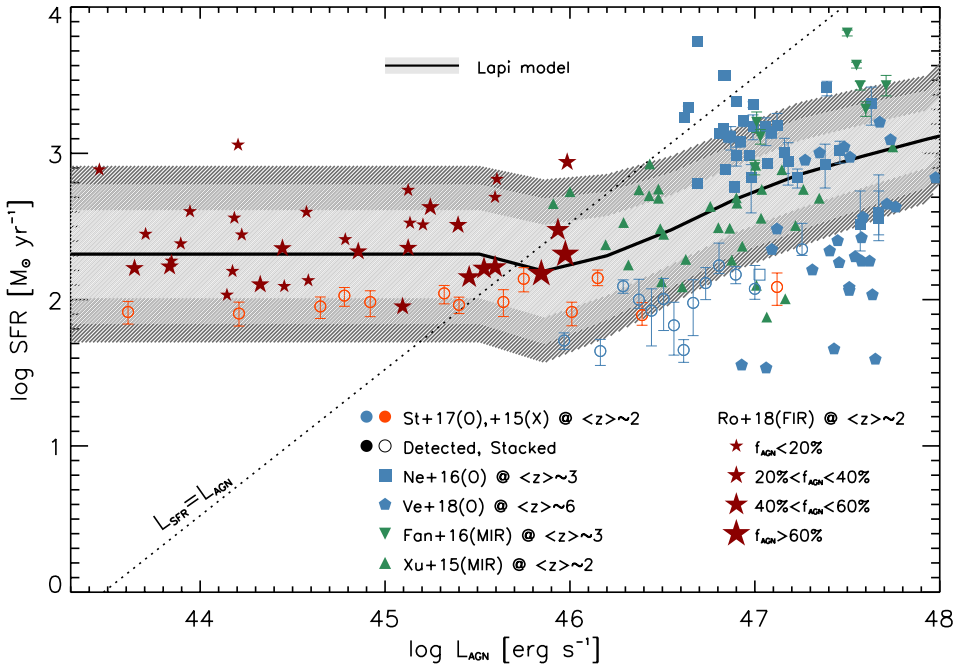

Figure 5.5.2: Coevolution plane between bolometric AGN luminosity and SFR in the host galaxies at $z > 1.5$. The dotted line marks where the bolometric luminosity from AGN emission and from star formation are equal. Gray shaded areas show the average locus of the evolutionary tracks from the simple coevolution scenario by Lapi et al. (2014, 2017). Orange symbols refer to X-ray selected AGNs, green to mid-IR selected AGNs and blue are optically selected QSO. Complete references are reported in Bianchini et al. (2018). We include the full population of SBs-AGN in our original sample, coded as red filled stars: the size of the symbol is proportional it its AGN luminosity contribution in the mid-IR (in the 5-40μm range, see Delvecchio et al., 2017).

5.5.3 Starbursts as young primordial galaxies

An alternative interpretation for the properties of the off-main sequence galaxies in the present sample is provided by the in-situ coevolution scenario from Lapi et al. (2018, 2014, 2017), (see also Mancuso et al., 2016, Bianchini et al., 2018); this envisages high-redshift galaxy evolution to be mainly ruled by the interplay between in-situ star formation, accretion onto the hosted central SMBHs, and related feedback processes.

According to such a scenario (as outlined in Chapter 3 of this Thesis), high-redshift $z \sim 2$ star-forming galaxies with SFR higher than a few $10^2\,M_\odot\,\mathrm{yr}^{-1}$ constitute the progenitor of local massive spheroids with final stellar mass $M_\star \geq 10^{11}\,M_\odot$. During their starforming phase, lasting some 10^8 yr, these galaxies feature a nearly constant SFR and a linearly increasing stellar mass. Thus in the SFR-$M*$ diagram they follow an almost horizontal track (see Fig. 10 in Lapi et al., 2017) while moving toward the galaxy MS locus; there they will have acquired most of their mass before being quenched by energy/momentum feedback from the SMBH. Far-IR selected, off-main sequence galaxies (like in the galaxy sample of this work) are simply interpreted as young objects, still rich in gas and dust and with small though increasing stellar mass.

Being in the early stages of their evolution, these SBs can host only a rather small SMBH, originating an AGN luminosity $L_{\rm AGN}$ weaker than the $L_{\rm SFR}$ associated to the star formation in the host. However, the BH mass is expected to grow exponentially (e.g., in an Eddington limited fashion), and this generates a noticeable statistical variance in $L_{\rm AGN}$ at given SFR. As a consequence, in the SFR vs. $L_{\rm AGN}$ plane, SBs are expected to populate a strip parallel to the $L_{\rm AGN}$ axis, and located to the left of the locus where $L_{\rm SFR} = L_{\rm AGN}$, as in Fig. 5.5.2 or Fig. 7 in (Bianchini et al., 2018). The hosted AGNs are expected to be heavily obscured, with an appreciable mid-IR and and/or hard X-ray emission. In addition, the AGN luminosity is still not powerful enough to originate substantial feedback effects on the ISM of the host galaxy; thus, the SFR and the gas mass of the host are still not much affected. As time passes by and the galaxy gets older, the

luminosity of the AGN will overwhelm that of the star formation in the host, removing gas and dust from the ISM and quenching the SFR and the accretion itself; the system will then shine as a bright optical quasar, progressively moving toward the bottom right region of the SFR vs. $L_{\rm AGN}$ diagram.

To sum up, the in-situ coevolution scenario predicts relatively high gas fractions and no trend with AGN luminosity for the present sample of far-IR selected, SBs; these are interpreted as young systems, still relatively far from the epoch when the AGN feedback will quench the star formation in the host and will substantially depress the gas fractions. The properties of the sample described in this work are indeed consistent with such a picture.

In conclusion, the preliminary results presented here are consistent with the idea that the SB population could be filled by a mixture of: 1) low-mass primordial galaxies, quickly accreting their $M*$ together with their BH (mainly the SBs-AGN), and 2) a class of highly star-forming merging sources (preferentially among the SBs-SFR). In both cases, feedback effects did not appear to have yet started to eventually reduce the gas fraction of the objects. Alternatively, we suggest that our results might more simply indicate that feedback processes (in form of galactic outflows from the SMBH) have not the power to eject sufficient gas masses from the host galaxies.

Larger samples of starbursts with a millimetric measurement will be required to provide a statistical description of the gas content in this population and to understand the impact of the co-evolving obscured central activity, being CO detections for wide samples too expensive in terms of observational time.

6

Future perspectives

Our understanding of the young Universe has significantly improved in the last decade. Great improvements in sub-mm astronomy translated into great scientific achievements. During these years, new light has been shed on the formation and evolution of the complex variety of structures observed in present-day Universe. The sub-mm bright population of dusty starforming galaxies, once poor known objects rarely seen in the local Universe, are now currently at the center of numerous investigations that are unveiling their physical properties, closing the gap that connects this population (and the violent starforming past of the Universe at cosmic noon) to the massive, gas-free and dead Early-Type Galaxies.

This achievements are mainly due to the great developments in sub-mm astronomy. First, the increasing number of large area surveys improved the statistics of these sources, better defining their intrinsic characteristics, i.e gas and

dust composition and masses, star formation rates, physical sizes. Second, the commissioning and entry into operation of ALMA, alongside with the previous class of available interferometers (e.g. the Submillimetre Array, Plateau de Bure Interferometer), allowed scientists to perform detailed studies of single sources, resolving in some cases their clumpy, inhomogeneous morphologies, the single starforming regions, even their dynamics.

Gravitational lensing has been critical in achieving those results. The great increase in angular resolution generated by a gravitational lens, along with the high number of efficient lens modelling techniques (e.g. the SemiLinear Inversion Warren and Dye, 2003, see Chapter 2), pushed the limit of the observable at high-z. Once the consequence of a serendipitous observation, now strongly lensed galaxies are systematically found, thanks to the flux limit technique that has proven to be successful in detecting magnified sub-mm sources inside large area surveys (Negrello et al., 2017, or see Chapter 3). In the coming years, a series of follow-up observations will increase the number of confirmed and modelled DSFGs at high-z from the current 20/25 to ~ 80 sources in the H-ATLAS fields alone, a number that rises to over a hundred when considering analogous surveys such as the SPT survey (Vieira et al., 2013). In this way a large, reliable sample of strongly lensed galaxies will be available, allowing scientists to answer fundamental cosmological and astrophysical questions on the Universe itself and the structures within (i.e., from the point of view of the lens, high-resolution interferometric observations of strongly lensed galaxies might be able to detect dark matter subhaloes in the lens galaxy, see Vegetti et al., 2012, Hezaveh et al., 2016, for further details).

A boost in the number of candidate (and confirmed) strongly lensed sub-mm galaxies will come with the Square Kilometer Array (SKA). Mancuso et al. (2015) showed that strong lensing will play a significant in the number counts of high-z galaxies detected in SKA surveys. Calculations show that, by adopting a SISSA profile for the lens galaxy (Lapi et al., 2012) and a maximum magnification $\mu_{\rm max} = 30$ (Bonato et al., 2014, found it as a good fit for the SPT lensed DSFGs counts), the number of strongly lensed galaxies per square degree

brighter than the 5σ detection limit of 0.25, 1, 5 and 50 μJy are, respectively, 1195, 432, 101 and 7.6 (or a fraction of $\sim 0.5\% - 0.6\%$ of the total number of detections). This means that directly in the first phases of these surveys a number comprised between a hundred and a thousand candidate strongly lensed galaxies will be identified. Furthermore, the high spatial resolution of SKA1-MID surveys will allow the detection of multiple images of the same source for a fraction of these, $\sim 20\% - 30\%$, leading to direct confirmation of the strong lensing nature for a significant part of the sample. Further follow-up observations with facilities such as ALMA or SMA will confirm the lensing nature of the remaining sample, or increase the quality of observation (and therefore lens modelling and source reconstruction) for the confirmed systems.

Gravitational lensing in the sub-mm has just started to unveil the physical nature of dusty starforming galaxies, responsible for the peak of star formation rate density during the *cosmic noon*, when the young Universe formed stars at a hectic pace. The next decade of detection, identification, confirmation and modelling of the sources will help scientists to close the gap on the remaining questions surrounding their formation and evolution, and the link between this population and the ETGs.

References

S. J. Warren and S. Dye. Semilinear Gravitational Lens Inversion. ApJ, 590: 673–682, June 2003. doi: 10.1086/375132.

A. Enia, M. Negrello, M. Gurwell, S. Dye, G. Rodighiero, M. Massardi, G. De Zotti, A. Franceschini, A. Cooray, P. van der Werf, M. Birkinshaw, M. J. Michałowski, and I. Oteo. The Herschel-ATLAS: magnifications and physical sizes of 500-μm-selected strongly lensed galaxies. MNRAS, 475:3467–3484, April 2018. doi: 10.1093/mnras/sty021.

R. S. Bussmann, I. Pérez-Fournon, S. Amber, J. Calanog, M. A. Gurwell, H. Dannerbauer, F. De Bernardis, H. Fu, A. I. Harris, M. Krips, A. Lapi, R. Maiolino, A. Omont, D. Riechers, J. Wardlow, A. J. Baker, M. Birkinshaw, J. Bock, N. Bourne, D. L. Clements, A. Cooray, G. De Zotti, L. Dunne, S. Dye, S. Eales, D. Farrah, R. Gavazzi, J. González Nuevo, R. Hopwood, E. Ibar, R. J. Ivison, N. Laporte, S. Maddox, P. Martínez-Navajas, M. Michalowski, M. Negrello, S. J. Oliver, I. G. Roseboom, D. Scott, S. Serjeant, A. J. Smith, M. Smith, A. Streblyanska, E. Valiante, P. van der Werf, A. Verma, J. D. Vieira, L. Wang, and D. Wilner. Gravitational Lens Models Based on Submillimeter Array Imaging of Herschel-selected Strongly Lensed Sub-millimeter Galaxies at $z > 1.5$. ApJ, 779:25, December 2013. doi: 10.1088/0004-637X/779/1/25.

P. Madau and M. Dickinson. Cosmic Star-Formation History. ARA&A, 52: 415–486, August 2014. doi: 10.1146/annurev-astro-081811-125615.

A. W. Blain, A. Jameson, I. Smail, M. S. Longair, J.-P. Kneib, and R. J. Ivison. Dust-obscured star formation and AGN fuelling in hierarchical models of galaxy evolution. MNRAS, 309:715–730, November 1999. doi: 10.1046/j.1365-8711.1999.02879.x.

A. W. Blain, I. Smail, R. J. Ivison, J.-P. Kneib, and D. T. Frayer. Submillimeter

galaxies. Phys. Rep., 369:111–176, October 2002. doi: 10.1016/S0370-1573(02)00134-5.

D. H. Hughes, S. Serjeant, J. Dunlop, M. Rowan-Robinson, A. Blain, R. G. Mann, R. Ivison, J. Peacock, A. Efstathiou, W. Gear, S. Oliver, A. Lawrence, M. Longair, P. Goldschmidt, and T. Jenness. High-redshift star formation in the Hubble Deep Field revealed by a submillimetre-wavelength survey. Nature, 394:241–247, July 1998. doi: 10.1038/28328.

W. S. Holland, E. I. Robson, W. K. Gear, C. R. Cunningham, J. F. Lightfoot, T. Jenness, R. J. Ivison, J. A. Stevens, P. A. R. Ade, M. J. Griffin, W. D. Duncan, J. A. Murphy, and D. A. Naylor. SCUBA: a common-user submillimetre camera operating on the James Clerk Maxwell Telescope. MNRAS, 303: 659–672, March 1999. doi: 10.1046/j.1365-8711.1999.02111.x.

I. Smail, R. J. Ivison, and A. W. Blain. A Deep Sub-millimeter Survey of Lensing Clusters: A New Window on Galaxy Formation and Evolution. ApJ, 490: L5–L8, November 1997. doi: 10.1086/311017.

A. J. Barger, L. L. Cowie, D. B. Sanders, E. Fulton, Y. Taniguchi, Y. Sato, K. Kawara, and H. Okuda. Submillimetre-wavelength detection of dusty star-forming galaxies at high redshift. Nature, 394:248–251, July 1998. doi: 10.1038/28338.

S. Eales, S. Lilly, W. Gear, L. Dunne, J. R. Bond, F. Hammer, O. Le Fèvre, and D. Crampton. The Canada-UK Deep Submillimeter Survey: First Submillimeter Images, the Source Counts, and Resolution of the Background. ApJ, 515:518–524, April 1999. doi: 10.1086/307069.

J. D. Vieira, T. M. Crawford, E. R. Switzer, P. A. R. Ade, K. A. Aird, M. L. N. Ashby, B. A. Benson, L. E. Bleem, M. Brodwin, J. E. Carlstrom, C. L. Chang, H.-M. Cho, A. T. Crites, T. de Haan, M. A. Dobbs, W. Everett, E. M. George, M. Gladders, N. R. Hall, N. W. Halverson, F. W. High, G. P. Holder, W. L. Holzapfel, J. D. Hrubes, M. Joy, R. Keisler, L. Knox, A. T. Lee, E. M. Leitch, M. Lueker, D. P. Marrone, V. McIntyre, J. J. McMahon, J. Mehl, S. S. Meyer, J. J. Mohr, T. E. Montroy, S. Padin, T. Plagge, C. Pryke, C. L. Reichardt, J. E. Ruhl, K. K. Schaffer, L. Shaw, E. Shirokoff, H. G. Spieler, B. Stalder, Z. Staniszewski, A. A. Stark, K. Vanderlinde, W. Walsh, R. Williamson, Y. Yang, O. Zahn, and A. Zenteno. Extragalactic Millimeter-wave Sources in South Pole Telescope Survey Data: Source Counts, Catalog, and Statistics for an 87 Square-degree Field. ApJ, 719:763–783, August 2010. doi: 10.1088/0004-637X/719/1/763.

J. M. Simpson, A. M. Swinbank, I. Smail, D. M. Alexander, W. N. Brandt, F. Bertoldi, C. de Breuck, S. C. Chapman, K. E. K. Coppin, E. da Cunha, A. L. R. Danielson, H. Dannerbauer, T. R. Greve, J. A. Hodge, R. J. Ivison, A. Karim, K. K. Knudsen, B. M. Poggianti, E. Schinnerer, A. P. Thomson, F. Walter, J. L. Wardlow, A. Weiß, and P. P. van der Werf. An ALMA Survey of Submillimeter Galaxies in the Extended Chandra Deep Field South: The Redshift Distribution and Evolution of Submillimeter Galaxies. ApJ, 788:125, June 2014. doi: 10.1088/0004-637X/788/2/125.

J. M. Simpson, I. Smail, A. M. Swinbank, R. J. Ivison, J. S. Dunlop, J. E. Geach, O. Almaini, V. Arumugam, M. N. Bremer, C.-C. Chen, C. Conselice, K. E. K. Coppin, D. Farrah, E. Ibar, W. G. Hartley, C. J. Ma, M. J. Michałowski, D. Scott, M. Spaans, A. P. Thomson, and P. P. van der Werf. The SCUBA-2 Cosmology Legacy Survey: Multi-wavelength Properties of ALMA-identified Submillimeter Galaxies in UKIDSS UDS. ApJ, 839:58, April 2017. doi: 10.3847/1538-4357/aa65d0.

C. M. Casey, D. Narayanan, and A. Cooray. Dusty star-forming galaxies at high redshift. Phys. Rep., 541:45–161, August 2014. doi: 10.1016/j.physrep.2014.02.009.

A. J. Benson. Galaxy formation theory. Phys. Rep., 495:33–86, October 2010. doi: 10.1016/j.physrep.2010.06.001.

A. Dekel, Y. Birnboim, G. Engel, J. Freundlich, T. Goerdt, M. Mumcuoglu, E. Neistein, C. Pichon, R. Teyssier, and E. Zinger. Cold streams in early massive hot haloes as the main mode of galaxy formation. Nature, 457: 451–454, January 2009. doi: 10.1038/nature07648.

G. L. Granato, G. De Zotti, L. Silva, A. Bressan, and L. Danese. A Physical Model for the Coevolution of QSOs and Their Spheroidal Hosts. ApJ, 600:580–594, January 2004. doi: 10.1086/379875.

L. Ferrarese and D. Merritt. A Fundamental Relation between Supermassive Black Holes and Their Host Galaxies. ApJ, 539:L9–L12, August 2000. doi: 10.1086/312838.

K. Gebhardt, R. Bender, G. Bower, A. Dressler, S. M. Faber, A. V. Filippenko, R. Green, C. Grillmair, L. C. Ho, J. Kormendy, T. R. Lauer, J. Magorrian, J. Pinkney, D. Richstone, and S. Tremaine. A Relationship between Nuclear

Black Hole Mass and Galaxy Velocity Dispersion. ApJ, 539:L13–L16, August 2000. doi: 10.1086/312840.

F. Shankar, D. H. Weinberg, and J. Miralda-Escudé. Self-Consistent Models of the AGN and Black Hole Populations: Duty Cycles, Accretion Rates, and the Mean Radiative Efficiency. ApJ, 690:20–41, January 2009. doi: 10.1088/0004-637X/690/1/20.

I. Delvecchio, D. Lutz, S. Berta, D. J. Rosario, G. Zamorani, F. Pozzi, C. Gruppioni, C. Vignali, M. Brusa, A. Cimatti, D. L. Clements, A. Cooray, D. Farrah, G. Lanzuisi, S. Oliver, G. Rodighiero, P. Santini, and M. Symeonidis. Mapping the average AGN accretion rate in the SFR-M_* plane for Herschel-selected galaxies at $0 < z \leq 2.5$. MNRAS, $449 : 373 - -389, \mathit{May} 2015. \mathit{doi} : .$

C. Mancuso, A. Lapi, J. Shi, Z.-Y. Cai, J. Gonzalez-Nuevo, M. Béthermin, and L. Danese. The Main Sequences of Star-forming Galaxies and Active Galactic Nuclei at High Redshift. ApJ, 833:152, December 2016. doi: 10.3847/1538-4357/833/2/152.

A. Lapi, L. Pantoni, L. Zanisi, J. Shi, C. Mancuso, M. Massardi, F. Shankar, A. Bressan, and L. Danese. The Dramatic Size and Kinematic Evolution of Massive Early-type Galaxies. ApJ, 857:22, April 2018. doi: 10.3847/1538-4357/aab6af.

S. P. Driver, P. Norberg, I. K. Baldry, S. P. Bamford, A. M. Hopkins, J. Liske, J. Loveday, J. A. Peacock, D. T. Hill, L. S. Kelvin, A. S. G. Robotham, N. J. G. Cross, H. R. Parkinson, M. Prescott, C. J. Conselice, L. Dunne, S. Brough, H. Jones, R. G. Sharp, E. van Kampen, S. Oliver, I. G. Roseboom, J. Bland-Hawthorn, S. M. Croom, S. Ellis, E. Cameron, S. Cole, C. S. Frenk, W. J. Couch, A. W. Graham, R. Proctor, R. De Propris, I. F. Doyle, E. M. Edmondson, R. C. Nichol, D. Thomas, S. A. Eales, M. J. Jarvis, K. Kuijken, O. Lahav, B. F. Madore, M. Seibert, M. J. Meyer, L. Staveley-Smith, S. Phillipps, C. C. Popescu, A. E. Sansom, W. J. Sutherland, R. J. Tuffs, and S. J. Warren. GAMA: towards a physical understanding of galaxy formation. *Astronomy and Geophysics*, 50(5): 5.12–5.19, October 2009. doi: 10.1111/j.1468-4004.2009.50512.x.

S. Eales, L. Dunne, D. Clements, A. Cooray, G. De Zotti, S. Dye, R. Ivison, M. Jarvis, G. Lagache, S. Maddox, M. Negrello, S. Serjeant, M. A. Thompson, E. Van Kampen, A. Amblard, P. Andreani, M. Baes, A. Beelen, G. J. Bendo, D. Benford, F. Bertoldi, J. Bock, D. Bonfield, A. Boselli, C. Bridge, V. Buat, D. Burgarella, R. Carlberg, A. Cava, P. Chanial, S. Charlot, N. Christopher, P. Coles, L. Cortese, A. Dariush, E. da Cunha, G. Dalton, L. Danese,

H. Dannerbauer, S. Driver, J. Dunlop, L. Fan, D. Farrah, D. Frayer, C. Frenk, J. Geach, J. Gardner, H. Gomez, J. González-Nuevo, E. González-Solares, M. Griffin, M. Hardcastle, E. Hatziminaoglou, D. Herranz, D. Hughes, E. Ibar, W.-S. Jeong, C. Lacey, A. Lapi, A. Lawrence, M. Lee, L. Leeuw, J. Liske, M. López-Caniego, T. Müller, K. Nandra, P. Panuzzo, A. Papageorgiou, G. Patanchon, J. Peacock, C. Pearson, S. Phillipps, M. Pohlen, C. Popescu, S. Rawlings, E. Rigby, M. Rigopoulou, A. Robotham, G. Rodighiero, A. Sansom, B. Schulz, D. Scott, D. J. B. Smith, B. Sibthorpe, I. Smail, J. Stevens, W. Sutherland, T. Takeuchi, J. Tedds, P. Temi, R. Tuffs, M. Trichas, M. Vaccari, I. Valtchanov, P. van der Werf, A. Verma, J. Vieria, C. Vlahakis, and G. J. White. The Herschel ATLAS. PASP, 122:499–515, May 2010a. doi: 10.1086/653086.

D. Walsh, R. F. Carswell, and R. J. Weymann. 0957 + 561 A, B - Twin quasistellar objects or gravitational lens. Nature, 279:381–384, May 1979. doi: 10.1038/279381a0.

G. Soucail, Y. Mellier, B. Fort, G. Mathez, and M. Cailloux. The giant arc in A 370 - Spectroscopic evidence for gravitational lensing from a source at Z = 0.724. *Astronomy & Astrophysics*, 191:L19–L21, February 1988.

J. N. Hewitt, E. L. Turner, D. P. Schneider, B. F. Burke, and G. I. Langston. Unusual radio source MG1131+0456 - A possible Einstein ring. *Nature*, 333: 537–540, June 1988. doi: 10.1038/333537a0.

M. J. Irwin, R. L. Webster, P. C. Hewett, R. T. Corrigan, and R. I. Jedrzejewski. Photometric variations in the Q2237 + 0305 system - First detection of a microlensing event. *The Astronomical Journal*, 98:1989–1994, December 1989. doi: 10.1086/115272.

J. A. Tyson, R. A. Wenk, and F. Valdes. Detection of systematic gravitational lens galaxy image alignments - Mapping dark matter in galaxy clusters. *The Astrophysical Journal, Letters*, 349:L1–L4, January 1990. doi: 10.1086/185636.

A. S. Bolton, S. Burles, D. J. Schlegel, D. J. Eisenstein, and J. Brinkmann. Sloan Digital Sky Survey Spectroscopic Lens Search. I. Discovery of Intermediate-Redshift Star-forming Galaxies behind Foreground Luminous Red Galaxies. *The Astronomical Journal*, 127:1860–1882, April 2004. doi: 10.1086/382714.

A. M. Swinbank, I. Smail, S. Longmore, A. I. Harris, A. J. Baker, C. De Breuck, J. Richard, A. C. Edge, R. J. Ivison, R. Blundell, K. E. K. Coppin, P. Cox, M. Gurwell, L. J. Hainline, M. Krips, A. Lundgren, R. Neri, B. Siana, G. Siringo, D. P. Stark, D. Wilner, and J. D. Younger. Intense star formation within resolved

compact regions in a galaxy at z = 2.3. Nature, 464:733–736, April 2010. doi: 10.1038/nature08880.

I. W. A. Browne, P. N. Wilkinson, N. J. F. Jackson, et al. The Cosmic Lens All-Sky Survey - II. Gravitational lens candidate selection and follow-up. *Monthly Notices of the Royal Astronomical Society*, 341:13–32, May 2003. doi: 10.1046/j.1365-8711.2003.06257.x.

M. Negrello, F. Perrotta, J. González-Nuevo, L. Silva, G. de Zotti, G. L. Granato, C. Baccigalupi, and L. Danese. Astrophysical and cosmological information from large-scale submillimetre surveys of extragalactic sources. MNRAS, 377: 1557–1568, June 2007. doi: 10.1111/j.1365-2966.2007.11708.x.

G. L. Pilbratt, J. R. Riedinger, T. Passvogel, G. Crone, D. Doyle, U. Gageur, A. M. Heras, C. Jewell, L. Metcalfe, S. Ott, and M. Schmidt. Herschel Space Observatory. An ESA facility for far-infrared and submillimetre astronomy. A&A, 518:L1, July 2010.

M. Negrello, R. Hopwood, G. De Zotti, A. Cooray, A. Verma, J. Bock, D. T. Frayer, M. A. Gurwell, A. Omont, R. Neri, H. Dannerbauer, L. L. Leeuw, E. Barton, J. Cooke, S. Kim, E. da Cunha, G. Rodighiero, P. Cox, D. G. Bonfield, M. J. Jarvis, S. Serjeant, R. J. Ivison, S. Dye, I. Aretxaga, D. H. Hughes, E. Ibar, F. Bertoldi, I. Valtchanov, S. Eales, L. Dunne, S. P. Driver, R. Auld, S. Buttiglione, A. Cava, C. A. Grady, D. L. Clements, A. Dariush, J. Fritz, D. Hill, J. B. Hornbeck, L. Kelvin, G. Lagache, M. Lopez-Caniego, J. Gonzalez-Nuevo, S. Maddox, E. Pascale, M. Pohlen, E. E. Rigby, A. Robotham, C. Simpson, D. J. B. Smith, P. Temi, M. A. Thompson, B. E. Woodgate, D. G. York, J. E. Aguirre, A. Beelen, A. Blain, A. J. Baker, M. Birkinshaw, R. Blundell, C. M. Bradford, D. Burgarella, L. Danese, J. S. Dunlop, S. Fleuren, J. Glenn, A. I. Harris, J. Kamenetzky, R. E. Lupu, R. J. Maddalena, B. F. Madore, P. R. Maloney, H. Matsuhara, M. J. Michałowski, E. J. Murphy, B. J. Naylor, H. Nguyen, C. Popescu, S. Rawlings, D. Rigopoulou, D. Scott, K. S. Scott, M. Seibert, I. Smail, R. J. Tuffs, J. D. Vieira, P. P. van der Werf, and J. Zmuidzinas. The Detection of a Population of Submillimeter-Bright, Strongly Lensed Galaxies. *Science*, 330:800, November 2010. doi: 10.1126/science.1193420.

R. S. Bussmann, M. A. Gurwell, H. Fu, D. J. B. Smith, S. Dye, R. Auld, M. Baes, A. J. Baker, D. Bonfield, A. Cava, D. L. Clements, A. Cooray, K. Coppin, H. Dannerbauer, A. Dariush, G. De Zotti, L. Dunne, S. Eales, J. Fritz, R. Hopwood, E. Ibar, R. J. Ivison, M. J. Jarvis, S. Kim, L. L. Leeuw, S. Maddox, M. J. Michałowski, M. Negrello, E. Pascale, M. Pohlen, D. A. Riechers, E. Rigby, D. Scott, P. Temi, P. P. Van der Werf, J. Wardlow, D. Wilner, and A. Verma. A

Detailed Gravitational Lens Model Based on Submillimeter Array and Keck Adaptive Optics Imaging of a Herschel-ATLAS Submillimeter Galaxy at z = 4.243. ApJ, 756:134, September 2012. doi: 10.1088/0004-637X/756/2/134.

H. Fu, E. Jullo, A. Cooray, R. S. Bussmann, R. J. Ivison, I. Pérez-Fournon, S. G. Djorgovski, N. Scoville, L. Yan, D. A. Riechers, J. Aguirre, R. Auld, M. Baes, A. J. Baker, M. Bradford, A. Cava, D. L. Clements, H. Dannerbauer, A. Dariush, G. De Zotti, H. Dole, L. Dunne, S. Dye, S. Eales, D. Frayer, R. Gavazzi, M. Gurwell, A. I. Harris, D. Herranz, R. Hopwood, C. Hoyos, E. Ibar, M. J. Jarvis, S. Kim, L. Leeuw, R. Lupu, S. Maddox, P. Martínez-Navajas, M. J. Michałowski, M. Negrello, A. Omont, M. Rosenman, D. Scott, S. Serjeant, I. Smail, A. M. Swinbank, E. Valiante, A. Verma, J. Vieira, J. L. Wardlow, and P. van der Werf. A Comprehensive View of a Strongly Lensed Planck-Associated Submillimeter Galaxy. ApJ, 753:134, July 2012. doi: 10.1088/0004-637X/753/2/134.

H. Messias, S. Dye, N. Nagar, G. Orellana, R. S. Bussmann, J. Calanog, H. Dannerbauer, H. Fu, E. Ibar, A. Inohara, R. J. Ivison, M. Negrello, D. A. Riechers, Y.-K. Sheen, J. E. Aguirre, S. Amber, M. Birkinshaw, N. Bourne, C. M. Bradford, D. L. Clements, A. Cooray, G. De Zotti, R. Demarco, L. Dunne, S. Eales, S. Fleuren, J. Kamenetzky, R. E. Lupu, S. J. Maddox, D. P. Marrone, M. J. Michałowski, E. J. Murphy, H. T. Nguyen, A. Omont, K. Rowlands, D. Smith, M. Smith, E. Valiante, and J. D. Vieira. Herschel-ATLAS and ALMA. HATLAS J142935.3-002836, a lensed major merger at redshift 1.027. A&A, 568:A92, August 2014. doi: 10.1051/0004-6361/201424410.

J. A. Calanog, H. Fu, A. Cooray, J. Wardlow, B. Ma, S. Amber, A. J. Baker, M. Baes, J. Bock, N. Bourne, R. S. Bussmann, C. M. Casey, S. C. Chapman, D. L. Clements, A. Conley, H. Dannerbauer, G. De Zotti, L. Dunne, S. Dye, S. Eales, D. Farrah, C. Furlanetto, A. I. Harris, R. J. Ivison, S. Kim, S. J. Maddox, G. Magdis, H. Messias, M. J. Michałowski, M. Negrello, J. Nightingale, J. M. O'Bryan, S. J. Oliver, D. Riechers, D. Scott, S. Serjeant, J. Simpson, M. Smith, N. Timmons, C. Thacker, E. Valiante, and J. D. Vieira. Lens Models of Herschel-selected Galaxies from High-resolution Near-IR Observations. ApJ, 797:138, December 2014. doi: 10.1088/0004-637X/797/2/138.

R. J. Ivison, A. M. Swinbank, I. Smail, A. I. Harris, R. S. Bussmann, A. Cooray, P. Cox, H. Fu, A. Kovács, M. Krips, D. Narayanan, M. Negrello, R. Neri, J. Peñarrubia, J. Richard, D. A. Riechers, K. Rowlands, J. G. Staguhn, T. A. Targett, S. Amber, A. J. Baker, N. Bourne, F. Bertoldi, M. Bremer, J. A. Calanog, D. L. Clements, H. Dannerbauer, A. Dariush, G. De Zotti, L. Dunne, S. A. Eales, D. Farrah, S. Fleuren, A. Franceschini, J. E. Geach, R. D. George, J. C. Helly,

R. Hopwood, E. Ibar, M. J. Jarvis, J.-P. Kneib, S. Maddox, A. Omont, D. Scott, S. Serjeant, M. W. L. Smith, M. A. Thompson, E. Valiante, I. Valtchanov, J. Vieira, and P. van der Werf. Herschel-ATLAS: A Binary HyLIRG Pinpointing a Cluster of Starbursting Protoellipticals. ApJ, 772:137, August 2013. doi: 10.1088/0004-637X/772/2/137.

ALMA Partnership, C. Vlahakis, T. R. Hunter, J. A. Hodge, L. M. Pérez, P. Andreani, C. L. Brogan, P. Cox, S. Martin, M. Zwaan, S. Matsushita, W. R. F. Dent, C. M. V. Impellizzeri, E. B. Fomalont, Y. Asaki, D. Barkats, R. E. Hills, A. Hirota, R. Kneissl, E. Liuzzo, R. Lucas, N. Marcelino, K. Nakanishi, N. Phillips, A. M. S. Richards, I. Toledo, R. Aladro, D. Broguiere, J. R. Cortes, P. C. Cortes, D. Espada, F. Galarza, D. Garcia-Appadoo, L. Guzman-Ramirez, A. S. Hales, E. M. Humphreys, T. Jung, S. Kameno, R. A. Laing, S. Leon, G. Marconi, A. Mignano, B. Nikolic, L.-A. Nyman, M. Radiszcz, A. Remijan, J. A. Rodón, T. Sawada, S. Takahashi, R. P. J. Tilanus, B. Vila Vilaro, L. C. Watson, T. Wiklind, Y. Ao, J. Di Francesco, B. Hatsukade, E. Hatziminaoglou, J. Mangum, Y. Matsuda, E. van Kampen, A. Wootten, I. de Gregorio-Monsalvo, G. Dumas, H. Francke, J. Gallardo, J. Garcia, S. Gonzalez, T. Hill, D. Iono, T. Kaminski, A. Karim, M. Krips, Y. Kurono, C. Lonsdale, C. Lopez, F. Morales, K. Plarre, L. Videla, E. Villard, J. E. Hibbard, and K. Tatematsu. The 2014 ALMA Long Baseline Campaign: Observations of the Strongly Lensed Submillimeter Galaxy HATLAS J090311.6+003906 at z = 3.042. ApJ, 808:L4, July 2015. doi: 10.1088/2041-8205/808/1/L4.

J. W. Nightingale and S. Dye. Adaptive semi-linear inversion of strong gravitational lens imaging. MNRAS, 452:2940–2959, September 2015. doi: 10.1093/mnras/stv1455.

S. H. Suyu, P. J. Marshall, M. P. Hobson, and R. D. Blandford. A Bayesian analysis of regularized source inversions in gravitational lensing. MNRAS, 371:983–998, September 2006. doi: 10.1111/j.1365-2966.2006.10733.x.

C. R. Keeton. GRAVLENS: Computational Methods for Gravitational Lensing. Astrophysics Source Code Library, February 2011.

M. Oguri. The Mass Distribution of SDSS J1004+4112 Revisited. *Publications of the Astronomical Society of Japan*, 62:1017–, August 2010. doi: 10.1093/pasj/62.4.1017.

M. Negrello, S. Amber, A. Amvrosiadis, Z.-Y. Cai, A. Lapi, J. Gonzalez-Nuevo, G. De Zotti, C. Furlanetto, S. J. Maddox, M. Allen, T. Bakx, R. S. Bussmann, A. Cooray, G. Covone, L. Danese, H. Dannerbauer, H. Fu, J. Greenslade,

M. Gurwell, R. Hopwood, L. V. E. Koopmans, N. Napolitano, H. Nayyeri, A. Omont, C. E. Petrillo, D. A. Riechers, S. Serjeant, C. Tortora, E. Valiante, G. Verdoes Kleijn, G. Vernardos, J. L. Wardlow, M. Baes, A. J. Baker, N. Bourne, D. Clements, S. M. Crawford, S. Dye, L. Dunne, S. Eales, R. J. Ivison, L. Marchetti, M. J. Michałowski, M. W. L. Smith, M. Vaccari, and P. van der Werf. The Herschel-ATLAS: a sample of 500 μm-selected lensed galaxies over 600 deg^2. MNRAS, 465:3558–3580, March 2017. doi: 10.1093/mnras/stw2911.

J. L. Wardlow, A. Cooray, F. De Bernardis, A. Amblard, V. Arumugam, H. Aussel, A. J. Baker, M. Béthermin, R. Blundell, J. Bock, A. Boselli, C. Bridge, V. Buat, D. Burgarella, R. S. Bussmann, A. Cabrera-Lavers, J. Calanog, J. M. Carpenter, C. M. Casey, N. Castro-Rodríguez, A. Cava, P. Chanial, E. Chapin, S. C. Chapman, D. L. Clements, A. Conley, P. Cox, C. D. Dowell, S. Dye, S. Eales, D. Farrah, P. Ferrero, A. Franceschini, D. T. Frayer, C. Frazer, H. Fu, R. Gavazzi, J. Glenn, E. A. González Solares, M. Griffin, M. A. Gurwell, A. I. Harris, E. Hatziminaoglou, R. Hopwood, A. Hyde, E. Ibar, R. J. Ivison, S. Kim, G. Lagache, L. Levenson, L. Marchetti, G. Marsden, P. Martinez-Navajas, M. Negrello, R. Neri, H. T. Nguyen, B. O'Halloran, S. J. Oliver, A. Omont, M. J. Page, P. Panuzzo, A. Papageorgiou, C. P. Pearson, I. Pérez-Fournon, M. Pohlen, D. Riechers, D. Rigopoulou, I. G. Roseboom, M. Rowan-Robinson, B. Schulz, D. Scott, N. Scoville, N. Seymour, D. L. Shupe, A. J. Smith, A. Streblyanska, A. Strom, M. Symeonidis, M. Trichas, M. Vaccari, J. D. Vieira, M. Viero, L. Wang, C. K. Xu, L. Yan, and M. Zemcov. HerMES: Candidate Gravitationally Lensed Galaxies and Lensing Statistics at Submillimeter Wavelengths. ApJ, 762:59, January 2013. doi: 10.1088/0004-637X/762/1/59.

J. D. Vieira, D. P. Marrone, S. C. Chapman, C. De Breuck, Y. D. Hezaveh, A. Weiβ, J. E. Aguirre, K. A. Aird, M. Aravena, M. L. N. Ashby, M. Bayliss, B. A. Benson, A. D. Biggs, L. E. Bleem, J. J. Bock, M. Bothwell, C. M. Bradford, M. Brodwin, J. E. Carlstrom, C. L. Chang, T. M. Crawford, A. T. Crites, T. de Haan, M. A. Dobbs, E. B. Fomalont, C. D. Fassnacht, E. M. George, M. D. Gladders, A. H. Gonzalez, T. R. Greve, B. Gullberg, N. W. Halverson, F. W. High, G. P. Holder, W. L. Holzapfel, S. Hoover, J. D. Hrubes, T. R. Hunter, R. Keisler, A. T. Lee, E. M. Leitch, M. Lueker, D. Luong-van, M. Malkan, V. McIntyre, J. J. McMahon, J. Mehl, K. M. Menten, S. S. Meyer, L. M. Mocanu, E. J. Murphy, T. Natoli, S. Padin, T. Plagge, C. L. Reichardt, A. Rest, J. Ruel, J. E. Ruhl, K. Sharon, K. K. Schaffer, L. Shaw, E. Shirokoff, J. S. Spilker, B. Stalder, Z. Staniszewski, A. A. Stark, K. Story, K. Vanderlinde, N. Welikala, and R. Williamson. Dusty starburst galaxies in the early Universe as revealed by gravitational lensing. Nature, 495:

344–347, March 2013. doi: 10.1038/nature12001.

Planck Collaboration, N. Aghanim, B. Altieri, M. Arnaud, M. Ashdown, J. Aumont, C. Baccigalupi, A. J. Banday, R. B. Barreiro, N. Bartolo, E. Battaner, A. Beelen, K. Benabed, A. Benoit-Lévy, J.-P. Bernard, M. Bersanelli, M. Bethermin, P. Bielewicz, L. Bonavera, J. R. Bond, J. Borrill, F. R. Bouchet, F. Boulanger, C. Burigana, E. Calabrese, R. Canameras, J.-F. Cardoso, A. Catalano, A. Chamballu, R.-R. Chary, H. C. Chiang, P. R. Christensen, D. L. Clements, S. Colombi, F. Couchot, B. P. Crill, A. Curto, L. Danese, K. Dassas, R. D. Davies, R. J. Davis, P. de Bernardis, A. de Rosa, G. de Zotti, J. Delabrouille, J. M. Diego, H. Dole, S. Donzelli, O. Doré, M. Douspis, A. Ducout, X. Dupac, G. Efstathiou, F. Elsner, T. A. Enßlin, E. Falgarone, I. Flores-Cacho, O. Forni, M. Frailis, A. A. Fraisse, E. Franceschi, A. Frejsel, B. Frye, S. Galeotta, S. Galli, K. Ganga, M. Giard, E. Gjerløw, J. González-Nuevo, K. M. Górski, A. Gregorio, A. Gruppuso, D. Guéry, F. K. Hansen, D. Hanson, D. L. Harrison, G. Helou, C. Hernández-Monteagudo, S. R. Hildebrandt, E. Hivon, M. Hobson, W. A. Holmes, W. Hovest, K. M. Huffenberger, G. Hurier, A. H. Jaffe, T. R. Jaffe, E. Keihänen, R. Keskitalo, T. S. Kisner, R. Kneissl, J. Knoche, M. Kunz, H. Kurki-Suonio, G. Lagache, J.-M. Lamarre, A. Lasenby, M. Lattanzi, C. R. Lawrence, E. Le Floc'h, R. Leonardi, F. Levrier, M. Liguori, P. B. Lilje, M. Linden-Vørnle, M. López-Caniego, P. M. Lubin, J. F. Macías-Pérez, T. MacKenzie, B. Maffei, N. Mandolesi, M. Maris, P. G. Martin, C. Martinache, E. Martínez-González, S. Masi, S. Matarrese, P. Mazzotta, A. Melchiorri, A. Mennella, M. Migliaccio, A. Moneti, L. Montier, G. Morgante, D. Mortlock, D. Munshi, J. A. Murphy, P. Natoli, M. Negrello, N. P. H. Nesvadba, D. Novikov, I. Novikov, A. Omont, L. Pagano, F. Pajot, F. Pasian, O. Perdereau, L. Perotto, F. Perrotta, V. Pettorino, F. Piacentini, M. Piat, S. Plaszczynski, E. Pointecouteau, G. Polenta, L. Popa, G. W. Pratt, S. Prunet, J.-L. Puget, J. P. Rachen, W. T. Reach, M. Reinecke, M. Remazeilles, C. Renault, I. Ristorcelli, G. Rocha, G. Roudier, B. Rusholme, M. Sandri, D. Santos, G. Savini, D. Scott, L. D. Spencer, V. Stolyarov, R. Sunyaev, D. Sutton, J.-F. Sygnet, J. A. Tauber, L. Terenzi, L. Toffolatti, M. Tomasi, M. Tristram, M. Tucci, G. Umana, L. Valenziano, J. Valiviita, I. Valtchanov, B. Van Tent, J. D. Vieira, P. Vielva, L. A. Wade, B. D. Wandelt, I. K. Wehus, N. Welikala, A. Zacchei, and A. Zonca. Planck intermediate results. XXVII. High-redshift infrared galaxy overdensity candidates and lensed sources discovered by Planck and confirmed by Herschel-SPIRE. A&A, 582:A30, October 2015. doi: 10.1051/0004-6361/201424790.

H. Nayyeri, M. Keele, A. Cooray, D. A. Riechers, R. J. Ivison, A. I. Harris, D. T.

Frayer, A. J. Baker, S. C. Chapman, S. Eales, D. Farrah, H. Fu, L. Marchetti, R. Marques-Chaves, P. I. Martinez-Navajas, S. J. Oliver, A. Omont, I. Perez-Fournon, D. Scott, M. Vaccari, J. Vieira, M. Viero, L. Wang, and J. Wardlow. Candidate Gravitationally Lensed Dusty Star-forming Galaxies in the Herschel Wide Area Surveys. ApJ, 823:17, May 2016. doi: 10.3847/0004-637X/823/1/17.

J. E. Carlstrom, P. A. R. Ade, K. A. Aird, B. A. Benson, L. E. Bleem, S. Busetti, C. L. Chang, E. Chauvin, H.-M. Cho, T. M. Crawford, A. T. Crites, M. A. Dobbs, N. W. Halverson, S. Heimsath, W. L. Holzapfel, J. D. Hrubes, M. Joy, R. Keisler, T. M. Lanting, A. T. Lee, E. M. Leitch, J. Leong, W. Lu, M. Lueker, D. Luong-Van, J. J. McMahon, J. Mehl, S. S. Meyer, J. J. Mohr, T. E. Montroy, S. Padin, T. Plagge, C. Pryke, J. E. Ruhl, K. K. Schaffer, D. Schwan, E. Shirokoff, H. G. Spieler, Z. Staniszewski, A. A. Stark, C. Tucker, K. Vanderlinde, J. D. Vieira, and R. Williamson. The 10 Meter South Pole Telescope. PASP, 123:568, May 2011. doi: 10.1086/659879.

R. Cañameras, N. P. H. Nesvadba, D. Guery, T. McKenzie, S. König, G. Petitpas, H. Dole, B. Frye, I. Flores-Cacho, L. Montier, M. Negrello, A. Beelen, F. Boone, D. Dicken, G. Lagache, E. Le Floc'h, B. Altieri, M. Béthermin, R. Chary, G. de Zotti, M. Giard, R. Kneissl, M. Krips, S. Malhotra, C. Martinache, A. Omont, E. Pointecouteau, J.-L. Puget, D. Scott, G. Soucail, I. Valtchanov, N. Welikala, and L. Yan. Planck's dusty GEMS: The brightest gravitationally lensed galaxies discovered with the Planck all-sky survey. A&A, 581:A105, September 2015. doi: 10.1051/0004-6361/201425128.

I. Valtchanov, J. Virdee, R. J. Ivison, B. Swinyard, P. van der Werf, D. Rigopoulou, E. da Cunha, R. Lupu, D. J. Benford, D. Riechers, I. Smail, M. Jarvis, C. Pearson, H. Gomez, R. Hopwood, B. Altieri, M. Birkinshaw, D. Coia, L. Conversi, A. Cooray, G. de Zotti, L. Dunne, D. Frayer, L. Leeuw, A. Marston, M. Negrello, M. S. Portal, D. Scott, M. A. Thompson, M. Vaccari, M. Baes, D. Clements, M. J. Michałowski, H. Dannerbauer, S. Serjeant, R. Auld, S. Buttiglione, A. Cava, A. Dariush, S. Dye, S. Eales, J. Fritz, E. Ibar, S. Maddox, E. Pascale, M. Pohlen, E. Rigby, G. Rodighiero, D. J. B. Smith, P. Temi, J. Carpenter, A. Bolatto, M. Gurwell, and J. D. Vieira. Physical conditions of the interstellar medium of high-redshift, strongly lensed submillimetre galaxies from the Herschel-ATLAS. MNRAS, 415:3473–3484, August 2011. doi: 10.1111/j.1365-2966.2011.18959.x.

R. E. Lupu, K. S. Scott, J. E. Aguirre, I. Aretxaga, R. Auld, E. Barton, A. Beelen, F. Bertoldi, J. J. Bock, D. Bonfield, C. M. Bradford, S. Buttiglione, A. Cava, D. L.

Clements, J. Cooke, A. Cooray, H. Dannerbauer, A. Dariush, G. De Zotti, L. Dunne, S. Dye, S. Eales, D. Frayer, J. Fritz, J. Glenn, D. H. Hughes, E. Ibar, R. J. Ivison, M. J. Jarvis, J. Kamenetzky, S. Kim, G. Lagache, L. Leeuw, S. Maddox, P. R. Maloney, H. Matsuhara, E. J. Murphy, B. J. Naylor, M. Negrello, H. Nguyen, A. Omont, E. Pascale, M. Pohlen, E. Rigby, G. Rodighiero, S. Serjeant, D. Smith, P. Temi, M. Thompson, I. Valtchanov, A. Verma, J. D. Vieira, and J. Zmuidzinas. Measurements of CO Redshifts with Z-Spec for Lensed Submillimeter Galaxies Discovered in the H-ATLAS Survey. ApJ, 757:135, October 2012. doi: 10.1088/0004-637X/757/2/135.

A. I. Harris, A. J. Baker, D. T. Frayer, I. Smail, A. M. Swinbank, D. A. Riechers, P. P. van der Werf, R. Auld, M. Baes, R. S. Bussmann, S. Buttiglione, A. Cava, D. L. Clements, A. Cooray, H. Dannerbauer, A. Dariush, G. De Zotti, L. Dunne, S. Dye, S. Eales, J. Fritz, J. González-Nuevo, R. Hopwood, E. Ibar, R. J. Ivison, M. J. Jarvis, S. Maddox, M. Negrello, E. Rigby, D. J. B. Smith, P. Temi, and J. Wardlow. Blind Detections of CO J = 1-0 in 11 H-ATLAS Galaxies at z = 2.1-3.5 with the GBT/Zpectrometer. ApJ, 752:152, June 2012. doi: 10.1088/0004-637X/752/2/152.

A. Omont, R. Neri, P. Cox, R. Lupu, M. Guélin, P. van der Werf, A. Weiß, R. Ivison, M. Negrello, L. Leeuw, M. Lehnert, I. Smail, A. Verma, A. J. Baker, A. Beelen, J. E. Aguirre, M. Baes, F. Bertoldi, D. L. Clements, A. Cooray, K. Coppin, H. Dannerbauer, G. de Zotti, S. Dye, N. Fiolet, D. Frayer, R. Gavazzi, D. Hughes, M. Jarvis, M. Krips, M. J. Michałowski, E. J. Murphy, D. Riechers, S. Serjeant, A. M. Swinbank, P. Temi, M. Vaccari, J. D. Vieira, R. Auld, B. Buttiglione, A. Cava, A. Dariush, L. Dunne, S. A. Eales, J. Fritz, H. Gomez, E. Ibar, S. Maddox, E. Pascale, M. Pohlen, E. Rigby, D. J. B. Smith, J. Bock, C. M. Bradford, J. Glenn, K. S. Scott, and J. Zmuidzinas. Observation of H_2O in a strongly lensed Herschel-ATLAS source at z = 2.3. A&A, 530:L3, June 2011. doi: 10.1051/0004-6361/201116921.

A. Omont, C. Yang, P. Cox, R. Neri, A. Beelen, R. S. Bussmann, R. Gavazzi, P. van der Werf, D. Riechers, D. Downes, M. Krips, S. Dye, R. Ivison, J. D. Vieira, A. Weiß, J. E. Aguirre, M. Baes, A. J. Baker, F. Bertoldi, A. Cooray, H. Dannerbauer, G. De Zotti, S. A. Eales, H. Fu, Y. Gao, M. Guélin, A. I. Harris, M. Jarvis, M. Lehnert, L. Leeuw, R. Lupu, K. Menten, M. J. Michałowski, M. Negrello, S. Serjeant, P. Temi, R. Auld, A. Dariush, L. Dunne, J. Fritz, R. Hopwood, C. Hoyos, E. Ibar, S. Maddox, M. W. L. Smith, E. Valiante, J. Bock, C. M. Bradford, J. Glenn, and K. S. Scott. H_2O emission in high-z ultra-luminous infrared galaxies. A&A, 551:A115, March 2013. doi:

10.1051/0004-6361/201220811.

I. Oteo, Z. Zhang, C. Yang, R. J. Ivison, A. Omont, M. Bremer, S. Bussmann, A. Cooray, P. Cox, H. Dannerbauer, L. Dunne, S. Eales, C. Furlanetto, R. Gavazzi, H. Nayyeri, M. Negrello, R. Neri, D. Riechers, and P. Van der Werf. High dense gas fraction in intensely star-forming dusty galaxies at high redshift. *ArXiv e-prints*, January 2017a.

C. Yang, A. Omont, A. Beelen, E. González-Alfonso, R. Neri, Y. Gao, P. van der Werf, A. Weiß, R. Gavazzi, N. Falstad, A. J. Baker, R. S. Bussmann, A. Cooray, P. Cox, H. Dannerbauer, S. Dye, M. Guélin, R. Ivison, M. Krips, M. Lehnert, M. J. Michałowski, D. A. Riechers, M. Spaans, and E. Valiante. Submillimeter H_2O and H_2O^+ emission in lensed ultra- and hyper-luminous infrared galaxies at z 2-4. A&A, 595:A80, November 2016. doi: 10.1051/0004-6361/201628160.

A. M. Swinbank, S. Dye, J. W. Nightingale, C. Furlanetto, I. Smail, A. Cooray, H. Dannerbauer, L. Dunne, S. Eales, R. Gavazzi, T. Hunter, R. J. Ivison, M. Negrello, I. Oteo-Gomez, R. Smit, P. van der Werf, and C. Vlahakis. ALMA Resolves the Properties of Star-forming Regions in a Dense Gas Disk at z 3. ApJ, 806:L17, June 2015. doi: 10.1088/2041-8205/806/1/L17.

M. Rybak, J. P. McKean, S. Vegetti, P. Andreani, and S. D. M. White. ALMA imaging of SDP.81 - I. A pixelated reconstruction of the far-infrared continuum emission. MNRAS, 451:L40–L44, July 2015. doi: 10.1093/mnrasl/slv058.

S. Dye, C. Furlanetto, A. M. Swinbank, C. Vlahakis, J. W. Nightingale, L. Dunne, S. A. Eales, I. Smail, I. Oteo, T. Hunter, M. Negrello, H. Dannerbauer, R. J. Ivison, R. Gavazzi, A. Cooray, and P. van der Werf. Revealing the complex nature of the strong gravitationally lensed system H-ATLAS J090311.6+003906 using ALMA. MNRAS, 452:2258–2268, September 2015. doi: 10.1093/mnras/stv1442.

S. Dye, N. W. Evans, V. Belokurov, S. J. Warren, and P. Hewett. Models of the Cosmic Horseshoe gravitational lens J1004+4112. MNRAS, 388:384–392, July 2008. doi: 10.1111/j.1365-2966.2008.13401.x.

S. Vegetti, D. J. Lagattuta, J. P. McKean, M. W. Auger, C. D. Fassnacht, and L. V. E. Koopmans. Gravitational detection of a low-mass dark satellite galaxy at cosmological distance. Nature, 481:341–343, January 2012. doi: 10.1038/nature10669.

S. Dye, M. Negrello, R. Hopwood, J. W. Nightingale, R. S. Bussmann, S. Amber, N. Bourne, A. Cooray, A. Dariush, L. Dunne, S. A. Eales, J. Gonzalez-Nuevo, E. Ibar, R. J. Ivison, S. Maddox, E. Valiante, and M. Smith. Herschel-ATLAS:

modelling the first strong gravitational lenses. MNRAS, 440:2013–2025, May 2014. doi: 10.1093/mnras/stu305.

S. Vegetti, L. V. E. Koopmans, M. W. Auger, T. Treu, and A. S. Bolton. Inference of the cold dark matter substructure mass function at z = 0.2 using strong gravitational lenses. MNRAS, 442:2017–2035, August 2014. doi: 10.1093/mnras/stu943.

A. Poglitsch, C. Waelkens, N. Geis, H. Feuchtgruber, B. Vandenbussche, L. Rodriguez, O. Krause, E. Renotte, C. van Hoof, P. Saraceno, J. Cepa, F. Kerschbaum, P. Agnèse, B. Ali, B. Altieri, P. Andreani, J.-L. Augueres, Z. Balog, L. Barl, O. H. Bauer, N. Belbachir, M. Benedettini, N. Billot, O. Boulade, H. Bischof, J. Blommaert, E. Callut, C. Cara, R. Cerulli, D. Cesarsky, A. Contursi, Y. Creten, W. De Meester, V. Doublier, E. Doumayrou, L. Duband, K. Exter, R. Genzel, J.-M. Gillis, U. Grözinger, T. Henning, J. Herreros, R. Huygen, M. Inguscio, G. Jakob, C. Jamar, C. Jean, J. de Jong, R. Katterloher, C. Kiss, U. Klaas, D. Lemke, D. Lutz, S. Madden, B. Marquet, J. Martignac, A. Mazy, P. Merken, F. Montfort, L. Morbidelli, T. Müller, M. Nielbock, K. Okumura, R. Orfei, R. Ottensamer, S. Pezzuto, P. Popesso, J. Putzeys, S. Regibo, V. Reveret, P. Royer, M. Sauvage, J. Schreiber, J. Stegmaier, D. Schmitt, J. Schubert, E. Sturm, M. Thiel, G. Tofani, R. Vavrek, M. Wetzstein, E. Wieprecht, and E. Wiezorrek. The Photodetector Array Camera and Spectrometer (PACS) on the Herschel Space Observatory. A&A, 518:L2, July 2010. doi: 10.1051/0004-6361/201014535.

M. J. Griffin, A. Abergel, A. Abreu, P. A. R. Ade, P. André, J.-L. Augueres, T. Babbedge, Y. Bae, T. Baillie, J.-P. Baluteau, M. J. Barlow, G. Bendo, D. Benielli, J. J. Bock, P. Bonhomme, D. Brisbin, C. Brockley-Blatt, M. Caldwell, C. Cara, N. Castro-Rodriguez, R. Cerulli, P. Chanial, S. Chen, E. Clark, D. L. Clements, L. Clerc, J. Coker, D. Communal, L. Conversi, P. Cox, D. Crumb, C. Cunningham, F. Daly, G. R. Davis, P. de Antoni, J. Delderfield, N. Devin, A. di Giorgio, I. Didschuns, K. Dohlen, M. Donati, A. Dowell, C. D. Dowell, L. Duband, L. Dumaye, R. J. Emery, M. Ferlet, D. Ferrand, J. Fontignie, M. Fox, A. Franceschini, M. Frerking, T. Fulton, J. Garcia, R. Gastaud, W. K. Gear, J. Glenn, A. Goizel, D. K. Griffin, T. Grundy, S. Guest, L. Guillemet, P. C. Hargrave, M. Harwit, P. Hastings, E. Hatziminaoglou, M. Herman, B. Hinde, V. Hristov, M. Huang, P. Imhof, K. J. Isaak, U. Israelsson, R. J. Ivison, D. Jennings, B. Kiernan, K. J. King, A. E. Lange, W. Latter, G. Laurent, P. Laurent, S. J. Leeks, E. Lellouch, L. Levenson, B. Li, J. Li, J. Lilienthal, T. Lim, S. J. Liu, N. Lu, S. Madden, G. Mainetti, P. Marliani, D. McKay, K. Mercier, S. Molinari,

H. Morris, H. Moseley, J. Mulder, M. Mur, D. A. Naylor, H. Nguyen, B. O'Halloran, S. Oliver, G. Olofsson, H.-G. Olofsson, R. Orfei, M. J. Page, I. Pain, P. Panuzzo, A. Papageorgiou, G. Parks, P. Parr-Burman, A. Pearce, C. Pearson, I. Pérez-Fournon, F. Pinsard, G. Pisano, J. Podosek, M. Pohlen, E. T. Polehampton, D. Pouliquen, D. Rigopoulou, D. Rizzo, I. G. Roseboom, H. Roussel, M. Rowan-Robinson, B. Rownd, P. Saraceno, M. Sauvage, R. Savage, G. Savini, E. Sawyer, C. Scharmberg, D. Schmitt, N. Schneider, B. Schulz, A. Schwartz, R. Shafer, D. L. Shupe, B. Sibthorpe, S. Sidher, A. Smith, A. J. Smith, D. Smith, L. Spencer, B. Stobie, R. Sudiwala, K. Sukhatme, C. Surace, J. A. Stevens, B. M. Swinyard, M. Trichas, T. Tourette, H. Triou, S. Tseng, C. Tucker, A. Turner, M. Vaccari, I. Valtchanov, L. Vigroux, E. Virique, G. Voellmer, H. Walker, R. Ward, T. Waskett, M. Weilert, R. Wesson, G. J. White, N. Whitehouse, C. D. Wilson, B. Winter, A. L. Woodcraft, G. S. Wright, C. K. Xu, A. Zavagno, M. Zemcov, L. Zhang, and E. Zonca. The Herschel-SPIRE instrument and its in-flight performance. A&A, 518:L3, July 2010. doi: 10.1051/0004-6361/201014519.

A. W. Blain. Galaxy-galaxy gravitational lensing in the millimetre/submillimetre waveband. MNRAS, 283:1340–1348, December 1996. doi: 10.1093/mnras/283.4.1340.

F. Perrotta, C. Baccigalupi, M. Bartelmann, G. De Zotti, and G. L. Granato. Gravitational lensing of extended high-redshift sources by dark matter haloes. MNRAS, 329:445–455, January 2002. doi: 10.1046/j.1365-8711.2002.05009.x.

F. Perrotta, M. Magliocchetti, C. Baccigalupi, M. Bartelmann, G. De Zotti, G. L. Granato, L. Silva, and L. Danese. Predictions for statistical properties of forming spheroidal galaxies. MNRAS, 338:623–636, January 2003. doi: 10.1046/j.1365-8711.2003.06072.x.

A. Lapi, F. Shankar, J. Mao, G. L. Granato, L. Silva, G. De Zotti, and L. Danese. Quasar Luminosity Functions from Joint Evolution of Black Holes and Host Galaxies. ApJ, 650:42–56, October 2006. doi: 10.1086/507122.

A. Lapi, J. González-Nuevo, L. Fan, A. Bressan, G. De Zotti, L. Danese, M. Negrello, L. Dunne, S. Eales, S. Maddox, R. Auld, M. Baes, D. G. Bonfield, S. Buttiglione, A. Cava, D. L. Clements, A. Cooray, A. Dariush, S. Dye, J. Fritz, D. Herranz, R. Hopwood, E. Ibar, R. Ivison, M. J. Jarvis, S. Kaviraj, M. López-Caniego, M. Massardi, M. J. Michałowski, E. Pascale, M. Pohlen, E. Rigby, G. Rodighiero, S. Serjeant, D. J. B. Smith, P. Temi, J. Wardlow, and P. van der Werf. Herschel-ATLAS Galaxy Counts and High-redshift Luminosity

Functions: The Formation of Massive Early-type Galaxies. ApJ, 742:24, November 2011. doi: 10.1088/0004-637X/742/1/24.

J. T. A. de Jong, G. A. Verdoes Kleijn, D. R. Boxhoorn, H. Buddelmeijer, M. Capaccioli, F. Getman, A. Grado, E. Helmich, Z. Huang, N. Irisarri, K. Kuijken, F. La Barbera, J. P. McFarland, N. R. Napolitano, M. Radovich, G. Sikkema, E. A. Valentijn, K. G. Begeman, M. Brescia, S. Cavuoti, A. Choi, O.-M. Cordes, G. Covone, M. Dall'Ora, H. Hildebrandt, G. Longo, R. Nakajima, M. Paolillo, E. Puddu, A. Rifatto, C. Tortora, E. van Uitert, A. Buddendiek, J. Harnois-Déraps, T. Erben, M. B. Eriksen, C. Heymans, H. Hoekstra, B. Joachimi, T. D. Kitching, D. Klaes, L. V. E. Koopmans, F. Köhlinger, N. Roy, C. Sifón, P. Schneider, W. J. Sutherland, M. Viola, and W.-J. Vriend. The first and second data releases of the Kilo-Degree Survey. A&A, 582:A62, October 2015. doi: 10.1051/0004-6361/201526601.

A. Edge, W. Sutherland, K. Kuijken, S. Driver, R. McMahon, S. Eales, and J. P. Emerson. The VISTA Kilo-degree Infrared Galaxy (VIKING) Survey: Bridging the Gap between Low and High Redshift. *The Messenger*, 154:32–34, December 2013.

A. Lawrence, S. J. Warren, O. Almaini, A. C. Edge, N. C. Hambly, R. F. Jameson, P. Lucas, M. Casali, A. Adamson, S. Dye, J. P. Emerson, S. Foucaud, P. Hewett, P. Hirst, S. T. Hodgkin, M. J. Irwin, N. Lodieu, R. G. McMahon, C. Simpson, I. Smail, D. Mortlock, and M. Folger. The UKIRT Infrared Deep Sky Survey (UKIDSS). MNRAS, 379:1599–1617, August 2007. doi: 10.1111/j.1365-2966.2007.12040.x.

B. Hatsukade, Y. Tamura, D. Iono, Y. Matsuda, M. Hayashi, and M. Oguri. High-resolution ALMA observations of SDP.81. II. Molecular clump properties of a lensed submillimeter galaxy at z = 3.042. PASJ, 67:93, October 2015. doi: 10.1093/pasj/psv061.

Y. Tamura, M. Oguri, D. Iono, B. Hatsukade, Y. Matsuda, and M. Hayashi. High-resolution ALMA observations of SDP.81. I. The innermost mass profile of the lensing elliptical galaxy probed by 30 milli-arcsecond images. PASJ, 67:72, August 2015. doi: 10.1093/pasj/psv040.

Y. D. Hezaveh, N. Dalal, D. P. Marrone, Y.-Y. Mao, W. Morningstar, D. Wen, R. D. Blandford, J. E. Carlstrom, C. D. Fassnacht, G. P. Holder, A. Kemball, P. J. Marshall, N. Murray, L. Perreault Levasseur, J. D. Vieira, and R. H. Wechsler. Detection of Lensing Substructure Using ALMA Observations of the Dusty Galaxy SDP.81. ApJ, 823:37, May 2016. doi: 10.3847/0004-637X/823/1/37.

R. Kormann, P. Schneider, and M. Bartelmann. Isothermal elliptical gravitational lens models. A&A, 284:285–299, April 1994.

M. Barnabè, O. Czoske, L. V. E. Koopmans, T. Treu, A. S. Bolton, and R. Gavazzi. Two-dimensional kinematics of SLACS lenses - II. Combined lensing and dynamics analysis of early-type galaxies at z = 0.08-0.33. MNRAS, 399:21–36, October 2009. doi: 10.1111/j.1365-2966.2009.14941.x.

S. Dye, C. Furlanetto, L. Dunne, S. A. Eales, M. Negrello, H. Nayyeri, P. P. van der Werf, S. Serjeant, D. Farrah, M. J. Michalowski, M. Baes, L. Marchetti, A. Cooray, and D. A. Riechers. Modelling ALMA observations of strong gravitational lenses detected by Herschel. *ArXiv e-prints*, May 2017.

E. E. Falco, M. V. Gorenstein, and I. I. Shapiro. On model-dependent bounds on H(0) from gravitational images Application of Q0957 + 561A,B. ApJ, 289: L1–L4, February 1985. doi: 10.1086/184422.

P. Schneider and D. Sluse. Source-position transformation: an approximate invariance in strong gravitational lensing. A&A, 564:A103, April 2014. doi: 10.1051/0004-6361/201322106.

P. Schneider and D. Sluse. Mass-sheet degeneracy, power-law models and external convergence: Impact on the determination of the Hubble constant from gravitational lensing. A&A, 559:A37, November 2013. doi: 10.1051/0004-6361/201321882.

F. Feroz and M. P. Hobson. Multimodal nested sampling: an efficient and robust alternative to Markov Chain Monte Carlo methods for astronomical data analyses. MNRAS, 384:449–463, February 2008. doi: 10.1111/j.1365-2966.2007.12353.x.

F. Feroz, M. P. Hobson, and M. Bridges. MULTINEST: an efficient and robust Bayesian inference tool for cosmology and particle physics. MNRAS, 398: 1601–1614, October 2009. doi: 10.1111/j.1365-2966.2009.14548.x.

John Skilling. Nested sampling for general bayesian computation. *Bayesian Anal.*, 1(4):833–859, 12 2006. doi: 10.1214/06-BA127. URL http://dx.doi.org/10.1214/06-BA127.

Y. D. Hezaveh, D. P. Marrone, C. D. Fassnacht, J. S. Spilker, J. D. Vieira, J. E. Aguirre, K. A. Aird, M. Aravena, M. L. N. Ashby, M. Bayliss, B. A. Benson, L. E. Bleem, M. Bothwell, M. Brodwin, J. E. Carlstrom, C. L. Chang, S. C. Chapman, T. M. Crawford, A. T. Crites, C. De Breuck, T. de Haan, M. A. Dobbs, E. B. Fomalont, E. M. George, M. D. Gladders, A. H. Gonzalez, T. R. Greve, N. W.

Halverson, F. W. High, G. P. Holder, W. L. Holzapfel, S. Hoover, J. D. Hrubes, K. Husband, T. R. Hunter, R. Keisler, A. T. Lee, E. M. Leitch, M. Lueker, D. Luong-Van, M. Malkan, V. McIntyre, J. J. McMahon, J. Mehl, K. M. Menten, S. S. Meyer, L. M. Mocanu, E. J. Murphy, T. Natoli, S. Padin, T. Plagge, C. L. Reichardt, A. Rest, J. Ruel, J. E. Ruhl, K. Sharon, K. K. Schaffer, L. Shaw, E. Shirokoff, B. Stalder, Z. Staniszewski, A. A. Stark, K. Story, K. Vanderlinde, A. Weiß, N. Welikala, and R. Williamson. ALMA Observations of SPT-discovered, Strongly Lensed, Dusty, Star-forming Galaxies. ApJ, 767:132, April 2013. doi: 10.1088/0004-637X/767/2/132.

M. Negrello, R. Hopwood, S. Dye, E. d. Cunha, S. Serjeant, J. Fritz, K. Rowlands, S. Fleuren, R. S. Bussmann, A. Cooray, H. Dannerbauer, J. Gonzalez-Nuevo, A. Lapi, A. Omont, S. Amber, R. Auld, M. Baes, S. Buttiglione, A. Cava, L. Danese, A. Dariush, G. De Zotti, L. Dunne, S. Eales, E. Ibar, R. J. Ivison, S. Kim, L. Leeuw, S. Maddox, M. J. Michałowski, M. Massardi, E. Pascale, M. Pohlen, E. Rigby, D. J. B. Smith, W. Sutherland, P. Temi, and J. Wardlow. Herschel *-ATLAS: deep HST/WFC3 imaging of strongly lensed submillimetre galaxies. MNRAS, 440:1999–2012, May 2014. doi: 10.1093/mnras/stu413.

K. C. Wong, T. Ishida, Y. Tamura, S. H. Suyu, M. Oguri, and S. Matsushita. ALMA Observations of the Gravitational Lens SDP.9. ApJ, 843:L35, July 2017. doi: 10.3847/2041-8213/aa7d4a.

M. Massardi, A. F. M. Enia, M. Negrello, C. Mancuso, A. Lapi, C. Vignali, R. Gilli, S. Burkutean, L. Danese, and G. D. Zotti. Chandra and ALMA observations of the nuclear activity in two strongly lensed star-forming galaxies. A&A, 610:A53, February 2018. doi: 10.1051/0004-6361/201731751.

P. Cox, M. Krips, R. Neri, A. Omont, R. Güsten, K. M. Menten, F. Wyrowski, A. Weiß, A. Beelen, M. A. Gurwell, H. Dannerbauer, R. J. Ivison, M. Negrello, I. Aretxaga, D. H. Hughes, R. Auld, M. Baes, R. Blundell, S. Buttiglione, A. Cava, A. Cooray, A. Dariush, L. Dunne, S. Dye, S. A. Eales, D. Frayer, J. Fritz, R. Gavazzi, R. Hopwood, E. Ibar, M. Jarvis, S. Maddox, M. Michałowski, E. Pascale, M. Pohlen, E. Rigby, D. J. B. Smith, A. M. Swinbank, P. Temi, I. Valtchanov, P. van der Werf, and G. de Zotti. Gas and Dust in a Submillimeter Galaxy at z = 4.24 from the Herschel Atlas. ApJ, 740:63, October 2011. doi: 10.1088/0004-637X/740/2/63.

J. M. Simpson, I. Smail, A. M. Swinbank, S. C. Chapman, J. E. Geach, R. J. Ivison, A. P. Thomson, I. Aretxaga, A. W. Blain, W. I. Cowley, C.-C. Chen, K. E. K. Coppin, J. S. Dunlop, A. C. Edge, D. Farrah, E. Ibar, A. Karim, K. K. Knudsen, R. Meijerink, M. J. Michałowski, D. Scott, M. Spaans, and P. P. van der Werf. The

SCUBA-2 Cosmology Legacy Survey: ALMA Resolves the Bright-end of the Sub-millimeter Number Counts. ApJ, 807:128, July 2015. doi: 10.1088/0004-637X/807/2/128.

R. S. Bussmann, D. Riechers, A. Fialkov, J. Scudder, C. C. Hayward, W. I. Cowley, J. Bock, J. Calanog, S. C. Chapman, A. Cooray, F. De Bernardis, D. Farrah, H. Fu, R. Gavazzi, R. Hopwood, R. J. Ivison, M. Jarvis, C. Lacey, A. Loeb, S. J. Oliver, I. Pérez-Fournon, D. Rigopoulou, I. G. Roseboom, D. Scott, A. J. Smith, J. D. Vieira, L. Wang, and J. Wardlow. HerMES: ALMA Imaging of Herschel-selected Dusty Star-forming Galaxies. ApJ, 812:43, October 2015. doi: 10.1088/0004-637X/812/1/43.

S. Ikarashi, R. J. Ivison, K. I. Caputi, I. Aretxaga, J. S. Dunlop, B. Hatsukade, D. H. Hughes, D. Iono, T. Izumi, R. Kawabe, K. Kohno, C. D. P. Lagos, K. Motohara, K. Nakanishi, K. Ohta, Y. Tamura, H. Umehata, G. W. Wilson, K. Yabe, and M. S. Yun. Compact Starbursts in z

3-6 Submillimeter Galaxies Revealed by ALMA. ApJ, 810:133, September 2015. doi: 10.1088/0004-637X/810/2/133.

J. A. Hodge, A. M. Swinbank, J. M. Simpson, I. Smail, F. Walter, D. M. Alexander, F. Bertoldi, A. D. Biggs, W. N. Brandt, S. C. Chapman, C. C. Chen, K. E. K. Coppin, P. Cox, H. Dannerbauer, A. C. Edge, T. R. Greve, R. J. Ivison, A. Karim, K. K. Knudsen, K. M. Menten, H.-W. Rix, E. Schinnerer, J. L. Wardlow, A. Weiss, and P. van der Werf. Kiloparsec-scale Dust Disks in High-redshift Luminous Submillimeter Galaxies. ApJ, 833:103, December 2016. doi: 10.3847/1538-4357/833/1/103.

I. Oteo, R. J. Ivison, M. Negrello, I. Smail, I. Pérez-Fournon, M. Bremer, G. De Zotti, S. A. Eales, D. Farrah, P. Temi, D. L. Clements, A. Cooray, H. Dannerbauer, S. Duivenvoorden, L. Dunne, E. Ibar, A. J. R. Lewis, R. Marques-Chaves, P. Martínez-Navajas, M. J. Michałowski, A. Omont, S. Oliver, D. Riechers, D. Scott, and P. van der Werf. Witnessing the birth of the red sequence: the physical scale and morphology of dust emission in hyper-luminous starbursts in the early Universe. *ArXiv e-prints*, September 2017b.

T. A. Thompson, E. Quataert, and N. Murray. Radiation Pressure-supported Starburst Disks and Active Galactic Nucleus Fueling. ApJ, 630:167–185, September 2005. doi: 10.1086/431923.

B. H. Andrews and T. A. Thompson. Radiation Pressure Feedback in Galaxies. In M. Röllig, R. Simon, V. Ossenkopf, and J. Stutzki, editors, *EAS Publications*

Series, volume 52 of *EAS Publications Series*, pages 275–276, November 2011. doi: 10.1051/eas/1152045.

R. C. Kennicutt and N. J. Evans. Star Formation in the Milky Way and Nearby Galaxies. ARA&A, 50:531–608, September 2012. doi: 10.1146/annurev-astro-081811-125610.

S. J. Oliver, J. Bock, B. Altieri, A. Amblard, V. Arumugam, H. Aussel, T. Babbedge, A. Beelen, M. Béthermin, A. Blain, A. Boselli, C. Bridge, D. Brisbin, V. Buat, D. Burgarella, N. Castro-Rodríguez, A. Cava, P. Chanial, M. Cirasuolo, D. L. Clements, A. Conley, L. Conversi, A. Cooray, C. D. Dowell, E. N. Dubois, E. Dwek, S. Dye, S. Eales, D. Elbaz, D. Farrah, A. Feltre, P. Ferrero, N. Fiolet, M. Fox, A. Franceschini, W. Gear, E. Giovannoli, J. Glenn, Y. Gong, E. A. González Solares, M. Griffin, M. Halpern, M. Harwit, E. Hatziminaoglou, S. Heinis, P. Hurley, H. S. Hwang, A. Hyde, E. Ibar, O. Ilbert, K. Isaak, R. J. Ivison, G. Lagache, E. Le Floc'h, L. Levenson, B. L. Faro, N. Lu, S. Madden, B. Maffei, G. Magdis, G. Mainetti, L. Marchetti, G. Marsden, J. Marshall, A. M. J. Mortier, H. T. Nguyen, B. O'Halloran, A. Omont, M. J. Page, P. Panuzzo, A. Papageorgiou, H. Patel, C. P. Pearson, I. Pérez-Fournon, M. Pohlen, J. I. Rawlings, G. Raymond, D. Rigopoulou, L. Riguccini, D. Rizzo, G. Rodighiero, I. G. Roseboom, M. Rowan-Robinson, M. Sánchez Portal, B. Schulz, D. Scott, N. Seymour, D. L. Shupe, A. J. Smith, J. A. Stevens, M. Symeonidis, M. Trichas, K. E. Tugwell, M. Vaccari, I. Valtchanov, J. D. Vieira, M. Viero, L. Vigroux, L. Wang, R. Ward, J. Wardlow, G. Wright, C. K. Xu, and M. Zemcov. The Herschel Multi-tiered Extragalactic Survey: HerMES. MNRAS, 424:1614–1635, August 2012. doi: 10.1111/j.1365-2966.2012.20912.x.

A. Karim, A. M. Swinbank, J. A. Hodge, I. R. Smail, F. Walter, A. D. Biggs, J. M. Simpson, A. L. R. Danielson, D. M. Alexander, F. Bertoldi, C. de Breuck, S. C. Chapman, K. E. K. Coppin, H. Dannerbauer, A. C. Edge, T. R. Greve, R. J. Ivison, K. K. Knudsen, K. M. Menten, E. Schinnerer, J. L. Wardlow, A. Weiß, and P. van der Werf. An ALMA survey of submillimetre galaxies in the Extended Chandra Deep Field South: high-resolution 870 μm source counts. MNRAS, 432:2–9, June 2013. doi: 10.1093/mnras/stt196.

J. A. Hodge, A. Karim, I. Smail, A. M. Swinbank, F. Walter, A. D. Biggs, R. J. Ivison, A. Weiss, D. M. Alexander, F. Bertoldi, W. N. Brandt, S. C. Chapman, K. E. K. Coppin, P. Cox, A. L. R. Danielson, H. Dannerbauer, C. De Breuck, R. Decarli, A. C. Edge, T. R. Greve, K. K. Knudsen, K. M. Menten, H.-W. Rix, E. Schinnerer, J. M. Simpson, J. L. Wardlow, and P. van der Werf. An ALMA Survey of Submillimeter Galaxies in the Extended Chandra Deep Field South:

Source Catalog and Multiplicity. ApJ, 768:91, May 2013. doi: 10.1088/0004-637X/768/1/91.

I. Oteo, R. J. Ivison, L. Dunne, I. Smail, A. M. Swinbank, Z.-Y. Zhang, A. Lewis, S. Maddox, D. Riechers, S. Serjeant, P. Van der Werf, A. D. Biggs, M. Bremer, P. Cigan, D. L. Clements, A. Cooray, H. Dannerbauer, S. Eales, E. Ibar, H. Messias, M. J. Michałowski, I. Pérez-Fournon, and E. van Kampen. Witnessing the Birth of the Red Sequence: ALMA High-resolution Imaging of [C II] and Dust in Two Interacting Ultra-red Starbursts at z = 4.425. ApJ, 827:34, August 2016. doi: 10.3847/0004-637X/827/1/34.

D. A. Riechers, T. K. D. Leung, R. J. Ivison, I. Perez-Fournon, A. J. R. Lewis, R. Marques-Chaves, I. Oteo, D. L. Clements, A. Cooray, J. Greenslade, P. Martinez-Navajas, S. Oliver, D. Rigopoulou, D. Scott, and A. Weiss. Rise of the Titans: A Dusty, Hyper-Luminous "870 micron Riser" Galaxy at z~6. *ArXiv e-prints*, May 2017.

Y. Fudamoto, R. J. Ivison, I. Oteo, M. Krips, Z.-Y. Zhang, A. Weiss, H. Dannerbauer, A. Omont, S. C. Chapman, L. Christensen, V. Arumugam, F. Bertoldi, M. Bremer, D. L. Clements, L. Dunne, S. A. Eales, J. Greenslade, S. Maddox, P. Martinez-Navajas, M. Michalowski, I. Pérez-Fournon, D. Riechers, J. M. Simpson, B. Stalder, E. Valiante, and P. van der Werf. The most distant, luminous, dusty star-forming galaxies: redshifts from NOEMA and ALMA spectral scans. MNRAS, 472:2028–2041, December 2017. doi: 10.1093/mnras/stx1956.

E. Valiante, M. W. L. Smith, S. Eales, S. J. Maddox, E. Ibar, R. Hopwood, L. Dunne, P. J. Cigan, S. Dye, E. Pascale, E. E. Rigby, N. Bourne, C. Furlanetto, and R. J. Ivison. The Herschel-ATLAS data release 1 - I. Maps, catalogues and number counts. MNRAS, 462:3146–3179, November 2016. doi: 10.1093/mnras/stw1806.

I. Oteo, M. A. Zwaan, R. J. Ivison, I. Smail, and A. D. Biggs. ALMACAL II: Extreme Star Formation Rate Densities in Dusty Starbursts Revealed by ALMA 20 mas Resolution Imaging. ApJ, 837:182, March 2017c. doi: 10.3847/1538-4357/aa5da4.

A. Franceschini, G. Hasinger, T. Miyaji, and D. Malquori. On the relationship between galaxy formation and quasar evolution. MNRAS, 310:L5–L9, November 1999. doi: 10.1046/j.1365-8711.1999.03078.x.

D. Thomas, C. Maraston, R. Bender, and C. Mendes de Oliveira. The Epochs of Early-Type Galaxy Formation as a Function of Environment. ApJ, 621:673–694,

March 2005. doi: 10.1086/426932.

A. Gallazzi, E. F. Bell, S. Zibetti, J. Brinchmann, and D. D. Kelson. Charting the Evolution of the Ages and Metallicities of Massive Galaxies since z = 0.7. ApJ, 788:72, June 2014. doi: 10.1088/0004-637X/788/1/72.

M. Velander, E. van Uitert, H. Hoekstra, J. Coupon, T. Erben, C. Heymans, H. Hildebrandt, T. D. Kitching, Y. Mellier, L. Miller, L. Van Waerbeke, C. Bonnett, L. Fu, S. Giodini, M. J. Hudson, K. Kuijken, B. Rowe, T. Schrabback, and E. Semboloni. CFHTLenS: the relation between galaxy dark matter haloes and baryons from weak gravitational lensing. MNRAS, 437:2111–2136, January 2014. doi: 10.1093/mnras/stt2013.

M. J. Hudson, B. R. Gillis, J. Coupon, H. Hildebrandt, T. Erben, C. Heymans, H. Hoekstra, T. D. Kitching, Y. Mellier, L. Miller, L. Van Waerbeke, C. Bonnett, L. Fu, K. Kuijken, B. Rowe, T. Schrabback, E. Semboloni, E. van Uitert, and M. Velander. CFHTLenS: co-evolution of galaxies and their dark matter haloes. MNRAS, 447:298–314, February 2015. doi: 10.1093/mnras/stu2367.

R. Mandelbaum, W. Wang, Y. Zu, S. White, B. Henriques, and S. More. Strong bimodality in the host halo mass of central galaxies from galaxy-galaxy lensing. MNRAS, 457:3200–3218, April 2016. doi: 10.1093/mnras/stw188.

B. P. Moster, T. Naab, and S. D. M. White. EMERGE - an empirical model for the formation of galaxies since z
10. MNRAS, 477:1822–1852, June 2018. doi: 10.1093/mnras/sty655.

J. Kormendy and L. C. Ho. Coevolution (Or Not) of Supermassive Black Holes and Host Galaxies. ARA&A, 51:511–653, August 2013. doi: 10.1146/annurev-astro-082708-101811.

F. Shankar, M. Bernardi, R. K. Sheth, L. Ferrarese, A. W. Graham, G. Savorgnan, V. Allevato, A. Marconi, R. Läsker, and A. Lapi. Selection bias in dynamically measured supermassive black hole samples: its consequences and the quest for the most fundamental relation. MNRAS, 460:3119–3142, August 2016. doi: 10.1093/mnras/stw678.

R. C. E. van den Bosch. Unification of the fundamental plane and Super Massive Black Hole Masses. ApJ, 831:134, November 2016. doi: 10.3847/0004-637X/831/2/134.

V. Eke, G. Efstathiou, and L. Wright. The cosmological dependence of galactic specific angular momenta. MNRAS, 315:L18–L22, June 2000. doi: 10.1046/j.1365-8711.2000.03632.x.

S. M. Fall. Origin of Galactic Disks. In E. Athanassoula, A. Bosma, and R. Mujica, editors, *Disks of Galaxies: Kinematics, Dynamics and Peturbations*, volume 275 of *Astronomical Society of the Pacific Conference Series*, pages 389–396, December 2002.

A. J. Romanowsky and S. M. Fall. Angular Momentum and Galaxy Formation Revisited. ApJS, 203:17, December 2012. doi: 10.1088/0067-0049/203/2/17.

J. Shi, A. Lapi, C. Mancuso, H. Wang, and L. Danese. Angular Momentum of Early- and Late-type Galaxies: Nature or Nurture? ApJ, 843:105, July 2017. doi: 10.3847/1538-4357/aa7893.

D. Narayanan, M. Turk, R. Feldmann, T. Robitaille, P. Hopkins, R. Thompson, C. Hayward, D. Ball, C.-A. Faucher-Giguère, and D. Kereš. The formation of submillimetre-bright galaxies from gas infall over a billion years. Nature, 525: 496–499, September 2015. doi: 10.1038/nature15383.

A. Toomre. On the gravitational stability of a disk of stars. ApJ, 139:1217–1238, May 1964. doi: 10.1086/147861.

R. Genzel, N. M. Förster Schreiber, P. Lang, S. Tacchella, L. J. Tacconi, S. Wuyts, K. Bandara, A. Burkert, P. Buschkamp, C. M. Carollo, G. Cresci, R. Davies, F. Eisenhauer, E. K. S. Hicks, J. Kurk, S. J. Lilly, D. Lutz, C. Mancini, T. Naab, S. Newman, Y. Peng, A. Renzini, K. Shapiro Griffin, A. Sternberg, D. Vergani, E. Wisnioski, E. Wuyts, and G. Zamorani. The SINS/zC-SINF Survey of z ~ 2 Galaxy Kinematics: Evidence for Gravitational Quenching. ApJ, 785:75, April 2014. doi: 10.1088/0004-637X/785/1/75.

P. G. van Dokkum, E. J. Nelson, M. Franx, P. Oesch, I. Momcheva, G. Brammer, N. M. Förster Schreiber, R. E. Skelton, K. E. Whitaker, A. van der Wel, R. Bezanson, M. Fumagalli, G. D. Illingworth, M. Kriek, J. Leja, and S. Wuyts. Forming Compact Massive Galaxies. ApJ, 813:23, November 2015. doi: 10.1088/0004-637X/813/1/23.

G. Barro, M. Kriek, P. G. Pérez-González, J. R. Trump, D. C. Koo, S. M. Faber, A. Dekel, J. R. Primack, Y. Guo, D. D. Kocevski, J. C. Muñoz-Mateos, W. Rujopakarn, and K. Seth. Sub-kiloparsec ALMA Imaging of Compact Star-forming Galaxies at z ~ 2.5: Revealing the Formation of Dense Galactic Cores in the Progenitors of Compact Quiescent Galaxies. ApJ, 827:L32, August 2016. doi: 10.3847/2041-8205/827/2/L32.

G. Barro, M. Kriek, P. G. Pérez-González, T. Diaz-Santos, S. H. Price,

W. Rujopakarn, V. Pandya, D. C. Koo, S. M. Faber, A. Dekel, J. R. Primack, and

D. D. Kocevski. Spatially Resolved Kinematics in the Central 1 kpc of a Compact Star-forming Galaxy at z ~ 2.3 *fromALMACOObservations*. ApJ, 851 : *L*40, *December*2017. *doi* : .

M. Talia, F. Pozzi, L. Vallini, A. Cimatti, P. Cassata, F. Fraternali, M. Brusa, E. Daddi, I. Delvecchio, E. Ibar, E. Liuzzo, C. Vignali, M. Massardi, G. Zamorani, C. Gruppioni, A. Renzini, M. Mignoli, L. Pozzetti, and G. Rodighiero. ALMA view of a massive spheroid progenitor: a compact rotating core of molecular gas in an AGN host at z = 2.226. MNRAS, 476:3956–3963, May 2018. doi: 10.1093/mnras/sty481.

S. Dye, C. Furlanetto, L. Dunne, S. A. Eales, M. Negrello, H. Nayyeri, P. P. van der Werf, S. Serjeant, D. Farrah, M. J. Michałowski, M. Baes, L. Marchetti, A. Cooray, D. A. Riechers, and A. Amvrosiadis. Modelling high-resolution ALMA observations of strongly lensed highly star-forming galaxies detected by Herschel. MNRAS, 476:4383–4394, June 2018. doi: 10.1093/mnras/sty513.

M. Cappellari, R. M. McDermid, K. Alatalo, L. Blitz, M. Bois, F. Bournaud, M. Bureau, A. F. Crocker, R. L. Davies, T. A. Davis, P. T. de Zeeuw, P.-A. Duc, E. Emsellem, S. Khochfar, D. Krajnović, H. Kuntschner, R. Morganti, T. Naab, T. Oosterloo, M. Sarzi, N. Scott, P. Serra, A.-M. Weijmans, and L. M. Young. The ATLAS^{3D} project - XX. Mass-size and mass-σ distributions of early-type galaxies: bulge fraction drives kinematics, mass-to-light ratio, molecular gas fraction and stellar initial mass function. MNRAS, 432:1862–1893, July 2013. doi: 10.1093/mnras/stt644.

C. Ragone-Figueroa and G. L. Granato. Puffing up early-type galaxies by

baryonic mass loss: numerical experiments. MNRAS, 414:3690–3698, July 2011. doi: 10.1111/j.1365-2966.2011.18670.x.

A. B. Newman, S. Belli, and R. S. Ellis. Discovery of a Strongly Lensed Massive Quiescent Galaxy at z = 2.636: Spatially Resolved Spectroscopy and Indications of Rotation. ApJ, 813:L7, November 2015. doi: 10.1088/2041-8205/813/1/L7.

S. Belli, A. B. Newman, and R. S. Ellis. MOSFIRE Spectroscopy of Quiescent Galaxies at $1.5 < z < 2.5$. I. Evolution of Structural and Dynamical Properties. ApJ, 834:18, January 2017. doi: 10.3847/1538-4357/834/1/18.

K. Glazebrook, C. Schreiber, I. Labbé, T. Nanayakkara, G. G. Kacprzak, P. A. Oesch, C. Papovich, L. R. Spitler, C. M. S. Straatman, K.-V. H. Tran, and T. Yuan. A massive, quiescent galaxy at a redshift of 3.717. Nature, 544:71–74, April 2017. doi: 10.1038/nature21680.

S. Toft, J. Zabl, J. Richard, A. Gallazzi, S. Zibetti, M. Prescott, C. Grillo, A. W. S. Man, N. Y. Lee, C. Gómez-Guijarro, M. Stockmann, G. Magdis, and C. L. Steinhardt. A massive, dead disk galaxy in the early Universe. Nature, 546: 510–513, June 2017. doi: 10.1038/nature22388.

R. Hill, S. C. Chapman, D. Scott, G. Petitpas, I. Smail, E. L. Chapin, M. A. Gurwell, R. Perry, A. W. Blain, M. N. Bremer, C.-C. Chen, J. S. Dunlop, D. Farrah, G. G. Fazio, J. E. Geach, P. Howson, R. J. Ivison, K. Lacaille, M. J. Michałowski, J. M. Simpson, A. M. Swinbank, P. P. van der Werf, and D. J. Wilner. High-resolution SMA imaging of bright submillimetre sources from the SCUBA-2 Cosmology Legacy Survey. MNRAS, 477:2042–2067, June 2018.

doi: 10.1093/mnras/sty746.

R. Lange, S. P. Driver, A. S. G. Robotham, L. S. Kelvin, A. W. Graham, M. Alpaslan, S. K. Andrews, I. K. Baldry, S. Bamford, J. Bland-Hawthorn, S. Brough, M. E. Cluver, C. J. Conselice, L. J. M. Davies, B. Haeussler, I. S. Konstantopoulos, J. Loveday, A. J. Moffett, P. Norberg, S. Phillipps, E. N. Taylor, Á. R. López-Sánchez, and S. M. Wilkins. Galaxy And Mass Assembly (GAMA): mass-size relations of $z < 0.1$ galaxies subdivided by Sérsic index, colour and morphology. MNRAS, 447:2603–2630, March 2015. doi: 10.1093/mnras/stu2467.

M. Cappellari. Structure and Kinematics of Early-Type Galaxies from Integral Field Spectroscopy. ARA&A, 54:597–665, September 2016. doi: 10.1146/annurev-astro-082214-122432.

A. Lapi, S. Raimundo, R. Aversa, Z.-Y. Cai, M. Negrello, A. Celotti, G. De Zotti, and L. Danese. The Coevolution of Supermassive Black Holes and Massive Galaxies at High Redshift. ApJ, 782:69, February 2014. doi: 10.1088/0004-637X/782/2/69.

C. Mancuso, A. Lapi, I. Prandoni, I. Obi, J. Gonzalez-Nuevo, F. Perrotta, A. Bressan, A. Celotti, and L. Danese. Galaxy Evolution in the Radio Band: The Role of Star-forming Galaxies and Active Galactic Nuclei. ApJ, 842:95, June 2017. doi: 10.3847/1538-4357/aa745d.

G. Rodighiero, M. Brusa, E. Daddi, M. Negrello, J. R. Mullaney, I. Delvecchio, D. Lutz, A. Renzini, A. Franceschini, I. Baronchelli, F. Pozzi, C. Gruppioni,

V. Strazzullo, A. Cimatti, and J. Silverman. Relationship between Star Formation Rate and Black Hole Accretion At Z = 2: the Different Contributions in Quiescent, Normal, and Starburst Galaxies. ApJ, 800:L10, February 2015. doi: 10.1088/2041-8205/800/1/L10.

W. Rujopakarn, K. Nyland, G. H. Rieke, G. Barro, D. Elbaz, R. J. Ivison, P. Jagannathan, J. D. Silverman, V. Smolčić, and T. Wang. Cospatial Star Formation and Supermassive Black Hole Growth in $z\sim 3 Galaxies : Evidence for In Situ Co-evolution$. ApJ, 854 : L4, February 2018. doi : .

K.-i. Tadaki, T. Kodama, E. J. Nelson, S. Belli, N. M. Förster Schreiber, R. Genzel, M. Hayashi, R. Herrera-Camus, Y. Koyama, P. Lang, D. Lutz, R. Shimakawa, L. J. Tacconi, H. Übler, E. Wisnioski, S. Wuyts, B. Hatsukade, M. Lippa, K. Nakanishi, S. Ikarashi, K. Kohno, T. L. Suzuki, Y. Tamura, and I. Tanaka. Rotating Starburst Cores in Massive Galaxies at z = 2.5. ApJ, 841:L25, June 2017. doi: 10.3847/2041-8213/aa7338.

P. Kroupa. On the variation of the initial mass function. MNRAS, 322:231–246, April 2001. doi: 10.1046/j.1365-8711.2001.04022.x.

G. Rodighiero, E. Daddi, I. Baronchelli, A. Cimatti, A. Renzini, H. Aussel, P. Popesso, D. Lutz, P. Andreani, S. Berta, A. Cava, D. Elbaz, A. Feltre, A. Fontana, N. M. Förster Schreiber, A. Franceschini, R. Genzel, A. Grazian, C. Gruppioni, O. Ilbert, E. Le Floch, G. Magdis, M. Magliocchetti, B. Magnelli, R. Maiolino, H. McCracken, R. Nordon, A. Poglitsch, P. Santini, F. Pozzi, L. Riguccini, L. J. Tacconi, S. Wuyts, and G. Zamorani. The Lesser Role of Starbursts in Star Formation at z = 2. ApJ, 739:L40, October 2011. doi: 10.1088/2041-8205/739/2/L40.

G. Rodighiero, A. Renzini, E. Daddi, I. Baronchelli, S. Berta, G. Cresci, A. Franceschini, C. Gruppioni, D. Lutz, C. Mancini, P. Santini, G. Zamorani, J. Silverman, D. Kashino, P. Andreani, A. Cimatti, H. D. Sánchez, E. Le Floch, B. Magnelli, P. Popesso, and F. Pozzi. A multiwavelength consensus on the main sequence of star-forming galaxies at z
2. MNRAS, 443:19–30, September 2014. doi: 10.1093/mnras/stu1110.

D. M. Alexander, W. N. Brandt, I. Smail, A. M. Swinbank, F. E. Bauer, A. W. Blain, S. C. Chapman, K. E. K. Coppin, R. J. Ivison, and K. Menéndez-Delmestre. Weighing the Black Holes in z 2 Submillimeter-Emitting Galaxies Hosting Active

Galactic Nuclei. AJ, 135:1968–1981, May 2008. doi: 10.1088/0004-6256/135/5/1968.

D. M. Alexander and R. C. Hickox. What drives the growth of black holes? , 56: 93–121, June 2012. doi: 10.1016/j.newar.2011.11.003.

D. Kashino, S. More, J. D. Silverman, E. Daddi, A. Renzini, D. B. Sanders, G. Rodighiero, A. Puglisi, M. Kajisawa, F. Valentino, J. S. Kartaltepe, O. Le Fèvre, T. Nagao, N. Arimoto, and N. Sugiyama. The FMOS-COSMOS Survey of Star-forming Galaxies at Z

1.6. V: Properties of Dark Matter Halos Containing Hα Emitting Galaxies. ApJ, 843:138, July 2017. doi: 10.3847/1538-4357/aa789d.

J. D. Silverman, E. Daddi, G. Rodighiero, W. Rujopakarn, M. Sargent, A. Renzini, D. Liu, C. Feruglio, D. Kashino, D. Sanders, J. Kartaltepe, T. Nagao, N. Arimoto, S. Berta, M. Béthermin, A. Koekemoer, D. Lutz, G. Magdis, C. Mancini, M. Onodera, and G. Zamorani. A Higher Efficiency of Converting Gas to Stars Pushes Galaxies at z

1.6 Well Above the Star-forming Main Sequence. ApJ, 812:L23, October 2015. doi: 10.1088/2041-8205/812/2/L23.

T. Di Matteo, V. Springel, and L. Hernquist. Energy input from quasars regulates the growth and activity of black holes and their host galaxies. Nature, 433: 604–607, February 2005. doi: 10.1038/nature03335.

P. R. Capelo, M. Volonteri, M. Dotti, J. M. Bellovary, L. Mayer, and F. Governato. Growth and activity of black holes in galaxy mergers with varying mass ratios. MNRAS, 447:2123–2143, March 2015. doi: 10.1093/mnras/stu2500.

L. K. Steinborn, M. Hirschmann, K. Dolag, F. Shankar, S. Juneau, M. Krumpe, R.-S. Remus, and A. F. Teklu. Cosmological simulations of black hole growth II: how (in)significant are merger events for fuelling nuclear activity? *ArXiv e-prints*, May 2018.

I. Delvecchio, V. Smolčić, G. Zamorani, C. D. P. Lagos, S. Berta, J. Delhaize, N. Baran, D. M. Alexander, D. J. Rosario, V. Gonzalez-Perez, O. Ilbert, C. G. Lacey, O. Le Fèvre, O. Miettinen, M. Aravena, M. Bondi, C. Carilli, P. Ciliegi, K. Mooley, M. Novak, E. Schinnerer, P. Capak, F. Civano, N. Fanidakis, N. Herrera Ruiz, A. Karim, C. Laigle, S. Marchesi, H. J. McCracken, E. Middleberg, M. Salvato, and L. Tasca. The VLA-COSMOS 3 GHz Large Project: AGN and host-galaxy properties out to z 6. A&A, 602:A3, June 2017. doi: 10.1051/0004-6361/201629367.

E. Daddi, M. Dickinson, G. Morrison, R. Chary, A. Cimatti, D. Elbaz, D. Frayer, A. Renzini, A. Pope, D. M. Alexander, F. E. Bauer, M. Giavalisco, M. Huynh, J. Kurk, and M. Mignoli. Multiwavelength Study of Massive Galaxies at z~2. I. Star Formation and Galaxy Growth. ApJ, 670:156–172, November 2007. doi: 10.1086/521818.

J. Delhaize, V. Smolčić, I. Delvecchio, M. Novak, M. Sargent, N. Baran, B. Magnelli, G. Zamorani, E. Schinnerer, E. J. Murphy, M. Aravena, S. Berta, M. Bondi, P. Capak, C. Carilli, P. Ciliegi, F. Civano, O. Ilbert, A. Karim, C. Laigle, O. Le Fèvre, S. Marchesi, H. J. McCracken, M. Salvato, N. Seymour, and L. Tasca. The VLA-COSMOS 3 GHz Large Project: The infrared-radio correlation of star-forming galaxies and AGN to z 6. A&A, 602:A4, June 2017. doi: 10.1051/0004-6361/201629430.

C. Laigle, H. J. McCracken, O. Ilbert, B. C. Hsieh, I. Davidzon, P. Capak, G. Hasinger, J. D. Silverman, C. Pichon, J. Coupon, H. Aussel, D. Le Borgne, K. Caputi, P. Cassata, Y.-Y. Chang, F. Civano, J. Dunlop, J. Fynbo, J. S. Kartaltepe, A. Koekemoer, O. Le Fèvre, E. Le Floc'h, A. Leauthaud, S. Lilly, L. Lin, S. Marchesi, B. Milvang-Jensen, M. Salvato, D. B. Sanders, N. Scoville, V. Smolcic, M. Stockmann, Y. Taniguchi, L. Tasca, S. Toft, M. Vaccari, and J. Zabl. The COSMOS2015 Catalog: Exploring the $1 < z < 6$ Universe with Half a Million Galaxies. ApJS, 224:24, June 2016. doi: 10.3847/0067-0049/224/2/24.

E. da Cunha, S. Charlot, and D. Elbaz. A simple model to interpret the ultraviolet, optical and infrared emission from galaxies. MNRAS, 388: 1595–1617, August 2008. doi: 10.1111/j.1365-2966.2008.13535.x.

S. Berta, D. Lutz, P. Santini, S. Wuyts, D. Rosario, D. Brisbin, A. Cooray, A. Franceschini, C. Gruppioni, E. Hatziminaoglou, H. S. Hwang, E. Le Floc'h, B. Magnelli, R. Nordon, S. Oliver, M. J. Page, P. Popesso, L. Pozzetti, F. Pozzi, L. Riguccini, G. Rodighiero, I. Roseboom, D. Scott, M. Symeonidis, I. Valtchanov, M. Viero, and L. Wang. Panchromatic spectral energy distributions of Herschel sources. A&A, 551:A100, March 2013. doi: 10.1051/0004-6361/201220859.

A. Feltre, E. Hatziminaoglou, J. Fritz, and A. Franceschini. Smooth and clumpy dust distributions in AGN: a direct comparison of two commonly explored infrared emission models. MNRAS, 426:120–127, October 2012. doi: 10.1111/j.1365-2966.2012.21695.x.

J. Fritz, A. Franceschini, and E. Hatziminaoglou. Revisiting the infrared spectra of active galactic nuclei with a new torus emission model. MNRAS, 366: 767–786, March 2006. doi: 10.1111/j.1365-2966.2006.09866.x.

R. C. Kennicutt, Jr. Star Formation in Galaxies Along the Hubble Sequence. ARA&A, 36:189–232, 1998. doi: 10.1146/annurev.astro.36.1.189.

G. Chabrier. Galactic Stellar and Substellar Initial Mass Function. PASP, 115: 763–795, July 2003. doi: 10.1086/376392.

I. Delvecchio, C. Gruppioni, F. Pozzi, S. Berta, G. Zamorani, A. Cimatti, D. Lutz, D. Scott, C. Vignali, G. Cresci, A. Feltre, A. Cooray, M. Vaccari, J. Fritz, E. Le Floc'h, B. Magnelli, P. Popesso, S. Oliver, J. Bock, M. Carollo, T. Contini, O. Le Févre, S. Lilly, V. Mainieri, A. Renzini, and M. Scodeggio. Tracing the cosmic growth of supermassive black holes to z

3 with Herschel. MNRAS, 439:2736–2754, April 2014. doi: 10.1093/mnras/stu130.

A. Bongiorno, A. Merloni, M. Brusa, B. Magnelli, M. Salvato, M. Mignoli, G. Zamorani, F. Fiore, D. Rosario, V. Mainieri, H. Hao, A. Comastri, C. Vignali, I. Balestra, S. Bardelli, S. Berta, F. Civano, P. Kampczyk, E. Le Floc'h, E. Lusso, D. Lutz, L. Pozzetti, F. Pozzi, L. Riguccini, F. Shankar, and J. Silverman. Accreting supermassive black holes in the COSMOS field and the connection to their host galaxies. MNRAS, 427:3103–3133, December 2012. doi: 10.1111/j.1365-2966.2012.22089.x.

C. Gruppioni, S. Berta, L. Spinoglio, M. Pereira-Santaella, F. Pozzi, P. Andreani, M. Bonato, G. De Zotti, M. Malkan, M. Negrello, L. Vallini, and C. Vignali. Tracing black hole accretion with SED decomposition and IR lines: from local galaxies to the high-z Universe. MNRAS, 458:4297–4320, June 2016. doi: 10.1093/mnras/stw577.

S. Tacchella, A. Dekel, C. M. Carollo, D. Ceverino, C. DeGraf, S. Lapiner, N. Mandelker, and R. Primack Joel. The confinement of star-forming galaxies into a main sequence through episodes of gas compaction, depletion and replenishment. MNRAS, 457:2790–2813, April 2016. doi: 10.1093/mnras/stw131.

A. Puglisi, E. Daddi, A. Renzini, G. Rodighiero, J. D. Silverman, D. Kashino, L. Rodríguez-Muñoz, C. Mancini, V. Mainieri, A. Man, A. Franceschini, F. Valentino, A. Calabrò, S. Jin, B. Darvish, C. Maier, J. S. Kartaltepe, and D. B. Sanders. The Bright and Dark Sides of High-redshift Starburst Galaxies from Herschel and Subaru Observations. ApJ, 838:L18, April 2017. doi: 10.3847/2041-8213/aa66c9.

G. E. Magdis, E. Daddi, M. Béthermin, M. Sargent, D. Elbaz, M. Pannella, M. Dickinson, H. Dannerbauer, E. da Cunha, F. Walter, D. Rigopoulou,

V. Charmandaris, H. S. Hwang, and J. Kartaltepe. The Evolving Interstellar Medium of Star-forming Galaxies since z = 2 as Probed by Their Infrared Spectral Energy Distributions. ApJ, 760:6, November 2012. doi: 10.1088/0004-637X/760/1/6.

B. T. Draine and A. Li. Infrared Emission from Interstellar Dust. IV. The Silicate-Graphite-PAH Model in the Post-Spitzer Era. ApJ, 657:810–837, March 2007. doi: 10.1086/511055.

S. A. Eales, M. W. L. Smith, C. D. Wilson, G. J. Bendo, L. Cortese, M. Pohlen, A. Boselli, H. L. Gomez, R. Auld, M. Baes, M. J. Barlow, J. J. Bock, M. Bradford, V. Buat, N. Castro-Rodríguez, P. Chanial, S. Charlot, L. Ciesla, D. L. Clements, A. Cooray, D. Cormier, J. I. Davies, E. Dwek, D. Elbaz, M. Galametz, F. Galliano, W. K. Gear, J. Glenn, M. Griffin, S. Hony, K. G. Isaak, L. R. Levenson, N. Lu, S. Madden, B. O'Halloran, K. Okumura, S. Oliver, M. J. Page, P. Panuzzo, A. Papageorgiou, T. J. Parkin, I. Pérez-Fournon, N. Rangwala, E. E. Rigby, H. Roussel, A. Rykala, N. Sacchi, M. Sauvage, B. Schulz, M. R. P. Schirm, L. Spinoglio, S. Srinivasan, J. A. Stevens, M. Symeonidis, M. Trichas, M. Vaccari, L. Vigroux, H. Wozniak, G. S. Wright, and W. W. Zeilinger. Mapping the interstellar medium in galaxies with Herschel/SPIRE. A&A, 518:L62, July 2010b. doi: 10.1051/0004-6361/201014536.

F. Mannucci, G. Cresci, R. Maiolino, A. Marconi, and A. Gnerucci. A fundamental relation between mass, star formation rate and metallicity in local and high-redshift galaxies. MNRAS, 408:2115–2127, November 2010. doi: 10.1111/j.1365-2966.2010.17291.x.

F. Mannucci, R. Salvaterra, and M. A. Campisi. The metallicity of the long GRB hosts and the fundamental metallicity relation of low-mass galaxies. MNRAS, 414:1263–1268, June 2011. doi: 10.1111/j.1365-2966.2011.18459.x.

R. Genzel, L. J. Tacconi, D. Lutz, A. Saintonge, S. Berta, B. Magnelli, F. Combes, S. García-Burillo, R. Neri, A. Bolatto, T. Contini, S. Lilly, J. Boissier, F. Boone, N. Bouché, F. Bournaud, A. Burkert, M. Carollo, L. Colina, M. C. Cooper, P. Cox, C. Feruglio, N. M. Förster Schreiber, J. Freundlich, J. Gracia-Carpio, S. Juneau, K. Kovac, M. Lippa, T. Naab, P. Salome, A. Renzini, A. Sternberg, F. Walter, B. Weiner, A. Weiss, and S. Wuyts. Combined CO and Dust Scaling Relations of Depletion Time and Molecular Gas Fractions with Cosmic Time, Specific Star-formation Rate, and Stellar Mass. ApJ, 800:20, February 2015. doi: 10.1088/0004-637X/800/1/20.

N. Scoville, K. Sheth, H. Aussel, P. Vanden Bout, P. Capak, A. Bongiorno, C. M.

Casey, L. Murchikova, J. Koda, J. Álvarez-Márquez, N. Lee, C. Laigle, H. J. McCracken, O. Ilbert, A. Pope, D. Sanders, J. Chu, S. Toft, R. J. Ivison, and S. Manohar. ISM Masses and the Star formation Law at Z = 1 to 6: ALMA Observations of Dust Continuum in 145 Galaxies in the COSMOS Survey Field. ApJ, 820:83, April 2016. doi: 10.3847/0004-637X/820/2/83.

L. J. Tacconi, R. Genzel, A. Saintonge, F. Combes, S. García-Burillo, R. Neri, A. Bolatto, T. Contini, N. M. Förster Schreiber, S. Lilly, D. Lutz, S. Wuyts, G. Accurso, J. Boissier, F. Boone, N. Bouché, F. Bournaud, A. Burkert, M. Carollo, M. Cooper, P. Cox, C. Feruglio, J. Freundlich, R. Herrera-Camus, S. Juneau, M. Lippa, T. Naab, A. Renzini, P. Salome, A. Sternberg, K. Tadaki, H. Übler, F. Walter, B. Weiner, and A. Weiss. PHIBSS: Unified Scaling Relations of Gas Depletion Time and Molecular Gas Fractions. ApJ, 853:179, February 2018. doi: 10.3847/1538-4357/aaa4b4.

M. T. Sargent, E. Daddi, M. Béthermin, H. Aussel, G. Magdis, H. S. Hwang, S. Juneau, D. Elbaz, and E. da Cunha. Regularity Underlying Complexity: A Redshift-independent Description of the Continuous Variation of Galaxy-scale Molecular Gas Properties in the Mass-star Formation Rate Plane. ApJ, 793:19, September 2014. doi: 10.1088/0004-637X/793/1/19.

A. K. Leroy, F. Walter, A. Schruba, and HERACLES Collaboration. The IRAM Large Program HERACLES: The HERA CO-line Extragalactic Survey. In *American Astronomical Society Meeting Abstracts #219*, volume 219 of *American Astronomical Society Meeting Abstracts*, page 346.03, January 2012.

A. Saintonge, G. Kauffmann, C. Kramer, L. J. Tacconi, C. Buchbender, B. Catinella, S. Fabello, J. Graciá-Carpio, J. Wang, L. Cortese, J. Fu, R. Genzel, R. Giovanelli, Q. Guo, M. P. Haynes, T. M. Heckman, M. R. Krumholz, J. Lemonias, C. Li, S. Moran, N. Rodriguez-Fernandez, D. Schiminovich, K. Schuster, and A. Sievers. COLD GASS, an IRAM legacy survey of molecular gas in massive galaxies - I. Relations between H_2, H I, stellar content and structural properties. MNRAS, 415:32–60, July 2011. doi: 10.1111/j.1365-2966.2011.18677.x.

J. E. Geach, D. N. A. Murphy, and R. G. Bower. 4098 galaxy clusters to z 0.6 in the Sloan Digital Sky Survey equatorial Stripe 82. MNRAS, 413: 3059–3067, June 2011. doi: 10.1111/j.1365-2966.2011.18380.x.

E. Daddi, F. Bournaud, F. Walter, H. Dannerbauer, C. L. Carilli, M. Dickinson, D. Elbaz, G. E. Morrison, D. Riechers, M. Onodera, F. Salmi, M. Krips, and

D. Stern. Very High Gas Fractions and Extended Gas Reservoirs in z = 1.5 Disk Galaxies. ApJ, 713:686–707, April 2010a. doi: 10.1088/0004-637X/713/1/686.

E. Daddi, D. Elbaz, F. Walter, F. Bournaud, F. Salmi, C. Carilli, H. Dannerbauer, M. Dickinson, P. Monaco, and D. Riechers. Different Star Formation Laws for Disks Versus Starbursts at Low and High Redshifts. ApJ, 714:L118–L122, May 2010b. doi: 10.1088/2041-8205/714/1/L118.

L. J. Tacconi, R. Neri, R. Genzel, F. Combes, A. Bolatto, M. C. Cooper, S. Wuyts, F. Bournaud, A. Burkert, J. Comerford, P. Cox, M. Davis, N. M. Förster Schreiber, S. García-Burillo, J. Gracia-Carpio, D. Lutz, T. Naab, S. Newman, A. Omont, A. Saintonge, K. Shapiro Griffin, A. Shapley, A. Sternberg, and B. Weiner. Phibss: Molecular Gas Content and Scaling Relations in z ~ 1-3 Massive, Main-sequence Star-forming Galaxies. ApJ, 768:74, May 2013. doi: 10.1088/0004-637X/768/1/74.

D. Downes and P. M. Solomon. Rotating Nuclear Rings and Extreme Starbursts in Ultraluminous Galaxies. ApJ, 507:615–654, November 1998. doi: 10.1086/306339.

P. P. Papadopoulos, P. P. van der Werf, E. M. Xilouris, K. G. Isaak, Y. Gao, and S. Mühle. The molecular gas in luminous infrared galaxies - I. CO lines, extreme physical conditions and their drivers. MNRAS, 426:2601–2629, November 2012. doi: 10.1111/j.1365-2966.2012.21001.x.

Q. Tan, E. Daddi, G. Magdis, M. Pannella, M. Sargent, D. Riechers, M. Béthermin, F. Bournaud, C. Carilli, E. da Cunha, H. Dannerbauer, M. Dickinson, D. Elbaz, Y. Gao, J. Hodge, F. Owen, and F. Walter. Dust and gas in luminous proto-cluster galaxies at z = 4.05: the case for different cosmic dust evolution in normal and starburst galaxies. A&A, 569:A98, September 2014. doi: 10.1051/0004-6361/201423905.

A. M. Swinbank, P. P. Papadopoulos, P. Cox, M. Krips, R. J. Ivison, I. Smail, A. P. Thomson, R. Neri, J. Richard, and H. Ebeling. The Interstellar Medium in Distant Star-forming Galaxies: Turbulent Pressure, Fragmentation, and Cloud Scaling Relations in a Dense Gas Disk at z = 2.3. ApJ, 742:11, November 2011. doi: 10.1088/0004-637X/742/1/11.

D. A. Riechers, A. Cooray, A. Omont, R. Neri, A. I. Harris, A. J. Baker, P. Cox, D. T. Frayer, J. M. Carpenter, R. Auld, H. Aussel, A. Beelen, R. Blundell, J. Bock, D. Brisbin, D. Burgarella, P. Chanial, S. C. Chapman, D. L. Clements, A. Conley, C. D. Dowell, S. Eales, D. Farrah, A. Franceschini, R. Gavazzi, J. Glenn, M. Griffin, M. Gurwell, R. J. Ivison, S. Kim, M. Krips, A. M. J. Mortier, S. J. Oliver,

M. J. Page, A. Papageorgiou, C. P. Pearson, I. Pérez-Fournon, M. Pohlen, J. I. Rawlings, G. Raymond, G. Rodighiero, I. G. Roseboom, M. Rowan-Robinson, K. S. Scott, N. Seymour, A. J. Smith, M. Symeonidis, K. E. Tugwell, M. Vaccari, J. D. Vieira, L. Vigroux, L. Wang, J. Wardlow, and G. Wright. Dynamical Structure of the Molecular Interstellar Medium in an Extremely Bright, Multiply Lensed z ~= 3 Submillimeter Galaxy Discovered with Herschel. ApJ, 733:L12, May 2011. doi: 10.1088/2041-8205/733/1/L12.

F. Vito, R. Maiolino, P. Santini, M. Brusa, A. Comastri, G. Cresci, D. Farrah, A. Franceschini, R. Gilli, G. L. Granato, C. Gruppioni, D. Lutz, F. Mannucci, F. Pozzi, D. J. Rosario, D. Scott, M. Viero, and C. Vignali. Black hole accretion preferentially occurs in gas-rich galaxies*. MNRAS, 441:1059–1065, June 2014. doi: 10.1093/mnras/stu637.

D. Kakkad, V. Mainieri, M. Brusa, P. Padovani, S. Carniani, C. Feruglio, M. Sargent, B. Husemann, A. Bongiorno, M. Bonzini, E. Piconcelli, J. D. Silverman, and W. Rujopakarn. ALMA observations of cold molecular gas in AGN hosts at z

1.5 - evidence of AGN feedback? MNRAS, 468:4205–4215, July 2017. doi: 10.1093/mnras/stx726.

M. Perna, M. T. Sargent, M. Brusa, E. Daddi, C. Feruglio, G. Cresci, G. Lanzuisi, E. Lusso, A. Comastri, R. T. Coogan, Q. D'Amato, R. Gilli, E. Piconcelli, and C. Vignali. The molecular gas content in obscured AGN at $z > 1$. *ArXiv e-prints*, July 2018.

A. Lapi, C. Mancuso, A. Celotti, and L. Danese. Galaxy Evolution at High Redshift: Obscured Star Formation, GRB Rates, Cosmic Reionization, and Missing Satellites. ApJ, 835:37, January 2017. doi: 10.3847/1538-4357/835/1/37.

F. Bianchini, G. Fabbian, A. Lapi, J. Gonzalez-Nuevo, R. Gilli, and C. Baccigalupi. Broadband spectral energy distributions of SDSS-selected quasars and of their host galaxies: intense activity at the edge of the quenching. *ArXiv e-prints*, June 2018.

P. F. Hopkins, L. Hernquist, T. J. Cox, and D. Kereš. A Cosmological Framework for the Co-Evolution of Quasars, Supermassive Black Holes, and Elliptical Galaxies. I. Galaxy Mergers and Quasar Activity. ApJS, 175:356–389, April 2008. doi: 10.1086/524362.

N. Menci, F. Fiore, S. Puccetti, and A. Cavaliere. The Blast Wave Model for AGN Feedback: Effects on AGN Obscuration. ApJ, 686:219–229, October 2008. doi:

10.1086/591438.

N. Bergvall, T. Marquart, M. J. Way, A. Blomqvist, E. Holst, G. Östlin, and E. Zackrisson. Local starburst galaxies and their descendants. Statistics from the Sloan Digital Sky Survey. A&A, 587:A72, March 2016. doi: 10.1051/0004-6361/201525692.

A. Lapi, R. Aversa, and L. Danese. Black Hole and Galaxy Coevolution from Continuity Equation and Abundance Matching. In *The Interplay between Local and Global Processes in Galaxies,*, page 7, June 2016.

C. Mancuso, A. Lapi, Z.-Y. Cai, M. Negrello, G. De Zotti, A. Bressan, M. Bonato, F. Perrotta, and L. Danese. Predictions for Ultra-deep Radio Counts of Star-forming Galaxies. ApJ, 810:72, September 2015. doi: 10.1088/0004-637X/810/1/72.

A. Lapi, M. Negrello, J. González-Nuevo, Z.-Y. Cai, G. De Zotti, and L. Danese. Effective Models for Statistical Studies of Galaxy-scale Gravitational Lensing. ApJ, 755:46, August 2012. doi: 10.1088/0004-637X/755/1/46.

M. Bonato, M. Negrello, Z.-Y. Cai, G. De Zotti, A. Bressan, A. Lapi, C. Gruppioni, L. Spinoglio, and L. Danese. Exploring the early dust-obscured phase of galaxy formation with blind mid-/far-infrared spectroscopic surveys. MNRAS, 438: 2547–2564, March 2014. doi: 10.1093/mnras/stt2375.